ESD-TR-90-119

Quarterly Technical Report

Solid State Research

1990:3

Lincoln Laboratory

MASSACHUSETTS INSTITUTE OF TECHNOLOGY

LEXINGTON, MASSACHUSETTS

Prepared for the Department of the Air Force under Contract F19628-90-C-0002.

Approved for public release; distribution is unlimited.

This report is based on studies performed at Lincoln Laboratory, a center for research operated by Massachusetts Institute of Technology. The work was sponsored by the Department of the Air Force under Contract F19628-90-C-0002.

The ESD Public Affairs Office has reviewed this report, and it is releasable to the National Technical Information Service, where it will be available to the general public, including foreign nationals.

This technical report has been reviewed and is approved for publication.

FOR THE COMMANDER

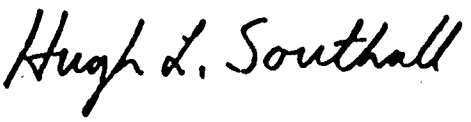

Hugh L. Southall, Lt. Col., USAF
Chief, ESD Lincoln Laboratory Project Office

MASSACHUSETTS INSTITUTE OF TECHNOLOGY
LINCOLN LABORATORY

SOLID STATE RESEARCH

QUARTERLY TECHNICAL REPORT

1 MAY — 31 JULY 1990

ISSUED 18 DECEMBER 1990

LEXINGTON MASSACHUSETTS

ABSTRACT

This report covers in detail the research work of the Solid State Division at Lincoln Laboratory for the period 1 May through 31 July 1990. The topics covered are Electrooptical Devices, Quantum Electronics, Materials Research, Submicrometer Technology, Microelectronics, and Analog Device Technology. Funding is provided primarily by the Air Force, with additional support provided by the Army, DARPA, Navy, SDIO, NASA, and DOE.

TABLE OF CONTENTS

LIST OF ILLUSTRATIONS

LIST OF ILLUSTRATIONS (Continued)

LIST OF ILLUSTRATIONS (Continued)

LIST OF ILLUSTRATIONS (Continued)

LIST OF ILLUSTRATIONS (Continued)

LIST OF TABLES

INTRODUCTION

1. ELECTROOPTICAL DEVICES

Slow evaporation of In has been measured and identified as a major cause of surface roughness in the heat treatment of InP. Techniques have been developed for effective protection against the evaporation loss and have reproducibly resulted in smooth surfaces.

A high-performance bandpass integrated-optical modulator has been used in an experimental K-band fiber-optic analog link. This amplifierless link has shown an electrical insertion loss of only 34 dB at 20 GHz and an intermodulation-free dynamic range of 108 dB-$Hz^{2/3}$.

The x-ray diffraction from InGaAs/GaAs multiple quantum wells grown by organometallic vapor phase epitaxy in two very different reactors has been compared with simulated rocking curves. The results show that nearly ideal structures are obtained in both cases and that any graded region present in these ~ 10-nm wells must be < 2.5 nm.

2. QUANTUM ELECTRONICS

Broad-area (500 × 1000 μm) graded-index separate-confinement heterostructure single-quantum-well (GRIN-SCH SQW) laser diodes have been used as single-pass optical amplifiers in a master-oscillator/power-amplifier (MOPA) system. At 4 A of diode-amplifier current, 1 W of CW output power was achieved in a single spatial mode with a large-signal gain of 15 and a bandwidth of over 40 nm.

A 0.97-μm strained-layer InGaAs diode laser has been used to pump a 1.03-μm Yb:YAG laser. This diode-pumped laser system offers a number of advantages over AlGaAs-pumped Nd^{3+} lasers, including lower thermal loading of the solid state gain medium and broad absorption features in the Yb:YAG which permit less stringent temperature control of the diode laser.

Diode-pumped microchip lasers have been gain switched to produce 170-ns pulses at a repetition rate of 100 kHz, with peak powers of 1.8 W. The minimum pulse width and peak power are limited by the peak power of the diode pump.

The temporal, spectral, and coherence properties of a Ti:Al_2O_3 MOPA system have been measured. The output pulse of 115 ns full width at half-maximum can be tuned over a range from 750 to 850 nm and is offset in frequency by 2 MHz from the oscillator because of temporal changes in refractive index during the pulse.

Nondegenerate four-wave mixing with a conversion efficiency of up to 5 percent has been obtained in a GaAs/AlGaAs ridge waveguide using a 5-ps input pump pulse of 12-W peak power. This conversion efficiency, which is the largest reported for any nonlinear waveguide except silica fibers, is sufficient for nonlinear optical switching applications.

3. MATERIALS RESEARCH

Diode lasers with a strained AlInGaAs SQW active layer have been fabricated for the first time. Lasers emitting at wavelengths from 785 to 890 nm, with threshold current densities and differential quantum efficiencies comparable to those of devices with AlGaAs and InGaAs active layers, have been fabricated in GRIN-SCH structures grown by organometallic vapor phase epitaxy on GaAs substrates.

The wavelength response of IrSi Schottky-barrier infrared detectors has been extended by forming the IrSi film on *p*-Si substrates that have been implanted with low-energy boron ions to produce a shallow p^+ layer. This layer increases the image-force barrier lowering and field-assisted tunneling, thereby reducing the optical barrier height to 0.100 eV, which corresponds to a detector cutoff wavelength of 12.4 μm.

4. SUBMICROMETER TECHNOLOGY

Thin organosilicon films have been deposited by plasma-enhanced chemical vapor deposition and used as deep-UV photoresists. Submicrometer patterning was achieved with 193-nm exposure followed by either wet or dry development.

Arrays of diffractive optical elements, such as a fly's-eye lens consisting of 10,000 lenslets, have been fabricated and utilized as "diffusers" in the illumination optics of a small-field 193-nm exposure system that uses a reflecting microscope objective as the projection lens. Such components are required in excimer laser lithography systems to destroy the spatial coherence of the laser beam and efficiently couple laser energy into the entrance pupil of the optical system.

5. MICROELECTRONICS

A visible-wavelength charge-coupled device (CCD) has been fabricated with an electronic shutter to reduce the smear that occurs in a normal device when the imaging-array charge is transferred. Preliminary measurements show that the photon-generated detected charge is reduced by a factor of 50 to 100 by the shutter and that the switching time is of the order of a microsecond.

A dynamic random-access memory cell using a GaAs/AlGaAs quantum-well structure has been demonstrated. A charge storage time of 5.4 s was measured at room temperature.

6. ANALOG DEVICE TECHNOLOGY

An all-refractory process for the fabrication of superconductive circuits has been developed. This process produced dc superconducting quantum interference devices (SQUIDs) with a noise performance exceeding that of the best dc SQUIDs made to date.

A 2-μm CMOS/CCD process has been developed to allow integration of high-performance analog, digital, and discrete-time analog circuitry. Because of several conflicting requirements, the design of the buried-channel CCDs presented the greatest challenge in this process development.

REPORTS ON SOLID STATE RESEARCH

1 May Through 31 July 1990

PUBLICATIONS

Femtosecond Dynamics of the Nonlinear Index near the Band Edge in AlGaAs Waveguides	K.K. Anderson* M.J. LaGasse* C.A. Wang J.C. Fujimoto* H.A. Haus*	*Appl. Phys. Lett.* **56**, 1834 (1990)
Preparation of $YBa_2Cu_3O_x$ Thin Films by Multisource Deposition	M. Bhushan	*Advances in Cryogenic Engineering Materials*, edited by R.P. Reed and F.R. Fickett (Plenum, New York, 1990), pp. 453-459
Preparation and Patterning of $YBa_2Cu_3O_x$ Thin Films	M. Bhushan A.J. Strauss	*Advances in Cryogenic Engineering Materials*, edited by R.P. Reed and F.R. Fickett (Plenum, New York, 1990), pp. 493-499
Gimbal for Aligning Laser and Lenslet Arrays for Coherent Operation in an External Cavity	J.W. Caunt V. Diadiuk	*Appl. Opt.* **29**, 2311 (1990)
InGaAs/AlGaAs Strained Single Quantum Well Diode Lasers with Extremely Low Threshold Current Density and High Efficiency	H.K. Choi C.A. Wang	*Appl. Phys. Lett.* **57**, 321 (1990)
Low-Loss Analog Fiber-Optic Links	C.H. Cox III D.Z. Tsang L.M. Johnson G.E. Betts	*1990 IEEE MTT-S International Microwave Symposium Digest*, Vol. 1 (IEEE, New York, 1990), pp. 157-160
An Analytic and Experimental Comparison of Direct and External Modulation in Analog Fiber-Optic Links	C.H. Cox III G.E. Betts L.M. Johnson	*IEEE Trans. Microwave Theory Tech.* **38**, 501 (1990)

* Author not at Lincoln Laboratory.

Self-Starting Additive-Pulse Mode-Locked Diode-Pumped Nd:YAG Laser	J. Goodberlet* J. Jacobson* J.G. Fujimoto* P.A. Schulz T.Y. Fan	*Opt. Lett.* **15**, 504 (1990)
Horizontal Gradient-Freeze Growth of InP Crystals under Controlled Pressure	G.W. Iseler H.R. Clark, Jr.	*Proceedings of the Second International Conference on Indium Phosphide and Related Materials* (IEEE, New York, 1990), p. 25
Measurements of the Two-Photon Absorption Coefficient in GaAs Quantum Well Lasers	H.Q. Le H.K. Choi C.A. Wang	*Appl. Phys. Lett.* **57**, 212 (1990)
Role of Nitrogen Ions in Ion-Beam Reactive Sputtering of NbN	D.J. Lichtenwalner A.C. Anderson D.A. Rudman*	*J. Vac. Sci. Technol. A* **8**, 1283 (1990)
Hardening Process for Plasma Deposited Planar Amorphous Carbon Films Used in Bilayer Resists	S.W. Pang R.B. Goodman M.W. Horn	*Proceedings of the 7th International IEEE VLSI Multilevel Interconnection Conference* (IEEE, New York, 1990), pp. 435-437
One-Gigabit per Second Free-Space Optical Interconnection	D.Z. Tsang	*Appl. Opt.* **29**, 2034 (1990) DTIC AD-A223712
Selective Plasma Etching of Si from GaAs-on-Si Wafers for Microwave Via Hole Formation	G.W. Turner C.L. Chen M.K. Connors L.J. Mahoney W.L. McGilvary	*Electron. Lett.* **26**, 854 (1990)
A New Organometallic Vapor Phase Epitaxy Reactor for Highly Uniform Epitaxy	C.A. Wang	*Lincoln Lab. J.* **3**, 3 (1990)

* Author not at Lincoln Laboratory.

ACCEPTED FOR PUBLICATION

Recent Advances in Semiconductor Integrated Optics	D.E. Bossi* J.P. Donnelly F.J. Leonberger*	In *Integrated Optics Technology*, 2nd ed., edited by T. Tamir, Vol. 26 of *Springer Series in Electronics and Photonics* (Springer-Verlag, New York)
Efficient GaInAsSb/AlGaAsSb Diode Lasers Emitting at 2.29 μm	S.J. Eglash H.K. Choi	*Appl. Phys. Lett.*
Capacitance-Voltage Measurements on Metal-SiO_2-Diamond Structures Fabricated with (100)- and (111)-Oriented Substrates	M.W. Geis J.A. Gregory B.B. Pate*	*IEEE Trans. Electron Devices*
Measurement of the Third-Order Optical Nonlinear Susceptibility Using Four-Wave Mixing in a Single-Mode Ridge Waveguide	H.Q. Le W.D. Goodhue K. Rauschenbach	*Opt. Lett.*
Amorphous Carbon Films as Planarization Layers Deposited by Plasma Enhanced Chemical Vapor Deposition	S.W. Pang M.W. Horn	*IEEE Electron Device Lett.*
Polyimide Optical Waveguides Fabricated with Electron-Beam Lithography	M.J. Rooks H.V. Roussell L.M. Johnson	*Appl. Opt.*
IrSi Schottky-Barrier Infrared Detectors with Wavelength Response Beyond 12 μm	B-Y. Tsaur C.K. Chen B.A. Nechay	*IEEE Electron Device Lett.*
Hydrogen Annealing of PtSi-Si Schottky-Barrier Contacts	B-Y. Tsaur J.P. Mattia C.K. Chen	*Appl. Phys. Lett.*

* Author not at Lincoln Laboratory.

PRESENTATIONS†

Substrate Temperature Measurement	A.C. Anderson	Conference on the Science and Technology of Thin-Film Superconductors, Denver, Colorado, 30 April – 4 May 1990
Stripline Resonators for Characterization of High-T_c Superconducting Films for Device Applications	D.E. Oates A.C. Anderson P.M. Mankiewich*	
High-Frequency Applications of Resonant-Tunneling Devices	T.C.L.G. Sollner E.R. Brown C.D. Parker W.D. Goodhue	Quantum Well Semiconductor Devices Symposium, Waltham, Massachusetts, 1 May 1990
Diode Laser Arrays	J.P. Donnelly	Lincoln Laboratory Technical Seminar Series, University of Minnesota, Minneapolis, Minnesota, 3 May 1990
Advanced CCD Imager Technology for Use from 1 to 10,000 Å	J.C. Twichell B.E. Burke R.K. Reich W.H. McGonagle C.M. Huang M.W. Bautz* J.P. Doty* G.R. Ricker* R.W. Mountain V.S. Dolat	Eighth Topical Conference on High-Temperature Plasma Diagnostics, Hyannis, Massachusetts, 6-10 May 1990
High-Temperature Superconductive Microstrip Filters	W.G. Lyons P.M. Mankiewich* M.L. O'Malley* A.C. Anderson R.S. Withers R.E. Howard*	1990 IEEE MTT-S International Microwave Symposium, Dallas, Texas, 7-11 May 1990
Power and Current Distribution Effects in Striplines	D.E. Oates	
Superconductive Microwave Circuits	R.W. Ralston	

* Author not at Lincoln Laboratory.

† Titles of presentations are listed for information only. No copies are available for distribution.

Superconductive Delay Lines	R.W. Ralston W.G. Lyons P.M. Mankiewich*	1990 IEEE MTT-S International Microwave Symposium, Dallas, Texas, 7-11 May 1990
Advances in Solid State Laser Technology and Applications	A. Mooradian	OSA Meeting, Rochester, New York, 11 May 1990
Advanced Device Fabrication Using Chlorine Ion Beam Assisted Etching	W.D. Goodhue	Lincoln Laboratory Technical Seminar Series, Cornell University, Ithaca, New York, 13 May 1990
Insulating Layer for Device Isolation in GaAs Semiconductor Integrated Circuits	A.R. Calawa F.W. Smith	Semi-insulating III-V Materials, Toronto, Canada, 13-16 May 1990
Ultrashort Pulse Generation in Solid State Lasers: Ti:Al_2O_3 and Diode Pumped Nd:YAG	J. Goodberlet* J. Jacobson* J. Wang* P.A. Schulz T.Y. Fan J.G. Fujimoto*	Ultrafast Phenomena Meeting, Monterey, California, 14-17 May 1990
High Frequency Oscillators Based on Resonant Tunneling	T.C.L.G. Sollner E.R. Brown J.R. Söderström* C.D. Parker W.D. Goodhue	NATO Advanced Research Workship on Resonant Tunneling, El Escorial, Spain, 14-18 May 1990
Shallow-Buried-Channel CCDs with Built-in Drift Fields	A.L. Lattes S.C. Munroe	1990 IEEE Workshop on Advanced Solid-State imagers, New York, New York, 18-20 May 1990
5-V Uniphase CMOS/CCD Process for Mixed-Signal Processing	S.C. Munroe A.L. Lattes D.B. Whitley D.R. Arsenault	
Device Applications of Diamonds	M.W. Geis	Workshop on Science and Technology of Diamond Films, Cleveland, Ohio, 20-24 May 1990

* Author not at Lincoln Laboratory.

High Contrast MQW Modulators Grown by Organometallic Chemical Vapor Deposition	B.F. Aull K.B. Nichols	1990 Conference on Lasers and Electro-Optics, Anaheim, California, 21-25 May 1990
Operation of Five Discrete Diode Lasers as a Coherent Ensemble by Fiber Coupling into an External Cavity	C. Corcoran R.H. Rediker	
InGaAs/AlGaAs Strained Quantum Well Lasers Emitting at 1 μm with Extremely Low Threshold Current Density and High Efficiency	H.K. Choi C.A.Wang	
Efficient GaInAsSb/AlGaAsSb Diode Lasers Emitting at 2.29 μm	S.J. Eglash H.K. Choi	
Self-Starting Additive Pulse Mode-Locking of a Diode Pumped Nd:YAG Laser	J. Goodberlet* J. Jacobson* J.G. Fujimoto* P.A. Schulz T.Y. Fan	
Self-Starting Additive Pulse Mode-Locking Characterization with a Ti:Al_2O_3 Laser	J. Goodberlet* J. Wang* P.A. Schulz J.G. Fujimoto*	
Electrooptically Tuned, Single Frequency Nd:YAG Laser	S.R. Henion P.A. Schulz	
Laser Pumping of Ti:Sapphire Amplifiers Using Random Binary Phase Plates	P. Lacovara K.F. Wall R.L. Aggarwal M.W. Geis K. Krohn	
A Ti:Al_2O_3 Master Oscillator–Power Amplifier System	K.F. Wall R.L. Aggarwal P.A. Schulz P. Lacovara V. Daneu A. Walther A. Sanchez	

* Author not at Lincoln Laboratory.

Measurements of the Third-Order Nonlinear Susceptibility of AlGaAs/GaAs Heterostructures Using Picosecond Nondegenerate Four-Wave Mixing in Waveguides	H.Q. Le W.D. Goodhue	1990 International Quantum Electronics Conference, Anaheim, California, 21-25 May 1990
Limits Imposed by Spatial Hole Burning on the Single-Mode Operation of Standing-Wave Laser Cavities	J.J. Zayhowski	
Silylation Processes Based on UV Laser-Induced Crosslinking	M.A. Hartney M. Rothschild R.R. Kunz D.J. Ehrlich D.C. Shaver	34th Electron, Ion, Photon Beam Symposium, San Antonio, Texas 29 May – 1 June 1990
Plasma Deposited Organosilicon Thin Films as Dry Resists for Deep UV Lithography	M.W. Horn S.W. Pang M. Rothschild	
Polysilyne Thin Films as Resists for Deep UV Lithography	R.R. Kunz M.W. Horn P.A. Bianconi* D.A. Smith* C.A. Freed*	
Plasma Deposited Amorphous Carbon Films as Planarization Layers	S.W. Pang M.W. Horn	
Technology Developments for 193-nm Lithography	M.A. Hartney	Seminar, Texas Instruments, Dallas, Texas, 4 June 1990
Fabrication and Characterization of Semiconductor Microlens Arrays	V. Diadiuk Z.L. Liau J.N. Walpole	Optical Fabrication and Testing Workshop, Monterey, California, 12-14 June 1990
Plasma Deposited Amorphous Carbon Planarizing Layers	M.W. Horn	Seminar, Texas Instruments, Dallas, Texas, 13 June 1990

* Author not at Lincoln Laboratory.

Technology Developments for 193-nm Lithography	M.A. Hartney	Seminar, Raytheon Research Center, Lexington, Massachusetts, 16 June 1990
Homoepitaxial Diamond Films	M.W. Geis	New England Vacuum Society Meeting, Burlington, Massachusetts, 18-19 June 1990
Room-Temperature Oscillations up to 675 GHz in InAs/AlSb Resonant-Tunneling Diodes	E.R. Brown C.D. Parker L.J. Mahoney J.R. Söderström* T.C. McGill*	Device Research Conference, Santa Barbara, California, 25-27 June 1990
High-Temperature Superconductive Passive Microwave Devices	W.G. Lyons R.R. Bonetti* A.E. Williams* P.M. Mankiewich* M.L. O'Malley* R.W. Withers A.C. Anderson R.E. Howard*	
A Fused Quartz Diaphragm Gauge for the Pressure Controlled Crystal Growth of Indium Phosphide	D.L. Hovey G.B. Finkenbeiner* G.W. Iseler H.R. Clark, Jr.	American Scientific Glassblowers Society Symposium, Orlando, Florida, 25-29 June 1990
Photoresist Chemistry for Lithography at 193-nm	R.R. Kunz	Northeast Regional American Chemical Society Meeting, Potsdam, New York, 26-27 June 1990
Dry Chemical Etching of Gallium Arsenide in an OMVPE Reactor	C.W. Krueger M. Flytzani-Stephanopoulos* R.A. Brown* C.A. Wang	1990 Electronic Materials Conference, Santa Barbara, California, 27-29 June 1990
OMVPE Growth of Strained-Layer InGaAs/AlGaAs Heterostructures for Quantum-Well Diode Lasers	C.A. Wang H.K. Choi	

* Author not at Lincoln Laboratory.

Growth and Characterization of High-Current Density High-Speed Resonant-Tunneling Diodes in the InAs/AlSb Material System	J.R. Söderström* J.Y. Yao* T.C. McGill* E.R. Brown C.D. Parker L.J. Mahoney	1990 Electronic Materials Conference, Santa Barbara, California, 27-29 June 1990
Ultrathin UV Resists	M. Rothschild	Gordon Research Conference on Chemistry and Physics of Microstructure Fabrication, New London, New Hampshire, 9-13 July 1990
Liouville Operator Theory of Nonlinear Optical Susceptibilities	P.L. Kelley J.P. Taran* O. Blum* I. Kim* T.K. Gustafson*	Nonlinear Optics: Materials, Phenomena and Devices, Kauai, Hawaii, 16-20 July 1990
Diamond Transistor Performance and Fabrication	M.W. Geis	Diamond and Diamond-Like Films and Coatings, Castelvecchio Pascoli, Italy, 22 July–3 August 1990
20-GHz Optical Analog Link Using an External Modulator	G.E. Betts C.H. Cox III K.G. Ray	Summer Topical Meeting on Broadband Analog Optoelectronics: Devices and Systems, Monterey, California, 23-25 July 1990
Incrementally Lossless, Broad-Bandwidth, Analog Fiber Optic Link	C.H. Cox III G.E. Betts A.C. Yee	
Linearization of an Interferometric Modulator at Microwave Frequencies by Polarization Mixing	L.M. Johnson H.V. Roussell	
High-Power Semiconductor Laser Amplifiers	C.D. Nabors R.L. Aggarwal H.K. Choi C.A. Wang A. Mooradian	New Semiconductor Laser Devices and Applications, Monterey, California, 23 July–3 August 1990

* Author not at Lincoln Laboratory.

ORGANIZATION

SOLID STATE DIVISION

A.L. McWhorter, *Head*
I. Melngailis, *Associate Head*
E. Stern, *Associate Head*
J.F. Goodwin, *Assistant*

D.J. Ehrlich, *Senior Staff*
N.L. DeMeo, Jr., *Associate Staff*
J.W. Caunt, *Assistant Staff*
K.J. Challberg, *Administrative Staff*

SUBMICROMETER TECHNOLOGY

D.C. Shaver, *Leader*
M. Rothschild, *Assistant Leader*

Astolfi, D.K.
Craig, D.M.
Dennis, C.L.
Doran, S.P.
Efremow, N.N., Jr.
Forte, A.R.
Gajar, S.A.*
Geis, M.W.
Goodman, R.B.
Hartney, M.A.
Horn, M.W.
Kunz, R.R.
Lyszczarz, T.M.
Maki, P.A.
Melngailis, J.†
Paladugu, R.R.
Sedlacek, J.H.C.
Uttaro, R.S.

QUANTUM ELECTRONICS

A. Mooradian, *Leader*
P.L. Kelley, *Associate Leader*
A. Sanchez-Rubio, *Assistant Leader*

Aggarwal, R.L.
Barch, W.E.
Cook, C.C.
Daneu, V.
DeFeo, W.E.
DiCecca, S.
Dill, C.D., III
Fan, T.Y.
Hancock, R.C.
Henion, S.R.
Hotaling, T.C.
Hsu, L.*
Jeys, T.H.
Korn, J.A.
Lacovara, P.
Le, H.Q.
Menyuk, N.†
Nabors, C.D.
Ochoa, J.R.
Schulz, P.A.
Seemungal, W.A.
Sullivan, D.J.
Wall, K.F.
Zayhowski, J.J.

ELECTRONIC MATERIALS

A.J. Strauss, *Leader*
B-Y. Tsaur, *Associate Leader*
H.J. Zeiger, *Senior Staff*

Anderson, C.H., Jr.
Button, M.J.
Chen, C.K.
Choi, H.K.
Clark, H.R., Jr.
Connors, M.K.
Delaney, E.J.
Eglash, S.J.
Fahey, R.E.
Finn, M.C.
Iseler, G.W.
Kolesar, D.F.
Krohn, L., Jr.
Mastromattei, E.L.
Mattia, J.P.*
McGilvary, W.L.
Nechay, B.A.
Nitishin, P.M.
Pantano, J.V.
Tracy, D.M.
Turner, G.W.
Wang, C.A.

---

* Research Assistant
† Part Time

APPLIED PHYSICS

R.C. Williamson, *Leader*
D.L. Spears, *Assistant Leader*
R.H. Rediker, *Senior Staff*

Aull, B.F.
Bailey, R.J.
Barwick, D.S.*
Betts, G.E.
Corcoran, C.J.*
Cox, C.H., III
Diadiuk, V.
Donnelly, J.P.
Ferrante, G.A.
Groves, S.H.
Harman, T.C.
Hovey, D.L.
Johnson, L.M.
Liau, Z.L.
Lind, T.A.
Missaggia, L.J.
Mull, D.E.
O'Donnell, F.J.
Palmacci, S.T.
Palmateer, S.C.
Pheiffer, B.K.*
Rauschenbach, K.
Reeder, R.E.
Roussell, H.V.
Shiple, S.D.*
Tsang, D.Z.
Walpole, J.N.
Woodhouse, J.D.
Yee, A.C.

ANALOG DEVICE TECHNOLOGY

R.W. Ralston, *Leader*
R.S. Withers, *Associate Leader*
T.C.L.G. Sollner, *Assistant Leader*
R.M. Lerner, *Senior Staff*†

Anderson, A.C.
Arsenault, D.R.
Bhushan, M.
Boisvert, R.R.
Brogan, W.T.
Denneno, A.P.
Fitch, G.L.
Green, J.B.
Hamm, J.M.
Holtham, J.H.
Lattes, A.L.
Lichtenwalner, D.J.*
Lyons, W.G.
Macedo, E.M., Jr.
Minnick, R.G.
Munroe, S.C.
Oates, D.E.
Sage, J.P.
Seaver, M.M.
Slattery, R.L.
Westerheim, A.C.*
Whitley, D.B.
Yu-Jahnes, L-S.*

MICROELECTRONICS

R.A. Murphy, *Leader*
E.D. Savoye, *Associate Leader*
B.B. Kosicki, *Assistant Leader*
R.W. Chick, *Senior Staff*

Actis, R.
Bales, J.W.*
Bergeron, N.J.
Bozler, C.O.
Brown, E.R.
Burke, B.E.
Calawa, A.R.
Chen, C.L.
Chiang, A.M.
Chuang, M.L.*
Clifton, B.J.
Collins, I.K.
Cooper, M.J.
Crenshaw, D.L.*
Daniels, P.J.
Doherty, C.L., Jr.
Dolat, V.S.
Donahue, T.C.
Durant, G.L.
Felton, B.J.
Gladden, D.B.‡
Goodhue, W.D.
Gray, R.V.
Gregory, J.A.
Hollis, M.A.
Huang, C.M.
Hurley, E.T.
Johnson, B.W.
Johnson, K.F.
LaFranchise, J.R.
Lincoln, G.A., Jr.
Mahoney, L.J.
Manfra, M.J.
Mathews, R.H.
McGonagle, W.H.
McIntosh, K.A.
McMorran, R.A.
McNamara, M.J.
Mountain, R.W.
Nichols, K.B.
Parker, C.D.
Percival, K.A.
Pichler, H.H.
Rabe, S.
Rathman, D.D.
Reich, R.K.
Reinold, J.H., Jr.
Smith, F.W., III
Vera, A.
Young, D.J.

* Research Assistant
† Part Time
‡ Staff Associate

1. ELECTROOPTICAL DEVICES

1.1 PREVENTION OF In EVAPORATION AND PRESERVATION OF SMOOTH SURFACE IN THERMAL ANNEALING AND MASS TRANSPORT OF InP

Thermal degradation of III-V compound semiconductors has been of considerable interest because of its importance in material growth, device fabrication, and perhaps also device reliability. Problems due to the high volatility of group V species have been extensively investigated and techniques are available for effective suppression. However, evaporation of group III species has been far less obvious and scarcely studied. In this work, we investigate the slow evaporation of In and show that it has a significant effect on the surface morphology of InP. We have also developed techniques to suppress effectively the evaporation and have reproducibly achieved a smooth surface after a long (> 100 h) mass transport at temperatures up to 835°C.

The furnace system used in the present work is illustrated in Figure 1-1. It is a refined version of a previous design [1] for high-temperature mass transport, in which high phosphorus vapor pressure can be used with a minimal phosphine consumption and clean phosphorus disposition. New features in the design include a large-diameter (30 mm) reactor tube and a separate phosphorus trap. A long section of the thermocouple tube is enlarged to restrict the outdiffusion of the phosphorus vapor generated by phosphine decomposition in the heated region. The rear end of the reactor tube is tapered to a 4-mm diameter and bent down to the phosphorus trap. The temperature and geometry of this region are tailored not only to condense effectively the phosphorus in the trap but keep the reactor tube entirely free of phosphorus deposition. This new system is capable of hundreds of hours of operation without phosphorus clogging, which was one major problem in the previous design.

Polished, 9 × 15-mm (100) InP substrates were cleaned and lightly etched before being loaded into the cleaned and baked system. The system was then purged with H_2 before PH_3 was introduced. With 5 percent PH_3, the InP wafers showed no metallic indium droplet formation at temperatures up to 860°C.

A measurement of In evaporation and equilibrium In vapor pressure was carried out. A 3-mm-diam. hole was drilled in the graphite used to cover the InP wafer, and the graphite container was placed in the gas flow without any further protection, i.e., with no InP covers and quartz container like those shown in Figure 1-1. The evaporation through the hole opening resulted in the formation of a crater in the InP wafer. Figure 1-2 shows a region near the rim of a crater. Inside the crater, the wafer surface becomes very rough. From the measured crater depth [Figure 1-2(b)], area, and time, the evaporation rate (atoms per min) was determined and was found to be roughly constant in time. Since the gas flow (10 ml/min) is slow relative to the vapor diffusion across the tube diameter, the evaporation rate is assumed to be limited by the gas flow. The equilibrium concentration N_0 of In atoms in the vapor can therefore be estimated by

$$N_0 \cong \frac{\text{evaporation rate}}{\text{gas flow}} \quad . \tag{1.1}$$

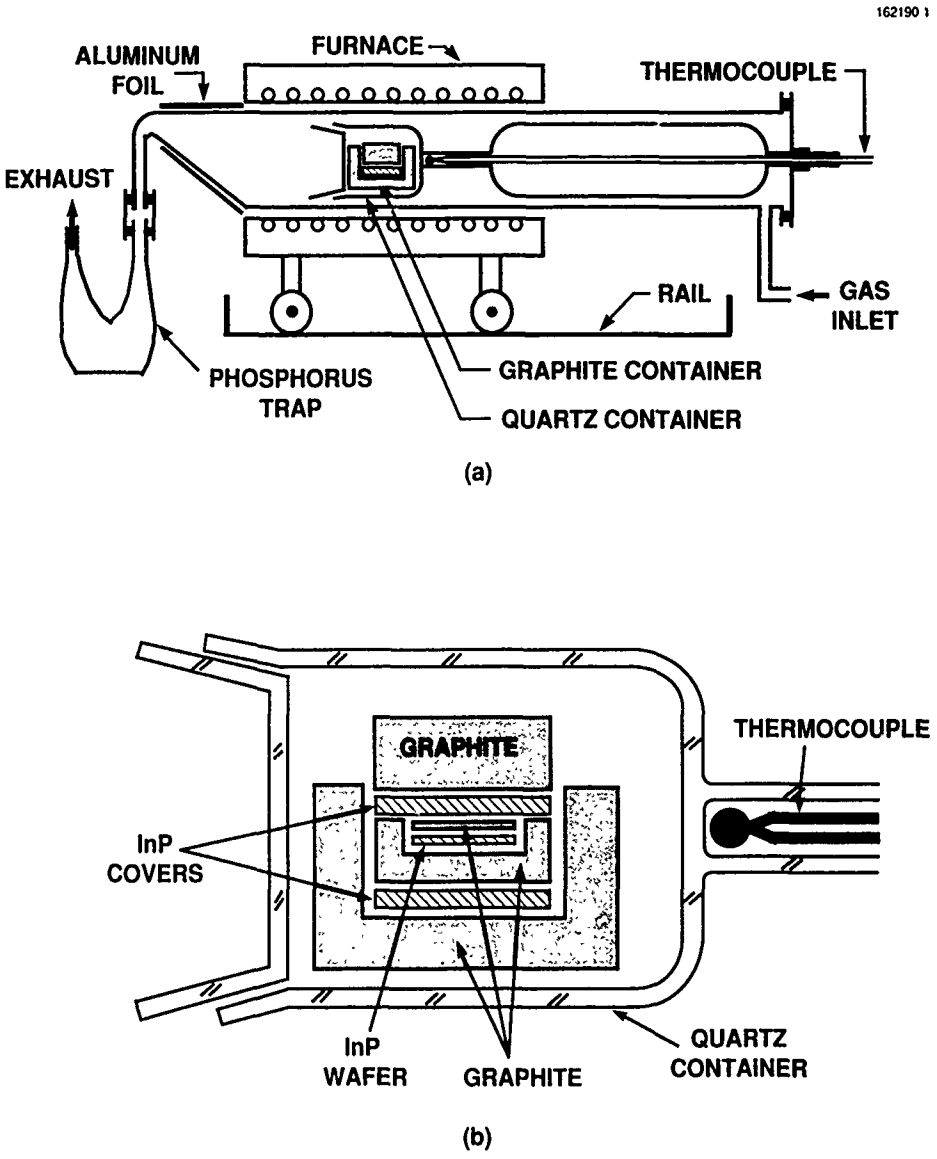

Figure 1-1. (a) Furnace system used in high-temperature annealing and mass transport of InP. This system is capable of high phosphorus vapor pressure with minimal phosphine consumption and clean phosphorus disposition. (b) Detailed illustration of the container, which further protects the wafer from evaporation loss of In.

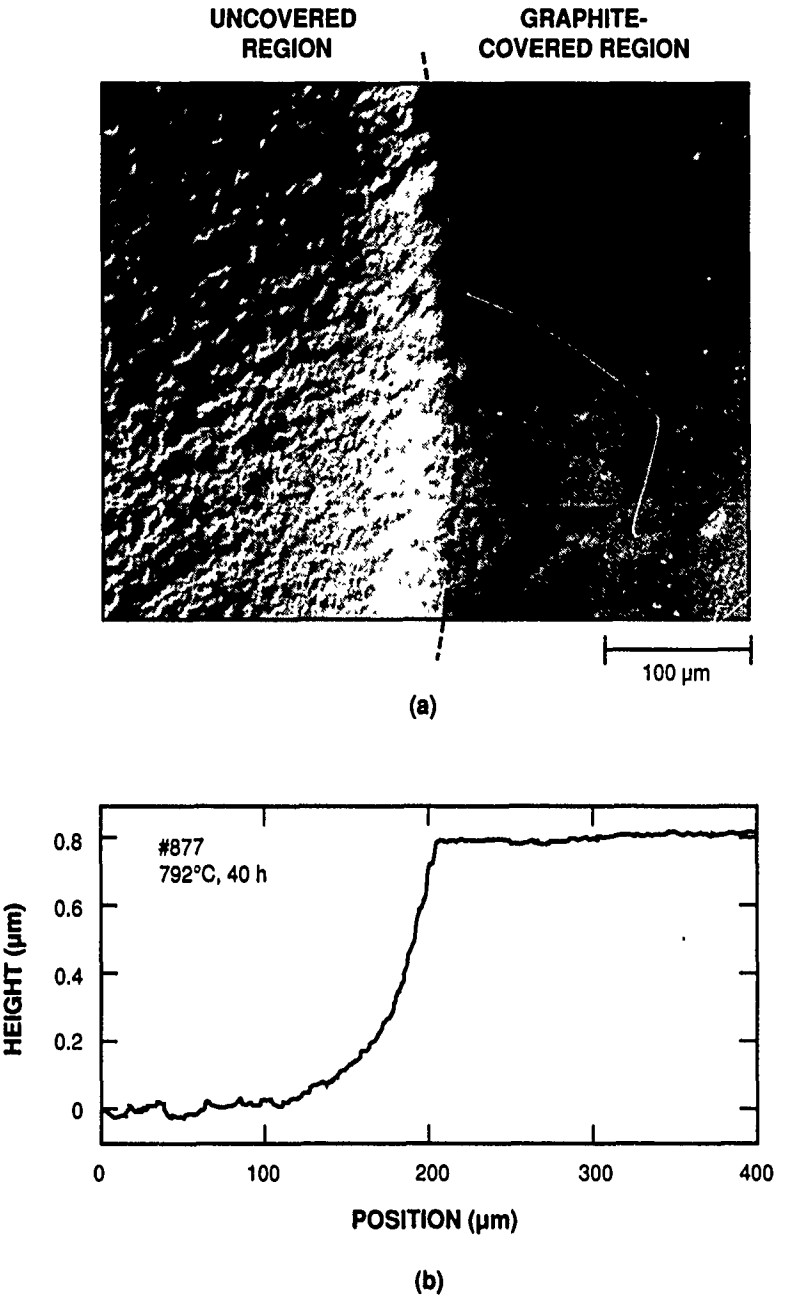

Figure 1-2. Crater formation due to evaporation loss in an uncovered region after 792°C, 40-h annealing. (a) Interference-contrast optical micrograph showing considerable roughness in the crater region. (b) Stylus surface profiling across the crater.

The value of N_0 thus obtained at 792°C was 2.5×10^{12} atoms/ml, which is lower than the vapor pressure of metallic indium (7×10^{12} molecules/ml as derived from [2]) and is consistent with the temperature being below that of metallic indium droplet formation.

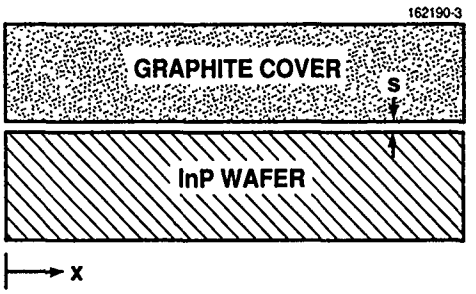

Figure 1-3. Illustration of a cover on an InP wafer.

Very effective protection against evaporation loss can be obtained by using a cover, as can be seen in the following analysis. Assume the cover and the wafer are separated by a very small gap s, as illustrated in Figure 1-3. Because of diffusion to the ambient, the In vapor concentration $N(0)$ at the edge of the covered region will be lower than the concentration $N(x)$ in the covered region. Since the evaporation rate per unit area at point x in the covered region is $k(N_0 - N)$, with the coefficient k being a constant, the conservation of mass at steady state becomes

$$-sD\frac{d^2N}{dx^2} = k(N_0 - N) \ , \tag{1.2}$$

where D is the vapor diffusivity. Since the phosphorus vapor pressure supplied by the PH_3 flow is many orders of magnitude higher than that of In, the former is assumed to be constant everywhere. This also makes N_0 constant. Equation (1.2) is easily solved and the solution satisfying the boundary conditions is

$$N(x) = N_0 - \left[N_0 - N(0)\right]e^{-x/L} \ . \tag{1.3}$$

In this equation the characteristic length L, given by

$$L = \sqrt{sD/k} \ , \tag{1.4}$$

is taken to be much shorter than the cover dimension, which is valid as will be shown below. By assuming a unity sticking coefficient of an In molecule impinging on InP, it can further be shown from kinetic theory that

$$k = \frac{\bar{v}}{4} \ , \tag{1.5}$$

where $\bar{v}$ is the mean thermal velocity of the In molecules. Furthermore, the diffusivity can also be related to the mean molecular velocity by [3]

$$D \cong \bar{v}\ell/3 \ , \tag{1.6}$$

where ℓ is the mean free path. By combining Equations (1.4) through (1.6), we have

$$L \cong \sqrt{\frac{4}{3}\ell s} \ . \tag{1.7}$$

Since ℓ and s are both on the order of micrometers, L is indeed much shorter than the cover dimension, and the In vapor quickly approaches the equilibrium concentration, as can be seen in Equation (1.3). Thus, the cover is indeed a very effective protection against evaporation loss.

Our earlier experiments with graphite alone as covers, however, were not entirely successful. Some InP surface roughness was often observed, especially after a high-temperature, prolonged treatment. In fact, some roughness can also be seen in the graphite-covered region in Figure 1-2(a). The problem was eventually traced to some small evaporation loss through bulk graphite, perhaps due to its porosity. Drastically improved results were consistently obtained by adding an InP cover and quartz container to stop the loss through graphite, as shown in Figure 1-1(b). Figure 1-4 presents a comparison of two InP wafers (cleaved from the same large piece) that were protected using two different covering schemes and heat treated together. The one covered only by graphite shows roughness across the entire wafer, whereas the other one has a smooth, featureless surface except for the first ~ 30 μm near the edges.

The InP covers cannot be used without graphite either. One reason for this is the possibility of fusion of the InP wafer and InP covers at points of contact. Such fusion between InP wafers during mass transport has been reported [4]. Another problem is evaporation loss and resulting surface roughness in the InP wafer (or an InP cover). When two pieces of InP are closely adjacent, growth occurs in one at the expense of the other, probably because of a small difference in equilibrium vapor pressure between them.

In a separate experiment a metallic indium melt equilibrated with added InP chips was placed on top of the graphite cover. As before, a very smooth InP wafer surface was obtained, but with occasional indium droplets on it. This can be explained by the high indium vapor pressure from the melt.

In conclusion, we have demonstrated the evaporation of In from InP during thermal annealing and the surface roughness that results from this evaporation loss. We have further shown that a smooth surface can be preserved by protecting the wafer against evaporation loss by using an effective cover. Whether evaporation can also result in other defects that can affect device reliability has not been determined.

Z.L. Liau
D.E. Mull

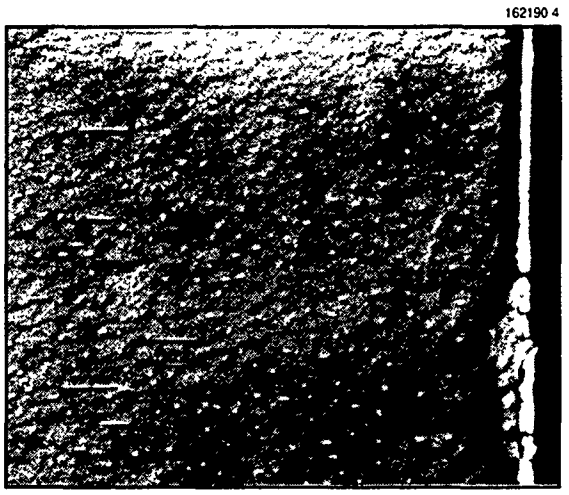

(a)

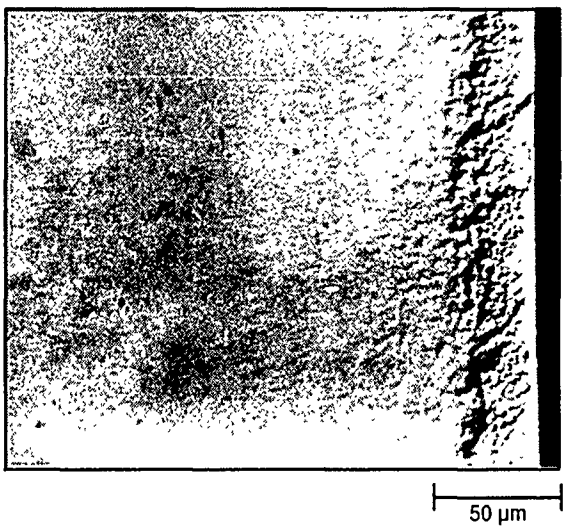

(b)

Figure 1-4. Interference-contrast optical micrographs showing surface morphologies of InP wafer covered (a) by graphite only and (b) by graphite/InP/quartz. These wafers were originally cleaved from the same piece and then heat treated together, using the respective cover schemes, at 825°C for 37 h.

1.2 20-GHZ OPTICAL ANALOG LINK USING AN EXTERNAL MODULATOR

We have demonstrated an optical analog link operating at 20 GHz with a 3-dB bandwidth of 5.2 GHz and have characterized its electrical gain, noise, and intermodulation (IM) performance. This link has an IM-free dynamic range of 108 dB-$Hz^{2/3}$ and a maximum signal-to-noise ratio (SNR) of 157 dB-Hz. Directly modulated analog links have not achieved operation at 20 GHz [5], and even in the 10-GHz frequency range, they have had 20- to 30-dB lower SNR than shown here [5],[6]. Previously reported externally modulated links have 30- to 50-dB poorer SNR than the present link [7],[8].

The optical analog link shown in the block diagram of Figure 1-5 consists of a CW laser, an integrated-optical intensity modulator, and a PIN diode detector connected together by fibers; it contains no amplifiers. The link performance was evaluated at the microwave ports, i.e., it is treated as a two-port electrical device. The diode-pumped Nd:YAG laser used in our experiment was operated CW at 1.32-μm wavelength, had relative intensity noise of < -165 dB/Hz in the 15- to 25-GHz range, and launched 120 mW into the polarization-preserving input fiber. Only a few meters of single-mode output fiber were used. The InGaAs PIN diode detector had a dc responsivity of 0.75 A/W. The Mach-Zehnder interferometric modulator, which is described more completely in [9], was fabricated on a Z-cut lithium niobate substrate using titanium-indiffused waveguides. A phase-reversed traveling-wave electrode structure was used to achieve a peak response at 21 GHz with a 7-GHz bandwidth and a switching voltage V_π at 21 GHz of ~ 9 V. A total fiber-to-fiber excess optical insertion loss of 10 dB was measured between the fiber pigtails permanently bonded to the modulator. We have demonstrated similar fiber-coupled devices with only 3 dB of excess optical loss, so substantial improvement is possible. Linear operation was achieved by biasing the modulator at the half-power point, where the output optical power was ~ 6 mW.

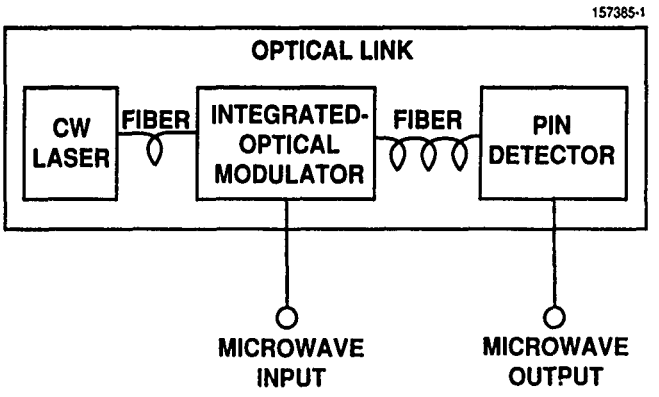

Figure 1-5. Block diagram of the optical analog link.

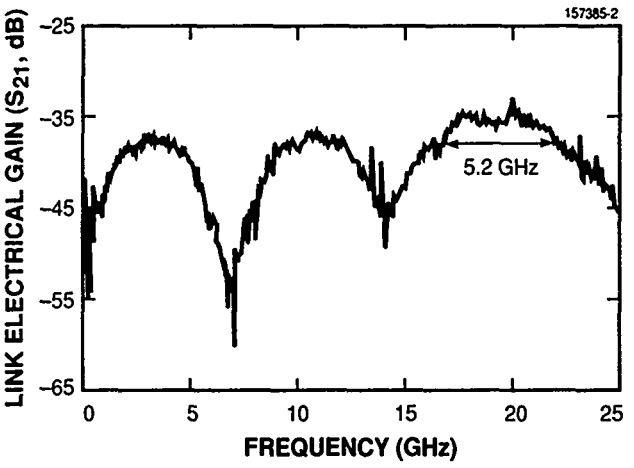

Figure 1-6. Frequency response of the optical analog link showing the electrical transmission of the link (S_{21}) measured with a network analyzer connected to the microwave ports.

Figure 1-6 shows a measurement of the electrical insertion loss of the link. The peak response and the upper 3-dB frequency are 20 and 22 GHz, respectively, compared with 21 and 24 GHz for the modulator. This difference was caused by the rapid detector response rolloff in this frequency region. At 21 GHz the detector response was 5 dB below the dc level. The noise figure, which is the degradation in SNR that occurs during transmission through the link when the only link input noise is thermal noise at 290 K, was also measured. Shot noise from the dc photocurrent (4.3 mA) at the high optical bias was the dominant link noise. In a 1-GHz band around 20.7 GHz, the measured output noise was −167 dBm/Hz (± 2 dB). With the ~ 34-dB link insertion loss, this corresponds to a noise figure of 41 dB.

Third-order IM distortion was measured by applying two signals of equal amplitude at 17.95 and 18.00 GHz and measuring the fundamentals and IM products at the link output. The results of these measurements are presented in Figure 1-7, which graphically shows several important link parameters. The IM-free dynamic range, defined as the range of input electrical power over which there is no third-order IM signal above the noise level, was 108 dB-$Hz^{2/3}$ for this link. Note that the IM-free dynamic range decreases as the two-thirds power of the noise bandwidth. The maximum SNR occurs approximately where the modulator is driven to 100 percent modulation depth (+28-dBm input power for a single frequency for this modulator); this gives an SNR of 157 dB-Hz. It is interesting to note that these values of dynamic range are very similar to those of a much lower frequency link that we demonstrated using a modulator with a considerably higher response [10], which confirms the theoretical prediction that dynamic range is independent of modulator response.

A few problems occurred with this link. The laser had multiple longitudinal modes, so there were RF noise spikes at 4.5-GHz intervals. In addition, the laser emitted at both 1319 and 1338 nm, which prevented long-distance fiber transmission at 20 GHz because of velocity dispersion. These two problems

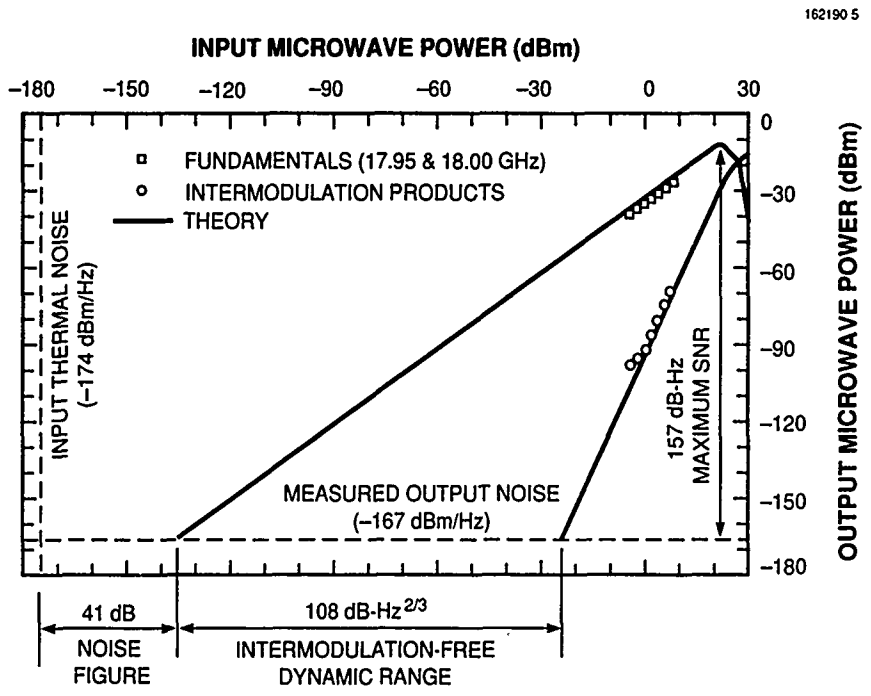

Figure 1-7. Two-tone third-order intermodulation measurement of the link with 6-mW optical bias power at the detector. The data points indicate experimental measurements. The performance numbers refer to extrapolated experimental data; the theoretical values are ~ 2 dB better.

could be overcome by using a single-frequency laser. The photorefractive effect in lithium niobate was not a problem because of the long optical wavelength [10].

In summary, we have demonstrated a 20-GHz optical analog link with an electrical insertion loss of ~ 34 dB, a noise figure of 41 dB, an IM-free dynamic range of 108 dB-$Hz^{2/3}$, and a maximum SNR of 157 dB-Hz. By simply using a single-frequency laser and improving the modulator insertion loss, this performance could be achieved with several kilometers of output fiber.

G.E. Betts C.H. Cox III
K.G. Ray

1.3 X-RAY DIFFRACTION OF InGaAs/GaAs STRAINED-LAYER MULTIPLE QUANTUM WELLS

Knowledge of heterointerface structure on the scale of interatomic distances is important for the understanding of epitaxial growth processes. Some success in acquiring such information has been obtained by x-ray diffraction analysis of superlattices where the periodic strain and/or structure factor variation causes a modulation of the Bragg reflections. Preliminary results using this technique to analyze organometallic vapor phase epitaxy (OMVPE) growth of InGaAs/GaAs multiple quantum wells (MQWs)

are reported here. This work is motivated by our need to understand the growth of GaInAsP/GaAs structures in order to optimize the switching of gases containing the group III and group V elements. The results permit some progress in separating this complex issue into its thermodynamic, growth-technique, and reactor-specific parts.

Two Lincoln Laboratory OMVPE systems with similar, state-of-the-art plumbing [11] but very different reactor tubes are presently configured to permit growth of InGaAs/GaAs strained layers. One reactor has a well-established record of state-of-the-art growth of GaAlAs/GaAs and InGaAs/GaAlAs/GaAs quantum-well lasers [12],[13]. The other reactor is on a system designed for the growth of InP-based alloys and has demonstrated excellent single-layer uniformity [14]. Currently, the latter system is being used for the growth of GaInP/GaAs laser structures. Since device structures incorporating As and P pose difficult materials growth problems, we decided to grow an all-As InGaAs/GaAs MQW structure in each of these two reactors to compare their performance.

The first reactor is in a downward-flow, rotating-disk configuration and utilizes injection through a diffuser. Susceptor rotation (~ 500 rpm) improves the layer thickness uniformity, and low-pressure operation (~ 0.2 atm) prevents formation of buoyancy-induced convection cells. The second reactor is in the chimney configuration, operating at atmospheric pressure with upward flow. It has no injection diffuser. Gases in this reactor flow through a rectangular channel of high width-to-depth ratio. A susceptor with the growth surface parallel to the flow is positioned from a sidearm attached to the rectangular tube. Susceptor rotation is used to achieve good deposition uniformity, but the rate is kept low enough (< 100 rpm) so as not to alter the flow.

Figures 1-8 and 1-9 show x-ray rocking curves for InGaAs/GaAs MQWs grown with the first and second reactor, respectively. The nominal structures grown were five 10-nm wells of $In_{0.15}Ga_{0.85}As$ between 50-nm GaAs barriers. The GaAs substrates were oriented 2° off (001) toward [011]. Trimethylgallium, trimethylindium, and AsH_3 were used as sources, and growth was made at ~ 650°C. The x-ray data are of the (004) reflection with CuK_α radiation (0 arc sec corresponding to a Bragg angle of 33°) taken with a double-crystal diffractometer operated in the (+, −) parallel configuration.

Below each experimental curve is a simulated rocking curve generated with commercial software [15] based on the Taupin-Tagachi solution to the dynamical x-ray problem. Each simulated curve is scaled to match the maximum intensity peak, which is attributable to the substrate. As can be seen, other than some observed background radiation off the Bragg angle, the fit is good. In particular, essentially all of the predicted structure is seen, and the observed satellite intensities and widths follow those predicted from the idealized structure. As pointed out by Quillec et al. [16], for sufficient strain the rocking curve of the strained-layer MQW consists of a periodic set of satellites whose peak intensities fall under two modulation envelopes. One envelope (at negative angles in this case) is associated with the alloy of the well, and the other (at zero here) is associated with that of the barrier.

The following procedure was used to find the parameters that give a good fit. First, the period of oscillations in the rocking curve is fixed by the MQW period, the sum of a well and barrier spacing, $t_w + t_b$. Second, the separation between the substrate peak and the $n = 0$ satellite is determined by the average In concentration, $\langle x \rangle = x t_w/(t_w + t_b)$, with x being the concentration in the well. The $n = 0$ peak is

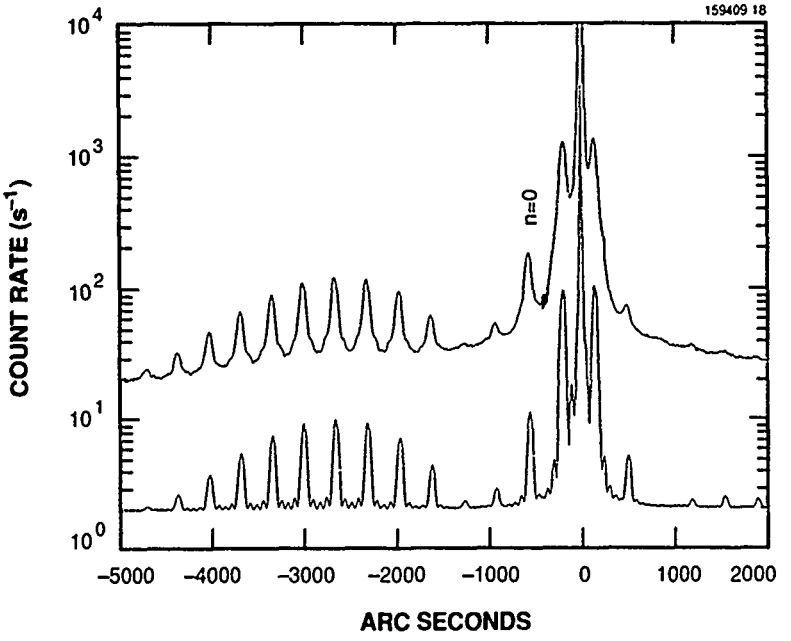

Figure 1-8. Rocking curve of a five-period strained layer grown with a low-pressure, rotating-disk reactor. Lower curve is a simulation using t_w = 9.6 nm, t_b = 45.0 nm, and x = 0.17, which is shifted by 10× for clarity.

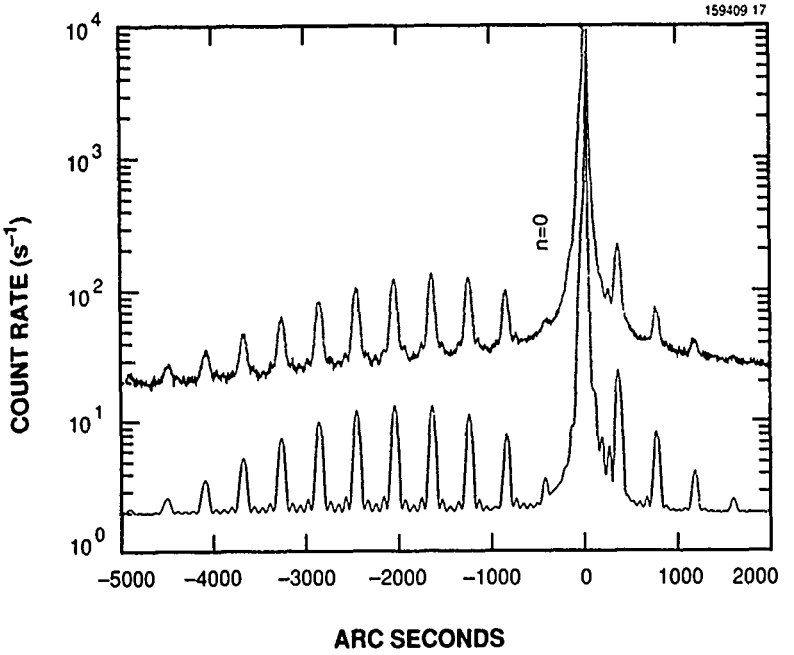

Figure 1-9. Rocking curve of a five-period strained layer grown with a chimney reactor. Lower curve is a simulation using t_w = 7.4 nm, t_b = 39.0 nm, and x = 0.16, which is shifted by 10× for clarity.

labeled in each figure; that identification is readily made knowing the nominal MQW structure. With the period determined, measurement of this separation then specifies the product xt_w. By holding xt_w fixed but changing x, it is possible to correctly fix the position of the modulation envelope associated with the InGaAs. The derived parameters that give the simulated rocking curves are $t_w = 9.6$ nm, $t_b = 45.0$ nm, and $x = 0.17$ (Figure 1-8), and $t_w = 7.4$ nm, $t_b = 39.0$ nm, and $x = 0.16$ (Figure 1-9).

It has been conjectured that, because of its relatively large atomic size, indium accumulates at the growth surface. If this happens, one might anticipate a graded region at the start of the well, with x changing from ~ 0 to ~ 0.15. To test the sensitivity of the rocking curve to this expectation, simulated curves have been generated with a graded region, keeping the period and the position of the $n = 0$ peak fixed. For a graded region wider than 2.5 nm the position and shape of the modulation envelope changes, and the fit in Figures 1-8 and 1-9 noticeably deteriorates.

To a certain degree, the upper limit on this grading could be reduced by growing narrower wells. However, a narrowing of the well broadens the envelope associated with the well and at some point merges it with the envelope associated with the barrier. This trend can be seen in the comparison between Figures 1-8 and 1-9. It is important to keep the envelopes separated because the shape of the envelope associated with the well is used to obtain the information on the grading. As the well is narrowed, it is then necessary to increase x to maintain this condition. Wells of 5-nm thickness should be usable for this purpose, but those of 2.5-nm width probably require more indium than can be incorporated without strain relaxation due to dislocation generation.

In summary, a preliminary x-ray diffraction study has been made on InGaAs/GaAs strained-layer MQW structures grown in two very different reactors. The diffraction curves from these growths are similar in overall appearance, and the good agreement between the simulated rocking curves for idealized structures and the experimental data is interpreted as evidence that both reactors are producing near-ideal structures. For these structures with ~ 10-nm wells, it can be said that an upper limit on the width of a possible graded region is 2.5 nm.

S.H. Groves S.C. Palmateer
D.R. Calawa C.A. Wang

REFERENCES

1. Z.L. Liau and D.E. Mull, Solid State Research Report, Lincoln Laboratory, MIT, 1987:3, p. 11. DTIC AD-192837.
2. D.E. Gray (ed.), *American Institute of Physics Handbook*, 3rd ed. (McGraw-Hill, New York, 1972), Sec. 4, p. 298.
3. F. Reif, *Fundamentals of Statistical and Thermal Physics* (McGraw-Hill, New York, 1965), p. 485. The equation quoted is for self-diffusion and is only a crude approximation for the present case, which is the diffusion of In molecules in an essentially H_2 atmosphere.
4. Z.L. Liau and D.E. Mull, *Appl. Phys. Lett.* **56**, 737 (1990).
5. H. Blauvelt and K. Lau, *Proc. SPIE* **995**, 106 (1988).
6. H. Blauvelt, D.B. Hiff, G.J. Stern, and I.L. Newberg, *Proc. SPIE* **1102**, 70 (1989).
7. J.J. Pan, Y.F. Liang, and M. Shih, *Conf. Lasers Electro-optics Tech. Dig.* (Optical Society of America, Washington, D.C., 1988), Paper TuP3.
8. I.L. Newberg, C.M. Gee, G.D. Thurmond, and H.W. Yen, *MTT-S Microwave Symp. Tech. Dig.* (IEEE, New York, 1989), Paper U-3.
9. G.E. Betts, *Topical Mtg. Integrated and Guided Wave Optics Tech. Dig.* (IEEE, New York and Optical Society of America, Washington, D.C., 1989), Paper MAA4.
10. G.E. Betts, L.M. Johnson, C.H. Cox III, and S.D. Lowney, *IEEE Photon. Technol. Lett.* **1**, 404 (1989).
11. Thomas Swan & Co., Ltd.
12. C.A. Wang, H.K. Choi, and M.K. Connors, *J. Electron. Mater.* **18**, 695 (1989).
13. C.A. Wang and H.K. Choi, to be published in *IEEE J. Quantum Electron.*
14. S.C. Palmateer, S.H. Groves, J.W. Caunt, and D.L. Hovey, *J. Electron. Mater.* **18**, 645 (1989).
15. Bede Scientific Instruments, Ltd., "Rocking Curve Analysis by Dynamical Simulation" software.
16. M. Quillec, L. Goldstein, G. LeRoux, J. Burgeat, and J. Primot, *J. Appl. Phys.* **55**, 2904 (1984).

2. QUANTUM ELECTRONICS

2.1 HIGH-POWER SEMICONDUCTOR LASER AMPLIFIERS

We are investigating a master-oscillator/power-amplifier (MOPA) system using a single-pass semiconductor laser amplifier. The advantages of a traveling-wave amplifier over high-power external-cavity lasers or injection-locked oscillators include simplicity, lack of chirp under pulsed conditions, resistance to parasitic oscillations in undesirable cavity modes, and broad wavelength agility.

The broad-area (500 μm wide × 1000 μm long) amplifiers are fabricated from GaAs/GaAlAs material with a graded-index separate-confinement heterostructure single-quantum-well (GRIN-SCH SQW) design. The material was grown by organometallic vapor phase epitaxy. The amplifier chips are mounted on diamond-turned heat sinks that provide nonvignetted optical access to both facets. The output of an uncoated device, used as a laser, is shown as a function of drive current in Figure 2-1. After mounting, both facets of the amplifier are antireflection coated to inhibit lasing under high-current conditions. This typically increased the lasing threshold current from 1.3 to 10 A.

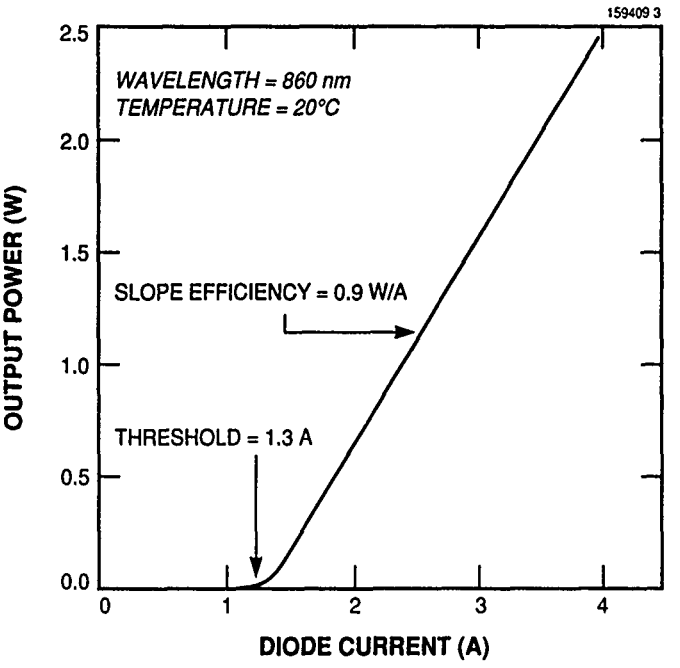

Figure 2-1. Performance of a broad-area diode laser prior to antireflection coating. Power and slope efficiency are given for double-ended output.

A CW Ti:Al_2O_3 laser was used as the master oscillator in these experiments and was mode matched into the diode-amplifier waveguide with a coupling efficiency as high as 50 percent. By tuning the Ti:Al_2O_3 laser below the absorption edge of the GaAs quantum well (at 860 nm) we were able to check the laser's alignment and coupling efficiency and to probe the distortion of the input beam caused by the waveguide under pumped and unpumped conditions.

With an amplifier current of 4 A, we have achieved 1 W of CW output power for an estimated 70 mW launched into the amplifier at a wavelength of 850 nm. The CW performance of the laser amplifier as a function of input power is shown in Figure 2-2. The CW measurements were limited to currents of no more than 4 A because of inadequate heat sinking. The small-signal gain of the amplifier was substantially saturated for pulsed currents greater than 6 A. We attribute this to band-filling. The large-signal bandwidth under pulsed conditions was 45 nm. It was slightly less with CW pumping. A multiple-quantum-well design should improve the small-signal gain with only a minor decrease in the large-signal bandwidth.

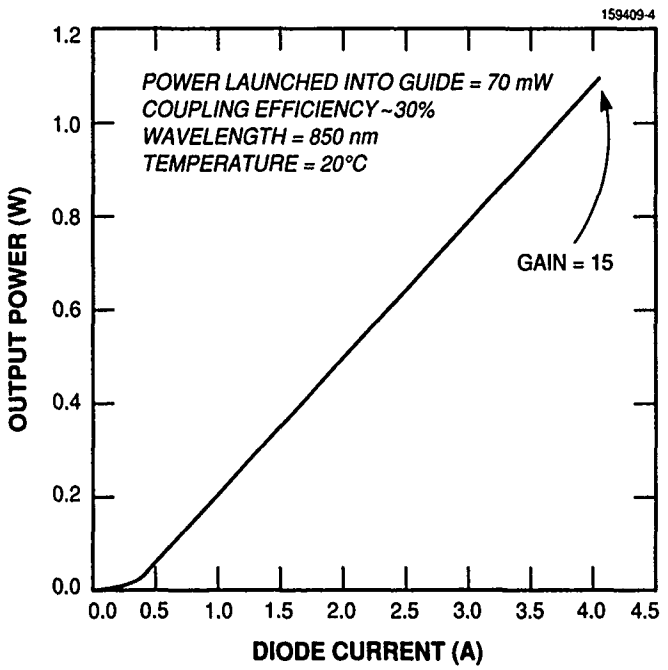

Figure 2-2. CW performance of a laser amplifier as a function of input power.

The output of the amplifier was contained in a spatially uniform beam with no pedestal or spurious modes. The transverse mode quality of the output beam was determined by comparing the results of a scanning-knife-edge test, with clip levels of 10 and 90 percent, with the expected results for a Gaussian beam. These measurements indicated that during amplification the beam quality was degraded by no more than a factor of 2 in the dimension parallel to the diode junction (the lateral dimension). In the

dimension perpendicular to the junction (the narrow waveguide dimension), the waveguide acted as a spatial filter and very little change in beam quality was observed. The transmitted beam from an unpumped diode amplifier was 1.8 times diffraction limited in the lateral dimension, as determined primarily by the quality of the master-oscillator beam.

The present results indicate that amplifier devices 1 mm wide by 2 mm long could produce as much as 5 W of CW output in a high-quality spatial mode.

C.D. Nabors
R.L. Aggarwal
H.K. Choi
C.A. Wang
A. Mooradian

2.2 PUMPING OF Yb:YAG LASER WITH InGaAs DIODE LASER

A 0.97-μm strained-layer InGaAs diode laser has been used to pump a 1.03-μm Yb:YAG laser. This diode-pumped laser system offers a number of advantages over AlGaAs-pumped Nd^{3+} lasers, including lower thermal loading of the solid state gain medium and broad absorption features in Yb:YAG that permit less stringent temperature control of the diode laser.

Figure 2-3 shows the absorption spectra for both Yb:YAG and Nd:YAG in their respective pump bands. The main absorption feature in Yb:YAG has a bandwidth of 18 nm full width at half-maximum (FWHM) compared with ~ 3 nm for Nd:YAG, thus reducing the requirement for wavelength selection of the diode pump lasers and increasing their operational temperature range. We estimate that thermal loading per unit output power in Yb:YAG should be at least three times less than in Nd:YAG when operating CW, and at least five times less when operating in an energy storage mode, thereby reducing problems with thermal focusing and stress-induced birefringence in the solid state laser. The upper-state lifetime of Yb:YAG is five times longer than that of Nd:YAG (1.2 ms versus 240 μs), and thus fewer pump diodes are needed per unit output energy when operating in a pulsed mode. In addition, InGaAs diode lasers may be better pump sources than AlGaAs diode lasers. InGaAs lasers with high efficiency and low threshold current density have been reported [1], and life tests indicate higher reliability and longer lifetime than for AlGaAs diodes [2].

There are disadvantages with Yb:YAG lasers as well. We have measured the effective stimulated emission cross section to be ~ 1.7×10^{-20} cm^2 at 1.03 μm in Yb:YAG, which is about 20 times less than that in Nd:YAG. This may be a problem in short-pulse operation since the saturation fluence approaches the damage fluence of some optical components. The other disadvantage is that this laser is quasi-three-level at room temperature, i.e., the lower laser level is significantly populated in thermal equilibrium at room temperature, resulting in a higher threshold. Previously, Yb^{3+} lasers have been cooled below room temperature to lower the laser threshold. However, it has been shown that efficient operation of quasi-three-level lasers can be obtained [3].

A liquid-nitrogen-cooled Yb:YAG laser pumped by light-emitting diodes had previously been reported [4]. We have used a single InGaAs diode laser to demonstrate end-pumped Yb:YAG laser operation at temperatures up to 210 K. We have also used the output of a Ti:Al_2O_3 laser to demonstrate high slope efficiency in Yb:YAG. Figure 2-4 shows experimental results from a liquid-nitrogen-cooled Yb:YAG

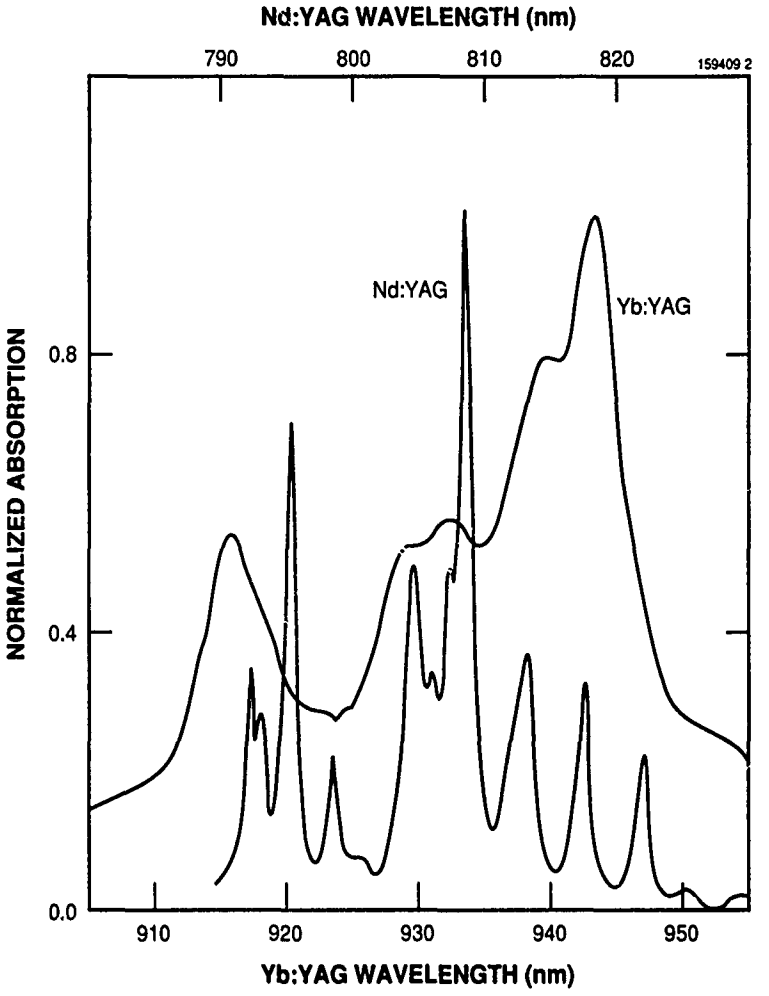

Figure 2-3. Absorption spectra of Yb:YAG at its main peak near 940 nm and of Nd:YAG near 810 nm. Both spectra have their absorption peaks normalized to 1.

laser pumped by an InGaAs laser operating at 970 nm and by a Ti:Al_2O_3 laser operating at 941 nm. For the InGaAs-pumped laser the transmission of the output coupler was 1 percent and for the Ti:Al_2O_3-pumped laser it was 3 percent. The poorer slope efficiency in the diode-pumping experiments was due to lower output coupling and poorer spatial overlap between the pumped volume and the laser mode. As the temperature of the Yb:YAG laser was allowed to rise, operation was obtained up to 210 K. The threshold of the laser rises with temperature because of the filling of the lower laser level and the reduced gain cross section resulting from linewidth broadening. In this experiment, the pump power was limited by poor transmission, 48 percent, of the 970-nm pump radiation through a cavity mirror. With more pump power and a better match of the pump volume to the laser mode, efficient diode-pumped room-tempera-

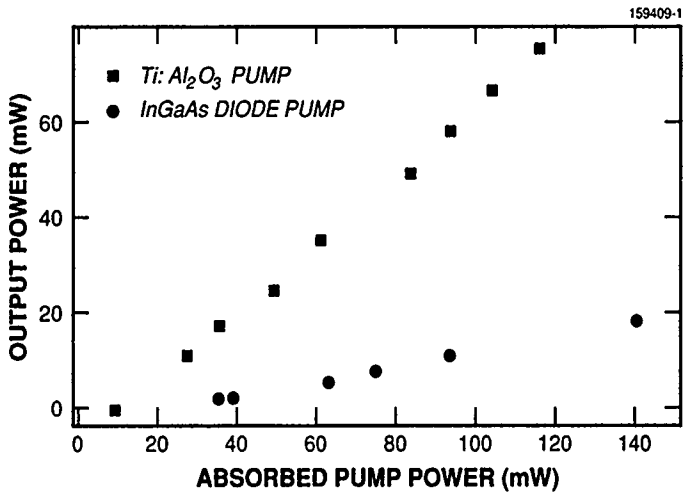

Figure 2-4. Output power as a function of absorbed pump power for both an InGaAs-pumped and a Ti.Al_2O_3-pumped Yb:YAG laser. The InGaAs laser is operating at 970 nm and the Ti:Al_2O_3 laser at 941 nm.

ture operation should be possible. To this end, the Yb:YAG laser should be pumped with multiple diodes [5] operating at 940 nm, which is a better pump wavelength because of the larger bandwidth of the 940-nm Yb:YAG absorption feature compared with that of the 970-nm feature.

In summary, we have demonstrated an InGaAs-diode-pumped Yb:YAG laser at temperatures up to 210 K, and a Ti:Al_2O_3-pumped Yb:YAG laser with a slope efficiency of 67 percent at 77 K. Improvements in the pumping of this laser should allow efficient room-temperature operation.

P. Lacovara
T.Y. Fan

2.3 GAIN-SWITCHED DIODE-PUMPED MICROCHIP LASERS

Gain-switched operation of microchip lasers has previously been demonstrated using a pulsed Ti:Al_2O_3 laser as a pump [6]. In those experiments the pump had a peak power in excess of 100 W, a power level difficult to obtain with diode lasers. Here, we report the gain-switched operation of a microchip laser pumped with an AlGaAs diode laser. The diode laser had a peak power of 0.5 W and was butt coupled to a 1.32-μm microchip laser. The microchip laser was constructed from 1.3-wt.% Nd:YAG, with a cavity length of 1 mm and a 1 percent output coupler. The output of the microchip laser was monitored with a Ge avalanche photodiode.

Rate-equation analysis indicates that the width of the output pulse generated in a gain-switched system is determined largely by the population inversion density that can be obtained during the pulse buildup time. In order to obtain the maximum population inversion in the microchip laser, the pump laser

should be biased below the microchip laser threshold. The output of the pump should then be quickly increased to its maximum power and maintained at that level until the output pulse of the microchip laser develops, whereupon it should be quickly reduced to below the microchip laser threshold to prevent the formation of a second pulse. Experimentally, these conditions were obtained by driving the diode pump laser with the superposition of a square wave and a dc component. The output of the microchip laser was monitored as the dc level and the frequency of the square wave were adjusted to obtain the narrowest pulses, without double pulsing. The magnitude of the square wave was maintained so that the maximum output from the diode laser was 0.5 W, its maximum rated power. The resulting diode output, shown in Figure 2-5, is a 100-kHz, 0.4-W (peak-to-peak) square wave superimposed on an average dc output power of 0.3 W. The corresponding microchip laser output, a 100-kHz train of 170-ns pulses, is shown in Figures 2-6 and 2-7. The long tail of the pulse shown in Figure 2-7 is an artifact of the detector. The average output power of the microchip laser was measured to be 30 mW, with a peak output power of 1.8 W.

Diode-pumped, pulsed operation of microchip lasers is also possible if the microchip lasers are CW pumped and then Q-switched once a sufficient inversion density is obtained. Computer modeling indicates that with a 500-mW diode pump it should be possible to obtain Q-switched pulses as short as 250 ps, with peak powers of several kilowatts, from a Nd:YAG microchip laser.

J.J. Zayhowski
J. Keszenheimer

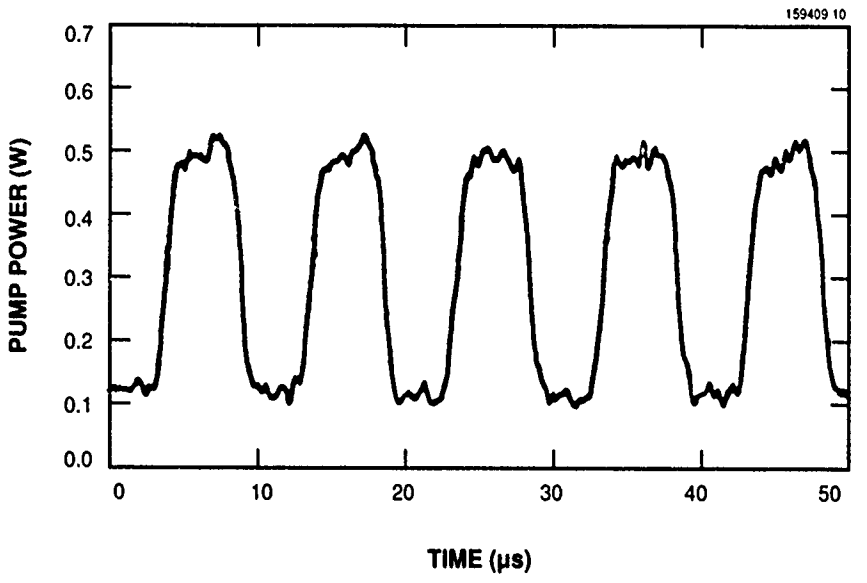

Figure 2-5. Diode output used to pump a 1.3-µm, gain-switched, Nd:YAG microchip laser.

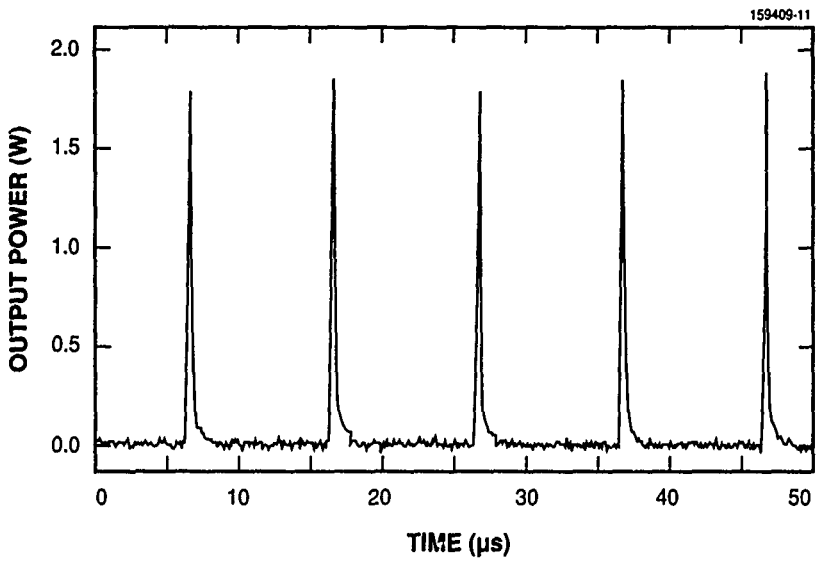

Figure 2-6. Train of output pulses obtained from a 1.3-µm, gained-switched, diode-pumped, Nd:YAG microchip laser.

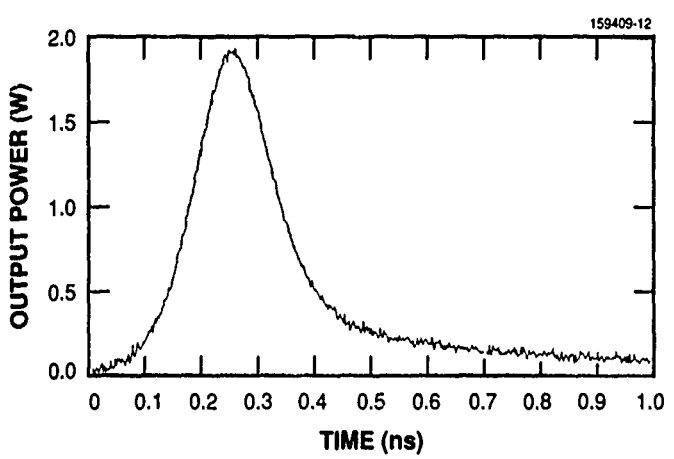

Figure 2-7. Output pulse from a 1.3-µm, gain-switched, diode-pumped, Nd:YAG microchip laser.

2.4 TEMPORAL, SPECTRAL, AND COHERENCE PROPERTIES OF A Ti:Al_2O_3 MASTER-OSCILLATOR/POWER-AMPLIFIER SYSTEM

We have constructed a longitudinally pumped, multistage Ti:Al_2O_3 MOPA system designed to produce pulsed (10 Hz), tunable radiation from 750 to 850 nm. With this system we have obtained ~ 100-ns, single-frequency output with 0.38 J per pulse at 800 nm. The design and operation [7] and the beam quality [8] of the Ti:Al_2O_3 MOPA system have been reported previously. Its temporal, spectral, and coherence properties are characterized here.

The Ti:Al_2O_3 MOPA system consists of a CW, single-frequency, TEM_{00}-mode Ti:Al_2O_3 ring laser as a master oscillator and four Ti:Al_2O_3 amplifier stages. Each amplifier stage is a single Brewster-cut Ti:Al_2O_3 crystal pumped by a pulsed (10 Hz), frequency-doubled Nd:YAG laser in a nearly collinear geometry. Several of the Ti:Al_2O_3 amplifier stages are multipassed to increase the signal gain. The overall signal gain of the system is ~ 2×10^7.

The shot-to-shot variation of the Ti:Al_2O_3 MOPA output is shown for 15 consecutive pulses in Figure 2-8. The pulses have been overlapped for ease of comparison. The pulse width of an individual pulse is 115 ns FWHM. The amplitude jitter is < 10 percent and the temporal jitter is ~ 20 ns. The pulses are smooth and show no structure when observed with a temporal resolution of 8 ns. (The bandwidth of our oscilloscope is 125 MHz.)

For a preamplifier, where the signal is typically in the small-signal gain regime, small variations in pump energy P lead to large variations in the pulse amplitude A, since $A \propto \exp(CP)$, where C is a constant that depends on variables such as the gain coefficient and the number of passes through the gain region. The reason for the small amplitude jitter in our Ti:Al_2O_3 MOPA is that we are saturating the gain in the last amplifier stage. This can be demonstrated by measuring the output of the last stage at $\lambda = 800$ nm as a function of the 532-nm pump energy into that stage (with constant pump energy into stages 1 to 3). The results of these measurements are shown in Figure 2-9, where the curve becomes linear at pump energies of ~ 300 mJ, indicating gain saturation and power extraction. The slope efficiency calculated from the linear portion of the curve is 30 percent, which compares favorably with detailed computer modeling of our system.

The Ti:Al_2O_3 MOPA was tuned using a mechanical, three-plate, birefringent filter in the master oscillator and leaving all other parameters unchanged. The output energy as a function of wavelength is shown in Figure 2-10, where the data indicate that the system is broadly tunable. Over the range from 760 to 825 nm the energy per pulse varied by ~ 33 percent. The energy meter was placed 1.7 m away from the output of the last Ti:Al_2O_3 amplifier stage. The reason for the relatively constant energy per pulse is again that we are saturating the gain in the final amplifier stage.

One limitation on the tuning of the Ti:Al_2O_3 MOPA was the mirrors used in its construction. While it is not difficult to obtain mirrors that have high reflectivity from 750 to 850 nm, it is difficult to obtain broadband mirrors that can also withstand high energies. For a system with ~ 30 mirrors, a loss of 1, 2, and 5 percent per mirror leads to a total loss of 26, 45, and 79 percent, respectively.

Amplified spontaneous emission (ASE) is another potential limitation on the tuning range of the Ti:Al_2O_3 MOPA. This occurs when spontaneous emission at the input to the preamplifier multiplied by

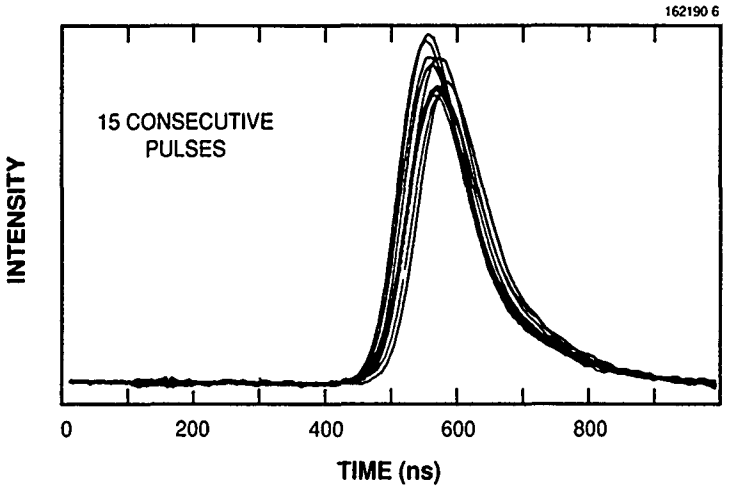

Figure 2-8. Output of the Ti:Al_2O_3 master-oscillator/power-amplifier (MOPA) system for 15 consecutive pulses. The pulse length is 115 ns FWHM. The amplitude jitter is < 10 percent and the temporal jitter is ~ 20 ns. The pulse is smooth and shows no structure.

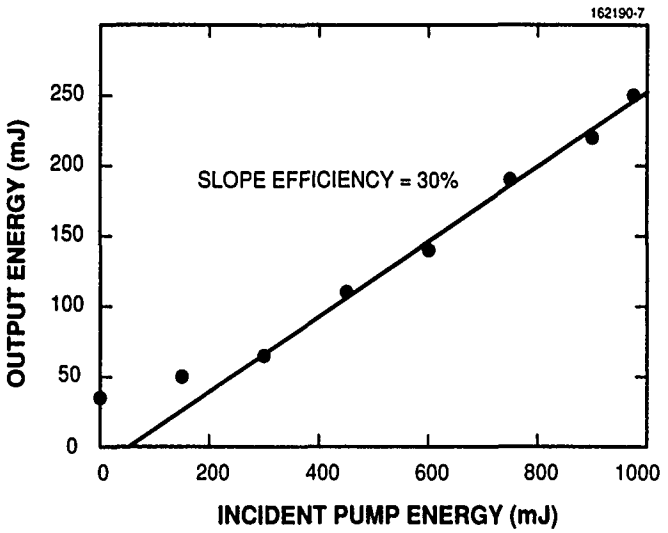

Figure 2-9. Output of the last stage of the Ti:Al_2O_3 MOPA at λ = 800 nm as a function of the 532-nm pump energy into the stage (with constant pump energy into stages 1 to 3). The curve becomes linear at a pump energy of ~ 300 mJ, indicating gain saturation and power extraction. The slope efficiency calculated from the linear portion of the curve is 30 percent.

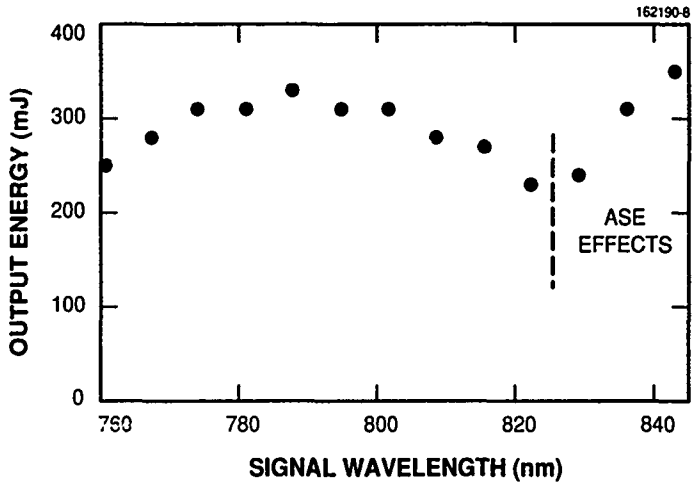

Figure 2-10. Output energy per pulse as a function of wavelength for the Ti:Al_2O_3 MOPA. From 760 to 825 nm the energy per pulse varies by ~ 33 percent. For signal wavelengths greater than 825 nm the output energy increases with increasing wavelength rather than decreases as would be expected from the gain profile of Ti:Al_2O_3. This increase is due to the onset of ASE, which contributes to the total output energy.

the integrated gain through the Ti:Al_2O_3 amplifier system is comparable to the signal output at the master-oscillator wavelength. In particular, the problem becomes evident when the master oscillator is tuned to a wavelength off of the peak (~ 800 nm) of the gain profile, where both the output of the master oscillator and the gain of the Ti:Al_2O_3 amplifier system decrease. The ASE occurs at the peak of the gain profile over a broad range of wavelengths.

Figure 2-10 shows that for signal wavelengths greater than 825 nm the output energy of the Ti:Al_2O_3 MOPA increases with increasing wavelength rather than decreases as would be expected from the gain profile of Ti:Al_2O_3. This increase is due to the onset of ASE, which begins to contribute to the total energy output by the Ti:Al_2O_3 MOPA. The output intensity as a function of wavelength near the center of the gain profile (758 to 818 nm) was measured when the master oscillator was tuned to 843 nm. A broad, spikey output was observed, which is characteristic of ASE. Limitations on the tuning range due to ASE can be reduced by spatial or spectral filtering.

Coherence of the Ti:Al_2O_3 MOPA output was demonstrated by interfering a sample of the master-oscillator output with a sample of the Ti:Al_2O_3 MOPA output. During a pulse, the intensity of the interference signal changed from a minimum to a maximum, indicating a phase change $\Delta\phi$ of π. The time Δt in which this occurred was on the order of 250 ns, yielding a maximum frequency change of $\omega = \Delta\phi/\Delta t = 1.3 \times 10^7$ rad/s, or $\nu = \omega/2\pi = 2$ MHz. Frequency changes are expected to occur in pulsed Ti:Al_2O_3 amplifiers because the index of refraction depends upon the inverted population of Ti^{3+} ions [9] and the temperature, neither of which are constant during the pulse.

In conclusion, we have observed pulses of 115 ns FWHM with small pulse-to-pulse amplitude jitter from a Ti:Al_2O_3 MOPA system. The energy per pulse remained relatively constant when tuning the master oscillator from 760 to 825 nm. For wavelengths greater than 825 nm, ASE is an issue. The

coherence properties have been tested, and we observed a small frequency change of 2 MHz due to both temperature- and population-induced changes in the index of refraction of the Ti:Al_2O_3.

K.F. Wall
P.A. Schulz
R.A. Aggarwal
P. Lacovara
A. Walther
V. Daneu
A. Sanchez

2.5 ULTRAFAST ALL-OPTICAL SWITCHING WITH HIGH-EFFICIENCY NONDEGENERATE FOUR-WAVE MIXING

The conventional approach to exploiting third-order nonlinearities for ultrafast all-optical switching is to detect a change induced in one optical pulse, the probe or data pulse, by a second optical pulse, the pump or clock pulse. This change can be detected as an amplitude modulation proportional to exp $(-2\mathrm{Im}\chi^{(3)}\phi)$ where $\chi^{(3)}$ is the third-order nonlinear susceptibility and ϕ is an interaction parameter, or as a phase shift [10],[11] in which the signal is proportional to $\cos^2(\mathrm{Re}\chi^{(3)}\phi/2)$. In either case, parasitic intensity modulations are undesirable and usually make detection of the signal difficult. In GaAs, which has one of the largest-broadband $\chi^{(3)}$'s known at wavelengths near 0.9 μm, $\mathrm{Im}\chi^{(3)}$ is comparable to $\mathrm{Re}\chi^{(3)}$ [12], implying tnat an induced phase shift of π is accompanied by an undesirable intensity attenuation of $\sim e^{-2\pi}$. The bandgap resonances of GaAs can be exploited to obtain a more favorable $\mathrm{Re}\chi^{(3)}/\mathrm{Im}\chi^{(3)}$ ratio. However, the resultant optically generated carriers also cause stimulated Raman scattering and other long-lived phenomena that dominate over the ultrafast effects. Furthermore, since the switches must ultimately operate with picosecond pulses, the inevitable nonlinearly induced chirp and pulse-shape distortion would be a serious source of noise.

Nondegenerate four-wave mixing (NDFWM) is a third-order nonlinear process with a signal proportional to $|\chi^{(3)}\phi|^2$ and zero background [12]. As illustrated in Figure 2-11(a), when a clock pulse of optical frequency ω_1 is coincident with a data pulse of optical frequency ω_2 in a nonlinear medium, a Stokes or anti-Stokes wave is generated at a new frequency $\omega_3 = 2\omega_1 - \omega_2$. The signal at ω_3 acts as an AND-gate output of the data and the clock. Thus, time-division multiplexing/demultiplexing of picosecond optical data pulses in a high-bit-rate optical trunk line can be achieved by using a low-repetition-rate local clock. Using a 0.5-mm-long GaAs/AlGaAs quantum-well waveguide as the nonlinear medium, we have observed Stokes-wave powers as high as 5 percent of the probe for a pump pulse of 5 ps and 12-W peak power, as shown in Figure 2-11(b). This 5 percent figure for NDFWM conversion efficiency is, to the best of our knowledge, several orders of magnitude larger than the efficiencies obtained in any other nonlinear nonresonant waveguides except for silica fibers. It is the consequence of a large-broadband $\chi^{(3)}$ and a small phase mismatch [13]. In this system, the pump and probe frequencies can be tuned over a 5-THz bandwidth without substantial signal degradation. For a frequency difference of ~ 1 percent, gratings or dichroic mirrors can be used to discriminate between the Stokes signal and the pump and probe signals. In our experiment, a 1-m spectrometer was used and the signal-to-noise ratio was detector limited at greater than 10^4.

Several advantages of the four-wave mixing scheme relative to other schemes are shown in Figures 2-12(a) and 2-12(b). While the transmitted probe pulse is highly susceptible to thermal and carrier

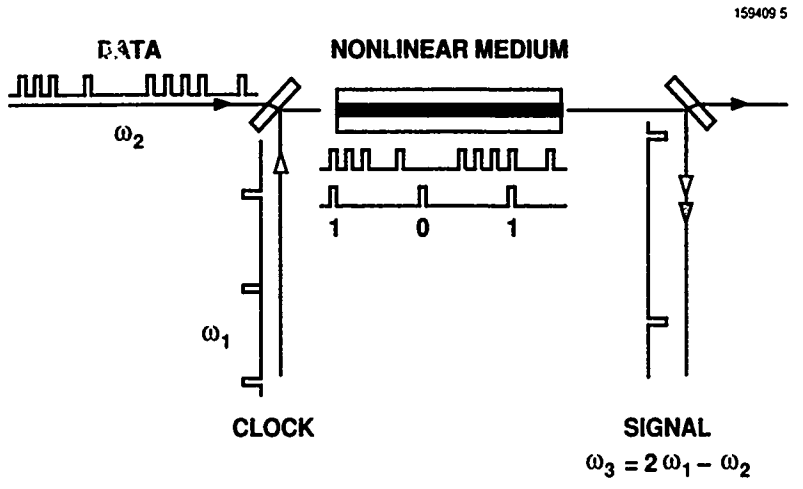

(a)

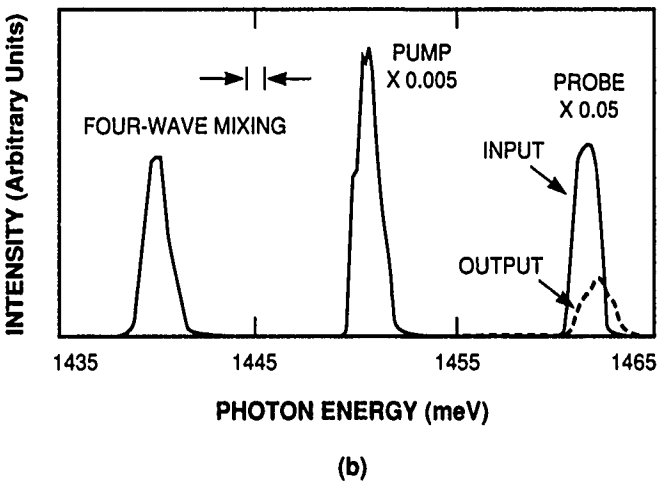

(b)

Figure 2-11. (a) Scheme for nonlinear optical switching using nondegenerate four-wave mixing. The coincidence of a data pulse of optical frequency ω_2 and a clock pulse of frequency ω_1 in a nonlinear medium results in a Stokes or anti-Stokes signal at frequency $\omega_3 = 2\omega_1 - \omega_2$, creating an AND gate. By varying the delay of the clock pulses or by employing different optical frequencies, different data channels, all carried by the same trunk line, can be multiplexed or demultiplexed. (b) Spectrum of the output of the nonlinear waveguide. Conversion efficiency is defined with respect to the input power of the probe beam.

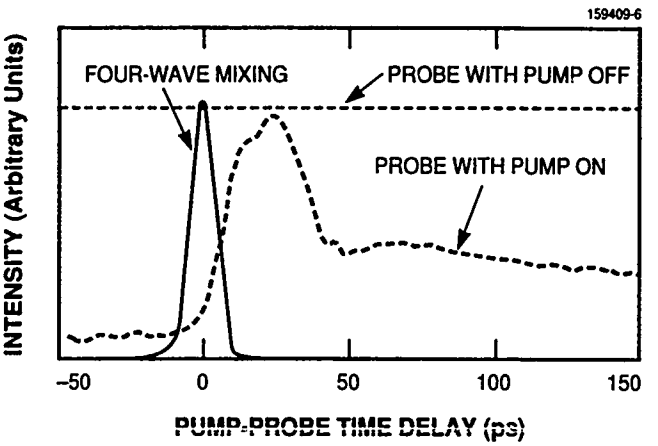

(a)

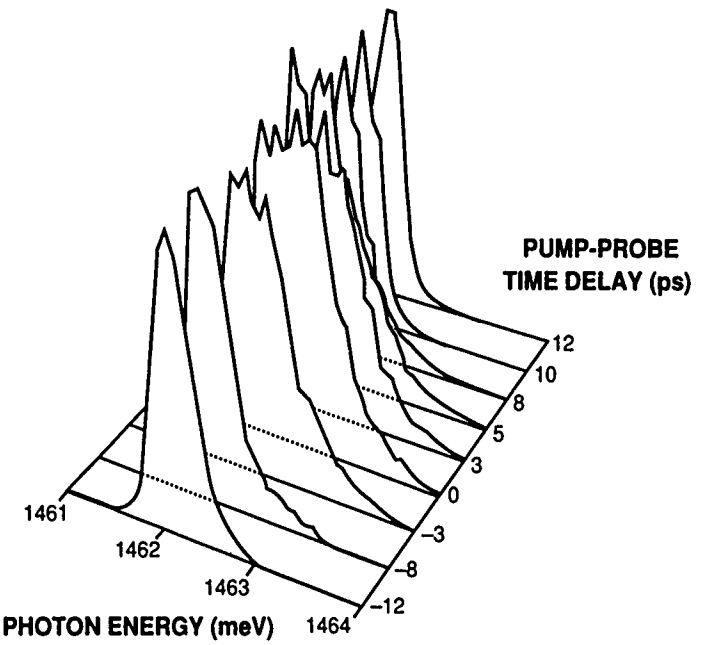

(b)

Figure 2-12. (a) Transmitted power of the probe beam (dashed curve) and amplitude of the four-wave mixing signal (solid curve) as a function of the pump-probe time delay. The probe intensity is shown attenuated by a factor of 20. Since the pump pulses are periodic and separated by 12.5 ns, the effect for a negative delay time (the probe pulse arrives before the pump pulse) is actually the effect at 12.5 ns after a previous pulse. (b) Normalized spectra of the output probe beam for different pump-probe time delays, showing nonlinearly induced chirps. The largest chirp shows a net phase shift of $\sim 0.2\pi$.

effects, evidenced by both nanosecond-long effects immediately following a pump pulse and quasi-steady-state effects at ~ 12.5 ns later, the coherent NDFWM process remains background free and ultrafast [Figure 2-12(a)]. The problem of cross-phase-modulation chirp is also evident in Figure 2-12(b), which in conjunction with material dispersion leads to substantial pulse-shape distortion. With its amplitude affected by optically excited carriers, and its frequency being chirped, the probe pulse is not a suitable carrier for interferometric detection of the nonlinear optical phase shift. On the other hand, the detection of the background-free NDFWM signal is tolerant to fluctuations in pump-pulse power, shape, and frequency.

The 5 percent nonlinear conversion efficiency obtained in our experiments is not much lower than the 25 percent value obtained in silica fibers [14]. The comparison is more meaningful, however, when the peak power levels used are considered. The fiber experiments used a 10^3-W peak pump power, a level far more demanding than the 12-W level used in our experiments. This level, adjusted for optical mode size and coupled with the length advantage of the fibers, results in an interaction parameter ϕ that is 10^5 times larger for the fibers, yet the much larger $\chi^{(3)}$ of GaAs/AlGaAs compensates for this difference quite adequately. Furthermore, we have not fully utilized the phase-matching bandwidth of the GaAs/AlGaAs waveguide. With a 5-mm-long GaAs/AlGaAs waveguide and a few watts of peak power, we anticipate complete parametric interaction, where the pump beam serves not only as an optical gate pulse but also to amplify the probe beam, replenishing the system loss for a truly lossless optical gate.

H.Q. Le H.K. Choi
S. DiCecca C.A. Wang

REFERENCES

1. H.K. Choi and C.A. Wang, *Conf. Lasers Electro-optics Tech. Dig.* (Optical Society of America, Washington, D.C., 1990), Paper CMH2.

2. D.P. Bour, D.B. Gilbert, K.B. Fabian, J.P. Bednarz, and M. Ettenberg, *IEEE Photon. Technol. Lett.* **2**, 173 (1990).

3. T.Y. Fan and R.L. Byer, *IEEE J. Quantum Electron.* **QE-23**, 605 (1987).

4. A.R. Reinberg, L.A. Riseberg, R.M. Brown, R.W. Wacker, and W.C. Holton, *Appl. Phys. Lett.* **10**, 11 (1971).

5. T.Y. Fan, A. Sanchez, and W.E. DeFeo, *Opt. Lett.* **14**, 1057 (1989).

6. J.J. Zayhowski, J. Ochoa, and A. Mooradian, *Opt. Lett.* **14**, 1318 (1989); Solid State Research Report, Lincoln Laboratory, MIT, 1989:2, p. 21. DTIC AD-A 220597.

7. Solid State Research Report, Lincoln Laboratory, MIT, 1990:1, p. 9. DTIC AD-A 227941.

8. Solid State Research Report, Lincoln Laboratory, MIT, 1990:2, p. 11.

9. K.F. Wall, R.L. Aggarwal, M.D. Sciacca, H.J. Zeiger, R.E. Fahey, and A.J. Strauss, *Opt. Lett.* **14**, 180 (1989).

10. P.W. Smith, *Bell Syst. Tech. J.* **61**, 1975 (1982).

11. A. Lattes, H.A. Haus, F.J. Leonberger, and E.P. Ippen, *IEEE J. Quantum Electron.* **QE-19,** 1718 (1983).

12. H.Q. Le, W.D. Goodhue, and K. Rauschenbach, to be published in *Opt. Lett.*

13. H.Q. Le, D.E. Bossi, K.B. Nichols, and W.D. Goodhue, *Appl. Phys. Lett.* **56**, 1008 (1990).

14. C. Lin, W.A. Reed, A.D. Pearson, and H.-T. Shang, *Opt. Lett.* **6**, 493 (1981).

3. MATERIALS RESEARCH

3.1 AlInGaAs/AlGaAs STRAINED-LAYER SINGLE-QUANTUM-WELL DIODE LASERS

Semiconductor diode lasers incorporating a strained $In_xGa_{1-x}As$ quantum-well active layer and $Al_yGa_{1-y}As$ confining layers grown on a GaAs substrate offer an attractive alternative to lasers of similar structure but with a lattice-matched, unstrained GaAs or AlGaAs active layer. Incorporation of In makes it possible to extend the laser emission wavelength to ~1.1 μm [1], compared with a long-wavelength limit of ~ 0.9 μm for GaAs/AlGaAs lasers. In addition, the strained-layer lasers can have lower values of threshold current density J_{th} [2], and improved reliability is observed [3] for devices with active layers containing sufficient In. One proposed explanation for the improvement in reliability is that the propagation of defects in the active layer is retarded because the In atom is larger than the Ga, Al, and As atoms, which are almost the same size. If this explanation is correct, it might be possible to achieve greater reliability for lasers emitting at wavelengths below 0.9 μm by the use of strained $Al_yIn_xGa_{1-x-y}As$ active layers, in which the Ga in $In_xGa_{1-x}As$ is partially replaced by Al to increase the electron transition energy. As the first step in investigating this possibility, we have fabricated graded-index separate-confinement heterostructure single-quantum-well (GRIN-SCH SQW) $Al_yIn_xGa_{1-x-y}As$/AlGaAs diode lasers with $0.12 \leq x \leq 0.14$ and five values of y between 0.05 and 0.17. As expected, with increasing Al content the emission wavelength decreases from 890 to 785 nm. With one exception, J_{th} is less than 200 A/cm^2, while the differential quantum efficiency η_d ranges from 71 to 88 percent. These devices are the first reported AlInGaAs/AlGaAs diode lasers, although lattice-matched AlInGaAs/InP lasers with emission wavelengths between 1.5 and 1.7 μm have been fabricated on InP substrates [4],[5].

The AlInGaAs/AlGaAs laser structures were grown by organometallic vapor phase epitaxy (OMVPE) in a vertical rotating-disk reactor operated at low pressure [6]. The substrates were Si-doped n^+-GaAs (100) wafers, tilted 2° toward the nearest (110) plane, with etch pit densities of less than 2000 cm^{-2}. The source materials were trimethylgallium, trimethylaluminum, trimethylindium, and 100 percent arsine. Hydrogen selenide (500 ppm in H_2) and dimethylzinc (3000 ppm in H_2) were used as the n- and p-type dopants, respectively. The structure consists of the following layers: 20-nm-thick n-GaAs buffer layer, 0.1-μm-thick graded n-$Al_yGa_{1-y}As$ layer (y linearly graded from 0.1 to 0.7), 1.1-μm-thick n-$Al_{0.7}Ga_{0.3}As$ cladding layer, 0.15-μm-thick undoped $Al_yGa_{1-y}As$ confining layer (y linearly graded from 0.7 to 0.3), 10-nm-thick $Al_yIn_xGa_{1-x-y}As$ active layer, 0.15-μm-thick undoped $Al_yGa_{1-y}As$ confining layer (y linearly graded from 0.3 to 0.7), 1.1-μm-thick p-$Al_{0.7}Ga_{0.3}As$ cladding layer, 0.1-μm-thick graded p-$Al_yGa_{1-y}As$ layer (y linearly graded from 0.7 to 0.1), and 0.1-μm-thick p^+-GaAs contact layer. The n- and p-type doping levels in the cladding layers were varied from 10^{18} down to 10^{17} cm^{-3} toward the GRIN layers to reduce the optical loss resulting from free-carrier absorption.

The substrate temperatures used for OMVPE growth were selected on the basis of surface morphology and photoluminescence studies on test layers. Since epilayers containing In are unstable at the high temperature used for AlGaAs growth, the following sequence was followed in growing the laser structure. The GaAs buffer layer and lower AlGaAs cladding layer were grown at 800°C. The temperature was then lowered to 700°C over a period of several minutes, during which the lower GRIN layer was

grown. The AlInGaAs active layer was grown at 700°C, the temperature was raised to 800°C while the upper GRIN layer was being grown, and the upper AlGaAs cladding layer was grown at 800°C. Finally, the p^+-GaAs cap layer ($p = 6 \times 10^{19}$ cm^{-3}) was grown at 625°C to enhance Zn incorporation [7]. Growth rates were typically 30 nm/min for the active, GRIN, and cap layers and 65 nm/min for the other layers.

To fabricate broad-stripe lasers, 100- or 200-μm-wide Ti/Au stripes on 400-μm centers were defined on the GaAs cap layer by means of evaporation and photolithographic liftoff. Mesas were formed by wet chemical etching between the stripes to a depth of ~ 1 μm, slightly above the active layer. The wafer was mechanically thinned from the substrate side to 100 μm, and contact to the substrate was made by alloying Ge/Au/Ni/Au at 390°C. For stripe widths of 100 and 200 μm, the wafer was cleaved into bars 500 and 700 μm long, respectively. The lasers were probe tested using 200-ns pulses at 1 kHz. Single-ended optical output power was measured with a calibrated Si photodiode detector.

Figure 3-1 shows the curves of light output versus current for four lasers with cavity length of 700 μm that were fabricated from a wafer with an active layer composition of $y = 0.17$, $x = 0.12$. The values of J_{th} range from 193 to 200 A/cm^2, and η_d varies from 66 to 73 percent. For one such laser, the emission spectrum measured at 3.7 times threshold is shown in Figure 3-2. The peak wavelength is 785 nm. Table 3-1 summarizes the performance of lasers fabricated from the five $Al_yIn_xGa_{1-x-y}As$/AlGaAs wafers grown to date, which have active layer compositions with $0.12 \leq x \leq 0.14$ and with y decreasing from 0.17 to 0.05. As previously stated, with decreasing Al content the emission wavelength increases from 785 to 890 nm and η_d ranges from 71 to 88 percent. Except for wafer 847, for which J_{th}

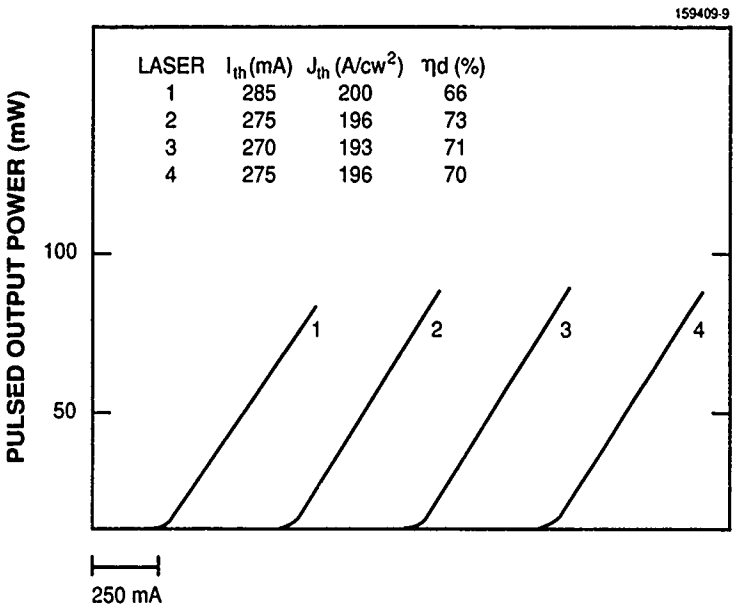

Figure 3-1. Light output versus current for pulsed room-temperature operation of $Al_{0.17}In_{0.12}Ga_{0.71}As$/AlGaAs strained-layer single-quantum-well diode lasers 200 μm wide with a cavity length of 700 μm.

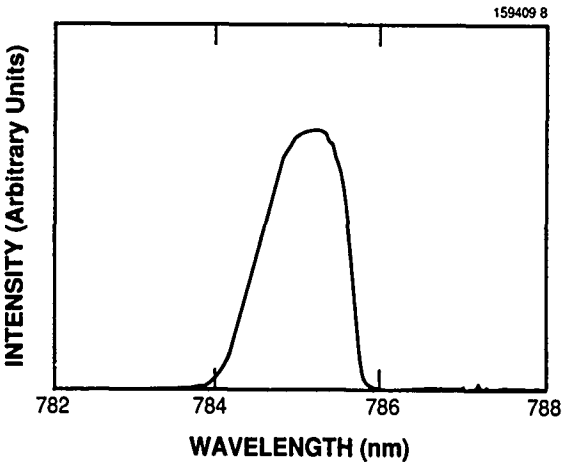

Figure 3-2. Emission spectra for diode laser 3 of Figure 3-1 under pulsed room-temperature operation at 3.7 times threshold.

TABLE 3-1

Characteristics of $Al_yIn_xGa_{1-x-y}As$/AlGaAs Diode Lasers

Wafer	y	x	Cavity Length (μm)	Wavelength (nm)	J_{th} (A/cm^2)	η_d (percent)
809	0.17	0.12	700	785	193	73
847	0.15	0.12	700	815	271	71
848	0.13	0.12	700	827	196	74
849	0.09	0.13	500	850	192	86
851	0.05	0.14	500	890	164	88

appears to be anomalously high, J_{th} ranges from 164 to 196 A/cm^2. For our GRIN-SCH SQW $Al_{0.07}Ga_{0.93}As$/AlGaAs lasers emitting at 808 nm, the lowest J_{th} is 169 A/cm^2 and the highest η_d is 85 percent [6], while for our $In_{0.15}Ga_{0.85}As$/AlGaAs lasers emitting at 950 nm, J_{th} = 120 A/cm^2 and η_d = 79 percent [7]. Thus, the devices with an AlInGaAs active layer are comparable in initial performance with those having either AlGaAs or InGaAs active layers. An investigation of the reliability of the AlInGaAs/AlGaAs lasers will therefore be of great interest.

C.A. Wang H.K. Choi
J.N. Walpole L.J. Missaggia

3.2 IrSi-Si SCHOTTKY-BARRIER INFRARED DETECTORS WITH WAVELENGTH RESPONSE BEYOND 12 μm

Since the use of silicide-Si Schottky-barrier diodes for infrared detection was first proposed in 1973 [8], substantial progress has been made in increasing detector responsivity and extending detector cutoff wavelength. State-of-the-art Schottky-barrier imager arrays [9] employ PtSi detectors, which have a cutoff wavelength of about 6 μm, for imaging in the 3- to 5-μm wavelength spectral band. Because IrSi-Si Schottky diodes [10] have lower barrier heights than PtSi-Si diodes, IrSi detectors have the potential for extending the response of Schottky-barrier sensors into the long-wavelength infrared spectral band from 8 to 14 μm. In an ongoing effort to develop an IrSi-based technology for this band, we have previously fabricated IrSi detectors with cutoff wavelengths out to 10 μm [11] and demonstrated the operation of 128 × 128-element focal plane arrays integrating IrSi detectors with surface-channel charge-coupled device readout circuitry [12].

Silicide-Si Schottky diodes are formed by depositing a noble-metal film on a p-Si substrate, and then annealing to convert the metal to the corresponding silicide by reaction with the substrate. To first order, the barrier height of an intimate silicide-Si Schottky contact is determined by the intrinsic properties of the silicide-Si interface [13]. However, the height also depends on the substrate doping profile [14]. Doping the p-Si surface with acceptor impurities can decrease the barrier height because of image-force barrier lowering and field-assisted tunneling. In order to extend the cutoff wavelength of IrSi detectors, we have used low-energy boron ion implantation to form a shallow p^+ layer at the Si surface before IrSi formation. By means of this technique, the barrier height of IrSi detectors has been reduced by ~ 0.02 eV, thereby extending the detector cutoff wavelength to 12.4 μm, the longest so far reported for silicide Schottky-barrier detectors.

For successful application of the barrier-lowering technique, the dopant concentration in the shallow p^+-Si layer must be high enough to produce appreciable lowering. In addition, in order to preserve the rectifying characteristic of the Schottky-barrier contact, this layer must be thin enough to be fully depleted at zero bias, so that the space-charge region extends into the lightly doped substrate region. For IrSi-Si contacts, with an intrinsic barrier height of only ~ 0.12 eV, very shallow p^+ doping is required to prevent excess tunneling current, which degrades detector dark-current characteristics and responsivity. For a p^+ layer with uniform dopant concentration of 10^{18} cm^{-3}, the thickness should not exceed 6 nm.

The structure of the present IrSi Schottky-barrier detectors is similar to the structure reported previously [15]. Briefly, it incorporates an IrSi-Si Schottky-barrier contact on a (100) p-Si substrate doped to ~ 10^{15} cm^{-3}, an n-type guard ring to suppress edge leakage, and a heavily doped p^+ region on the front side of the substrate for ohmic contact. Before IrSi formation, the Si surface was implanted with 1-keV boron ions to a dose of 1×10^{12} cm^{-2} through a thermal SiO_2 layer ~ 3 nm thick. Since the projected range for 1-keV boron ions in SiO_2 is ~ 3 nm, the peak of the boron distribution is near the SiO_2-Si interface. The implanted boron was activated by furnace annealing at 700°C for 1 h. The SiO_2 layer prevents outdiffusion of boron during annealing, and the diffusion distance of boron during annealing is estimated to be less than 1 nm, so that the peak boron concentration is ~ 1×10^{18} cm^{-3}. After annealing, the SiO_2 was etched away, and an IrSi film ~ 4 nm thick was formed by electron beam deposition and lamp annealing of a 2-nm-thick Ir film in a high-vacuum system using the procedure reported previously [11].

Figures 3-3(a) and 3-3(b), respectively, show the forward and reverse current-voltage characteristics measured in the dark at five temperatures from 40 to 80 K for a typical IrSi detector with a shallow p^+ layer. At the three lower temperatures the diode ideality factor n is slightly greater than unity, indicating predominantly thermionic emission current. The reverse characteristics show a gradual increase of current I_R with bias voltage V_R at high temperatures and a much more rapid increase for $V_R > \sim 1$ V at low temperatures. For an ideal Schottky-barrier diode, I_R is proportional to $T^2 \exp[-q(\phi_B - \Delta\phi_B)/kT]$, where ϕ_B is the zero-bias electrical barrier height and $\Delta\phi_B$ ($\propto V_R^{1/4}$) is the barrier lowering due to the image-force effect [16]. At low temperatures, the increase of I_R with V_R is therefore expected to be more pronounced, as observed.

The electrical barrier height $\phi \equiv \phi_B - \Delta\phi_B$ of the detector of Figure 3-3 has been determined [16] from the slope of a plot of J/T^2 versus $1/T$, where J is reverse current density. This plot, based on the measurements at $V_R = 1$ V, is shown in Figure 3-4, together with a similar plot for a device without the p^+ layer. The values of ϕ obtained from the linear portions of these plots are 0.094 and 0.115 eV, respectively.

The photoresponse of the IrSi detectors of Figure 3-4 has been measured at 40 K for $V_R = 1$ V. Figure 3-5 shows plots of responsivity R as a function of wavelength from 1 to 14 μm. Both sets of data can be fitted by the modified Fowler equation [17], $R = C_1(1 - \lambda\psi/1.24)^2$, where C_1 is the emission coefficient (in eV^{-1}), ψ is the optical barrier height (in eV), and λ is the wavelength (in μm). For the detectors with and without a p^+ layer, the C_1 values obtained by curve fitting are 0.045 and 0.043 eV^{-1}, respectively. The values of ψ are 0.100 and 0.117 eV, respectively, and the corresponding values of the cutoff wavelength, $\lambda_c \equiv 1.24/\psi$, are 12.4 and 10.6 μm. The values of ψ obtained by spectral response measurements are somewhat higher than the corresponding values of ϕ, because photogenerated hot carriers lose some of their energy by phonon collisions prior to emission over the Schottky barrier [18].

Because of image-force lowering, the barrier height of silicide-Si Schottky-barrier detectors decreases as V_R is increased. For IrSi detectors with a p^+ layer, with increasing bias the value of R increases initially but decreases for voltages exceeding 5 V. The reduction in R takes place because the increase in hole-electron generation in the Si depletion layer increases the density of electrons in the IrSi film that

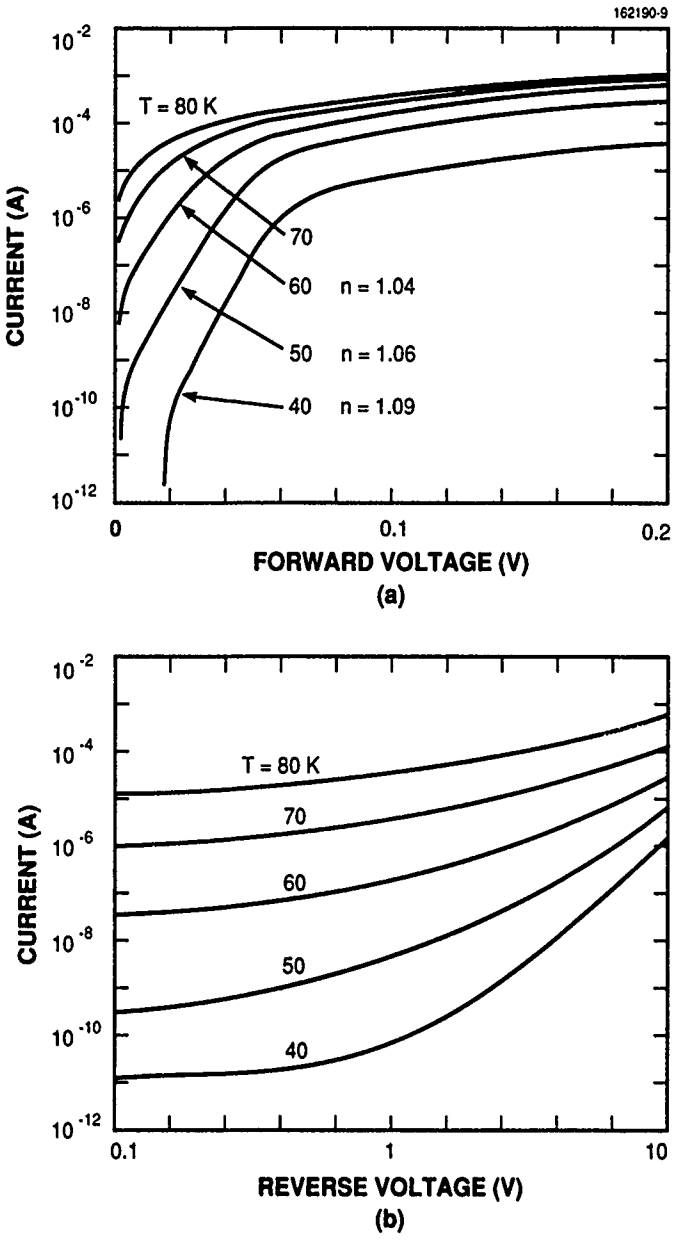

Figure 3-3. (a) Forward and (b) reverse current-voltage characteristics at five temperatures for an IrSi Schottky-barrier detector with a shallow p^+ layer at the surface of the Si substrate.

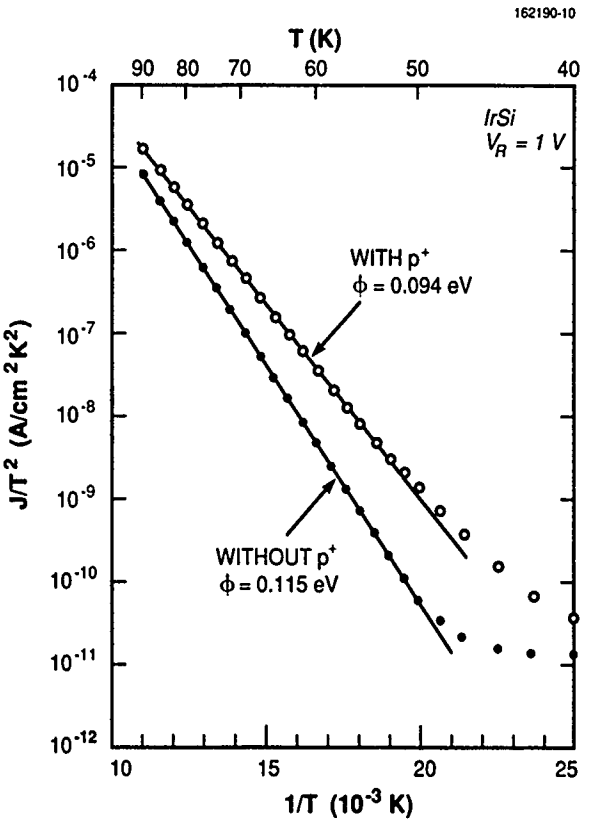

Figure 3-4. Plots of J/T^2 versus reciprocal absolute temperature 1/T for the IrSi detector of Figure 3-3 and for a conventional IrSi detector without a p^+ layer, where J is the dark current density at a reverse-bias voltage V_R of 1 V.

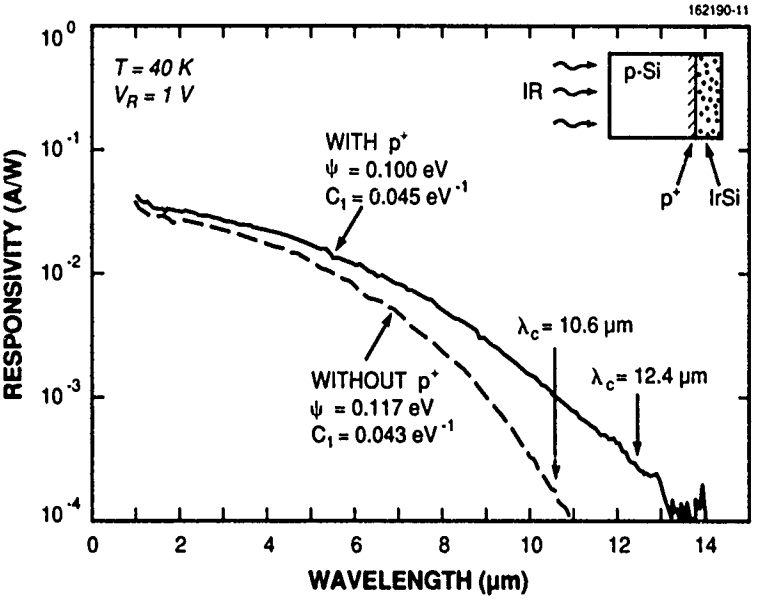

Figure 3-5. Responsivity versus wavelength for the detectors of Figure 3-4.

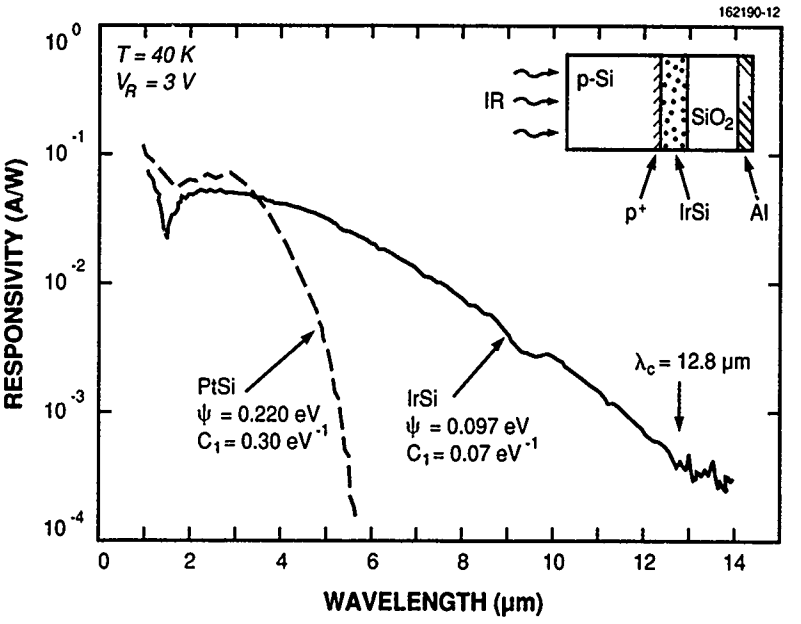

Figure 3-6. Responsivity versus wavelength for an IrSi detector with a shallow p^+ layer and for a high-performance PtSi detector, both with an optical cavity for enhanced optical absorption.

are sufficiently energetic for effective scattering of the photogenerated holes, which reduces the energy of the photocarriers and therefore the probability of their emission over the Schottky barrier. At 5-V bias, $\psi = 0.094$ eV, corresponding to $\lambda_c = 13.2\ \mu$m, has been measured for IrSi detectors with a p^+ layer.

The responsivity of IrSi detectors with a p^+ layer has been increased by using an optical cavity [10], consisting of a 1-μm-thick SiO_2 layer formed by chemical vapor deposition and an evaporated Al film, to enhance the absorption of infrared photons in the IrSi film. The peak wavelength for such a cavity is estimated to be ~ 8 μm. In Figure 3-6, R at 40 K is plotted versus λ for a detector with such a cavity and for a high-performance PtSi detector, also with an optical cavity. The IrSi detector has higher values of R than the PtSi detector for wavelengths beyond 3.5 μm.

B-Y. Tsaur
C.K. Chen
B.A. Nechay

REFERENCES

1. K.J. Beernink, P.K. York, and J.J. Coleman, *Appl. Phys. Lett.* **55**, 2585 (1989).
2. H.K. Choi and C.A. Wang, *Appl. Phys. Lett.* **57**, 321 (1990).
3. D.P. Bour, D.B. Gilbert, K.B. Fabian, J.P. Bednarz, and M. Ettenberg, *IEEE Photon. Technol. Lett.* **2**, 173 (1990).
4. W.T. Tsang and N.A. Olsson, *Appl. Phys. Lett.* **42**, 922 (1983).
5. R. Gessner, M. Druminski, and M. Beschorner, *Electron. Lett.* **25**, 516 (1989).
6. C.A. Wang, H.K. Choi, and M.K. Connors. *J. Electron. Mater.* **18**, 695 (1989).
7. C.A. Wang and H.K. Choi, to be published in *IEEE J. Quantum Electron.*
8. F.D. Shepherd and A.C. Yang, *Int. Electron Devices Mtg. Tech. Dig.* (IEEE, New York, 1973), p. 310.
9. W.F. Kosonocky, F.V. Shallcross, T.S. Villani, and J.V. Groppe, *IEEE Trans. Electron Devices* **ED-32**, 1564 (1985).
10. P.W. Pellegrini, A. Golubovic, C.E. Ludington, and M.M. Weeks, *Int. Electron Devices Mtg. Tech. Dig.* (IEEE, New York, 1982), p. 157.
11. B-Y. Tsaur, M.M. Weeks, R. Trubiano, and P.W. Pellegrini, *IEEE Electron Device Lett.* **9**, 650 (1988).
12. B-Y. Tsaur, M.J. McNutt, R.A. Bredthauer, and R.B. Mattson, *IEEE Electron Device Lett.* **10**, 361 (1989).
13. See, for example, P.E. Schmid, *Helv. Phys. Acta* **58**, 371 (1985).
14. J.M. Shannon, *Solid-State Electron.* **19**, 537 (1976).
15. B-Y. Tsaur, M.M. Weeks, and P.W. Pellegrini, *IEEE Electron Device Lett.* **9**, 100 (1988).
16. S.M. Sze, *Physics of Semiconductor Devices*, 2nd ed. (Wiley, New York, 1981), Chap. 5.
17. V.L. Dalal, *J. Appl. Phys.* **42**, 2274 (1971).
18. J.M. Mooney and J. Silverman, *IEEE Trans. Electron Devices* **ED-32**, 33 (1985).

4. SUBMICROMETER TECHNOLOGY

4.1 PLASMA-DEPOSITED ORGANOSILICON THIN FILMS AS DRY RESISTS FOR DEEP-UV LITHOGRAPHY

Plasma-enhanced chemical vapor deposition (PECVD) of ultrathin organosilicon films and their use as deep-UV photoresists are reported. Because of their photoreactivity at short wavelengths and their etch resistance in O_2 plasma, such films may be an effective alternative to thicker, all-organic photoresists.

Organosilicon thin films are deposited from liquid precursors in a conventional 13.56-MHz, RF-powered parallel-plate reactor. The precursors include: (i) hexamethyldisilazane (HMDS), $(CH_3)_3$ Si-NH-Si$(CH_3)_3$, (ii) hexamethyldisilane (HM_2S), $(CH_3)_3$Si-Si$(CH_3)_3$, (iii) tetramethylsilane (TMS), $(CH_3)_4$ Si, and (iv) trimethylsilyldimethylamine (TMSDMA), $(CH_3)_3$Si-N-$(CH_3)_2$. Gases are introduced through a shower head in the top electrode. Both the top and bottom electrode are water cooled and can be independently powered. Films are deposited on a temperature-controlled bottom electrode at rates from 1 to 25 nm/min at relatively high pressures (300 to 950 mTorr) and low power densities (0.06 to 0.55 W/cm^2). They all are highly photosensitive at 193 nm. Exposure at low fluences (< 5 mJ/cm^2) results in photooxidation of the films, as evidenced by changes in their physical and chemical properties.

Figure 4-1 shows the effect of 193-nm radiation on the refractive index at 633 nm and on the oxygen-to-silicon (O/Si) atomic concentration ratio of a 50-nm-thick film deposited from HMDS. With increasing dose, the index of refraction decreases from its initial value of 1.495 to 1.440 at 3 J/cm^2. These

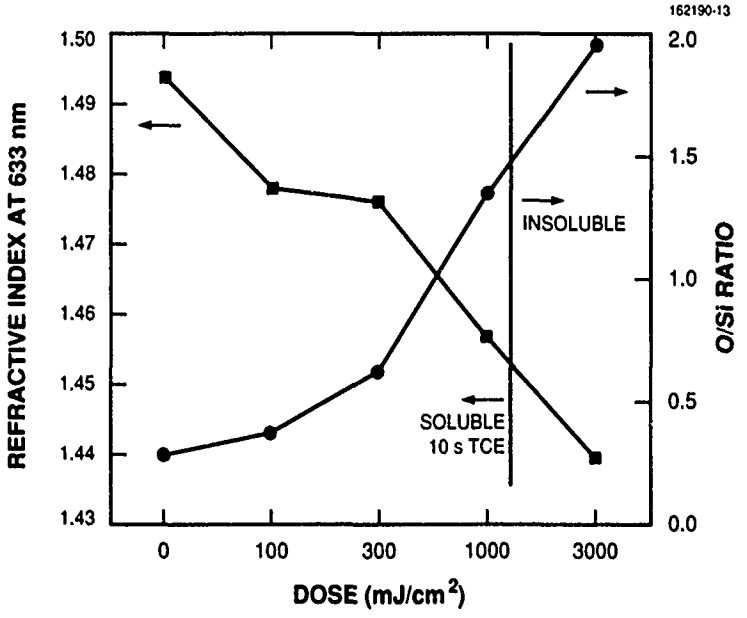

Figure 4-1. Effect of 193-nm exposure of an organosilicon thin film on index of refraction at 633 nm, stoichiometry (ratio of oxygen-to-silicon concentration), and solubility in trichloroethane (TCE). The 50-nm-thick film was deposited from HMDS in an RF plasma, and the exposure was at a fluence of 3 mJ/cm^2 per pulse.

figures should be compared to the index of 1.457 of synthetic fused silica. In parallel with a reduction in the index of refraction, the oxygen content of the film, as measured with Auger electron spectroscopy (AES), increases with dose. Prior to exposure the film contains some oxygen, apparently as a result of reactions between chemically reactive radicals in the film and oxygen molecules in air [1]. The O/Si ratio is, however, quite low, < 0.3, and is strongly dependent on the precursor gas and deposition conditions used. Exposure in air at 193 nm clearly induces oxidation, and the O/Si ratio approaches that of SiO_2 at 3 J/cm^2. Furthermore, x-ray photoelectron spectroscopy (XPS) of the Si 2p peak indicates that the chemical bonding of the silicon atoms in the film changes upon exposure. At low doses, the Si 2p binding energy is 101.2 eV, characteristic of a siloxane, while for doses exceeding 1 J/cm^2, it approaches 103.5 eV, the value for SiO_2. Figure 4-1 also shows the strong effect that photooxidation of the organosilicon film has on its solubility in trichloroethane (TCE). As deposited, the film is completely soluble in TCE within a few seconds. It remains so up to a dose of ~ 1.2 J/cm^2 (corresponding to an O/Si ratio of ~ 1.5). At higher doses the film abruptly becomes insoluble in TCE. The abruptness of the transition is the main reason that the film is suitable as a high-contrast, wet-developable photoresist in submicrometer lithography.

The effects of 193-nm radiation on the chemical structure of organosilicon thin films are further clarified by Fourier-transform infrared (FTIR) spectroscopy. Unexposed films exhibit some Si-O bonding, in agreement with the AES and XPS results discussed above. Upon irradiation the Si-O absorption peak at ~ 1050 cm^{-1} increases by more than a factor of 2 with respect to the Si-$(CH_3)_n$ peak at ~ 800 cm^{-1} and the aliphatic C-H absorption peaks (2800 to 3000 cm^{-1}). These results indicate that 193-nm irradiation in air induces an uptake of oxygen, formation of Si-O bonds, and probably volatilization of aliphatic fragments.

The UV-visible absorption spectra also show changes related to the photooxidation process of organosilicon thin films. Figure 4-2 illustrates the effect of 193-nm exposure in air on the UV absorption spectrum of a 50-nm-thick film deposited from HMDS. The unexposed film is transparent in the visible, and has a strong absorption below ~ 230 nm. Note the decrease in this absorption as a function of the number of pulses. After 1000 pulses (total dose of ~ 1.2 J/cm^2), the absorption at 193 nm has decreased to the very low levels characteristic of stoichiometric SiO_2 (the residual absorbance of 0.08 is attributed to Fresnel reflection rather than to absorption).

By the use of 193-nm projection lithography, submicrometer patterns are imaged and transferred through an underlying carbon layer. Negative-tone imaging is achieved by patterned photooxidation of the PECVD organosilicon films at fluences (< 5 mJ/cm^2) well below the self-development threshold. Organic solvents such as TCE and toluene are used to dissolve the unexposed regions of the films. Following development, O_2 reactive ion etching (RIE) is used to transfer the patterns into the underlying organic planarizing layer. The organosilicon films are highly resistant to O_2 RIE and thus serve in the dual role of photoresist and etch mask. Figure 4-3 shows the resultant patterns when imaging is performed in projection on a 100-nm-thick TMS film deposited at 950 mTorr, and exposed at a fluence of 1 mJ/cm^2 per pulse, and a total dose of 360 mJ/cm^2. Lines and spaces with a nominal resolution of 0.6, 0.5, and 0.4 μm are well defined, and aspect ratios higher than 2:1 are obtained. The surface roughening in the unexposed regions is still under study, but may be caused by inorganic residue or by incomplete etching of the planarizing layer.

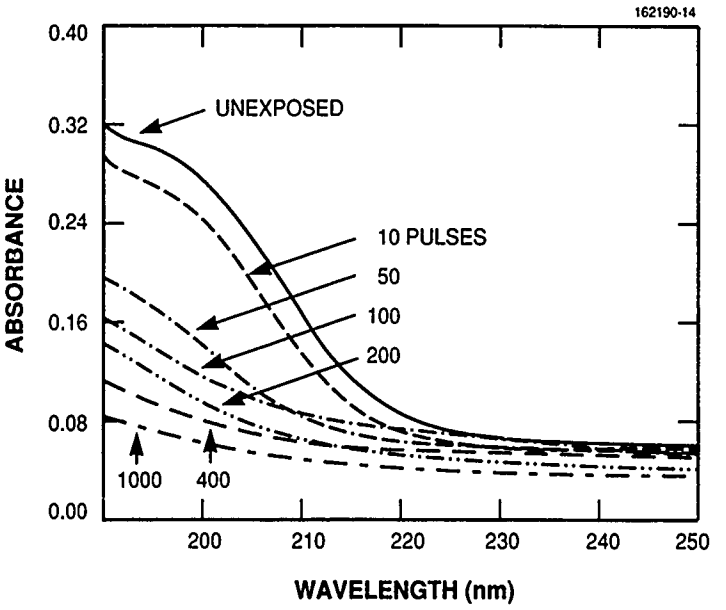

Figure 4-2. Effect of 193-nm exposure on the UV absorption of a 50-nm-thick film deposited from HMDS. The absorption curves are labeled by the number of pulses used in the exposure. The fluence was ~ 1.2 mJ/cm^2 per pulse.

Organosilicon films that are photooxidized are also successfully dry developed using HBr and Cl_2 RIE. This process is illustrated in Figure 4-4 for a 135-nm-thick film deposited from TMS at 300 mTorr. This sample is patterned in projection at a fluence of 1 mJ/cm^2 per pulse and a total dose of 40 mJ/cm^2. The films are developed using HBr RIE at 10 mTorr and 100-V self-bias, and the patterns are then transferred using O_2 RIE at 150-V self-bias. The resolution of these features is better than 0.4 μm, and the aspect ratio is greater than 2:1. Note that the dry-developed patterns are obtained at doses that are almost an order of magnitude lower than those used for wet development. Part of the increased sensitivity may be attributed to the difference between the requirement to modify only the surface layer of the film in dry development and the need to oxidize the full thickness of the film in wet development.

All-dry positive-tone imaging is also accomplished at 193 nm. Exposure is performed at fluences of ~ 15 mJ/cm^2 per pulse. At these relatively high fluences the dominant photoprocess is volatilization of the organosilicon thin film, and self-developed submicrometer patterns are obtained. Figure 4-5 shows such patterns transferred through a plasma-deposited planarizing layer. The bilayer resist is formed by planarizing 1-μm-deep oxide steps with a plasma-deposited, hydrogenated amorphous carbon (*a*-C:H) layer [2], followed by the deposition of a 50-nm-thick organosilicon imaging layer. The imaging layer is deposited from HMDS at a pressure of 950 mTorr and an RF power density of 0.1 W/cm^2, and it is then patterned with ten pulses at 16 mJ/cm^2 per pulse. After exposure, the pattern is transferred through the *a*-C:H planarizing layer by O_2 RIE. Notably, the final patterns show no residue, unlike the negative-tone low-fluence samples in Figures 4-3 and 4-4.

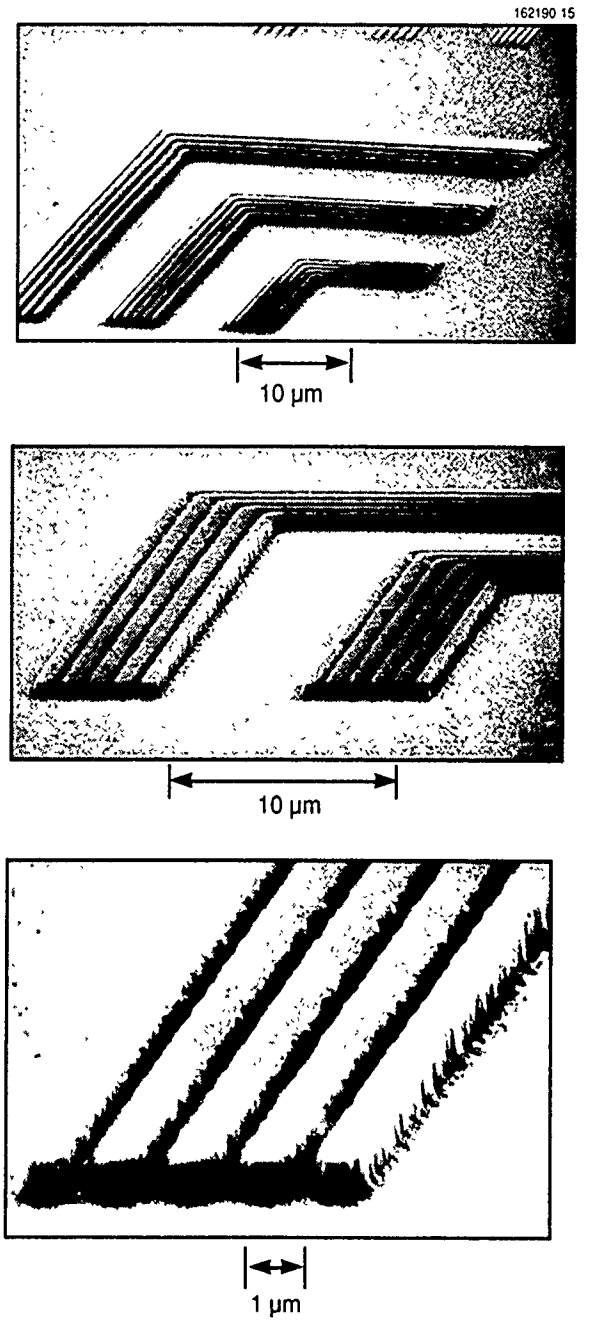

Figure 4-3. Scanning electron micrographs (SEMs) of submicrometer patterns obtained with an organosilicon layer exposed in projection at 193 nm. Nominally 0.6-, 0.5-, and 0.4-µm equal lines and spaces are seen, with increasing magnification from the upper to lower frame. The 100-nm-thick imaging layer was deposited from TMS on a 1-µm-thick organic planarizing layer. The patterns were exposed at a fluence of 1 mJ/cm^2 per pulse and a dose of 360 mJ/cm^2. This was followed by wet development for 5 s in toluene and by O_2 RIE for pattern transfer.

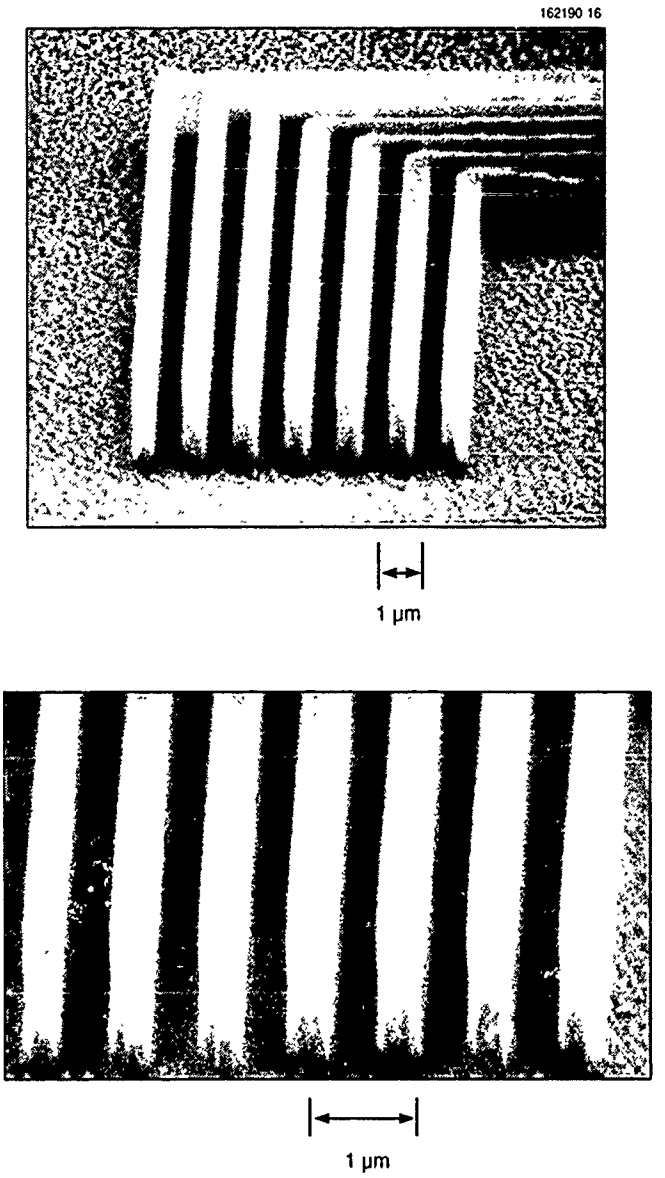

Figure 4-4. SEMs at two magnifications of nominally 0.4-µm lines and spaces patterned in a bilayer that consisted of a 135-nm-thick imaging layer deposited from 1MS on a 1-µm-thick organic planarizing layer. The projection exposure at 193 nm was performed at a fluence of 1 mJ/cm^2 per pulse and a dose of 40 mJ/cm^2. The films were then dry developed using HBr RIE, and the patterns were transferred using O_2 RIE.

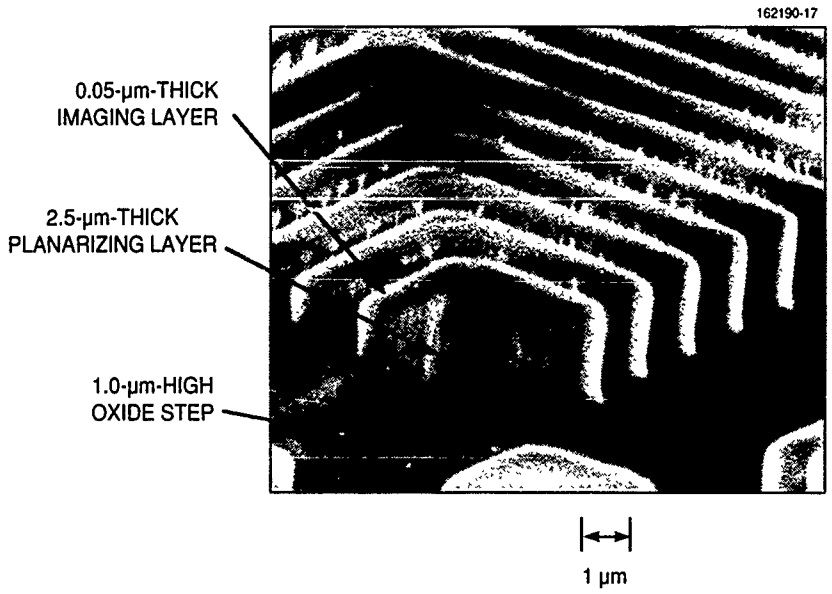

Figure 4-5. SEM of an all-dry bilayer resist system patterned in projection at 193 nm. The planarizing layer was 2.5-μm-thick a-C:H PECVD film deposited over 1.0-μm-thick oxide steps, and the 50-nm-thick imaging layer w deposited from HMDS. Self-developed patterning was performed in projection at 193 nm, using ten pulses at fluence of 16 mJ/cm^2 per pulse. Pattern transfer was performed using O_2 RIE.

In summary, PECVD organosilicon thin films are used as imaging layers in a bilayer resist sche for deep-UV lithography. Photooxidation induced by 193-nm radiation is exploited with either wet or d development to yield negative-tone patterns. Films deposited from TMS are patterned in projection at a dose of 40 mJ/cm^2 and dry developed using HBr RIE. Wet development in TCE or toluene is also demonstrated at higher doses. Patterns with resolution better than 0.4 μm are transferred through a planarizing organic layer to yield features with a high aspect ratio. At higher fluences, above ~ 15 mJ/cm^2, high-resolution self-development is also achieved.

M.W. Horn
S.W. Pang
M. Rothschild

4.2 DIFFRACTIVE OPTICAL ELEMENTS AS ILLUMINATOR COMPONENTS IN 193-nm EXCIMER LASER LITHOGRAPHY SYSTEMS

Most optical glasses are strongly absorbing at wavelengths in the deep UV (< 300 nm). As a result, refractive elements can be made from only a few materials, of which fused silica is by far the most practical. This reliance on a single refractive material makes the achromatization of lenses, which is typically taken for granted with visible light, difficult. One solution is to use all-reflecting optics, which are inherently achromatic, allowing good imagery with both visible and UV light. Our 193-nm-wavelength small-field lithographic exposure system, which we use to pattern submicrometer patterns in

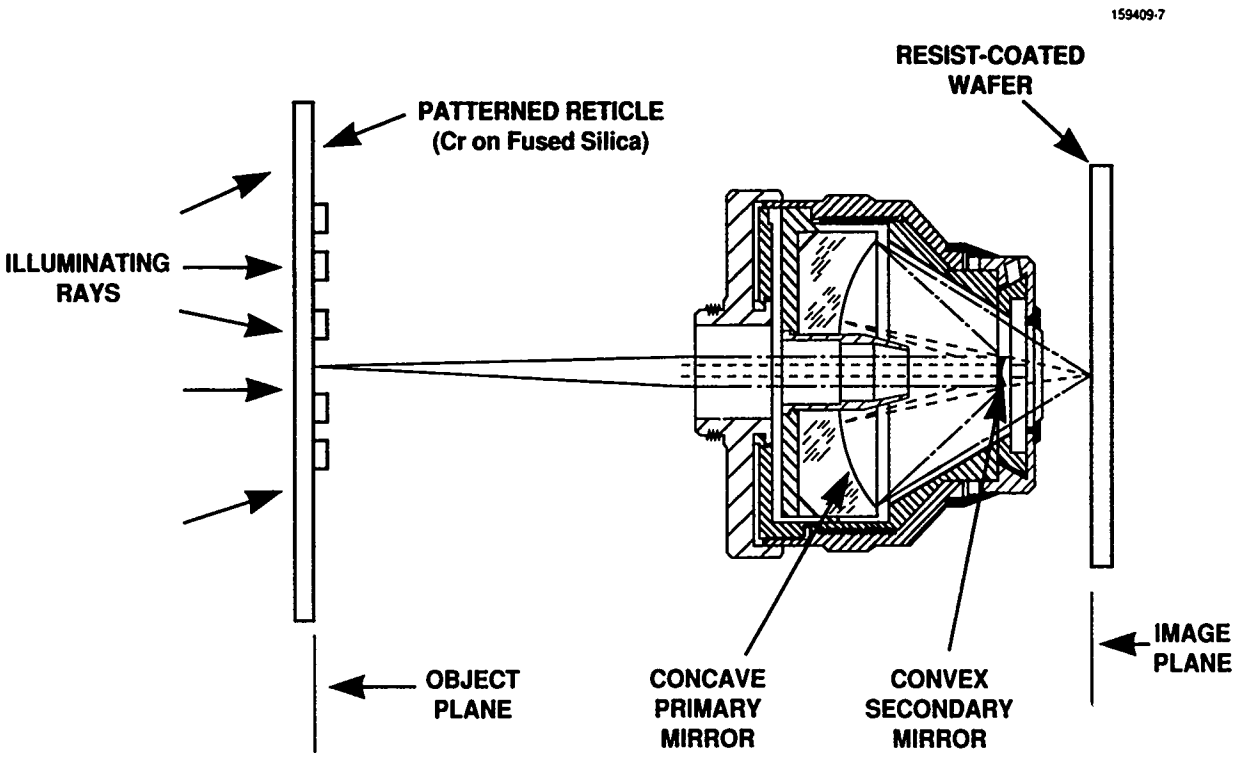

Figure 4-6. Schematic diagram of a Schwarzschild reflecting objective showing the object (reticle) and image (wafer) planes. Fly's-eye lens diffusers and condenser lenses are located to the left of (behind) the reticle.

various experimental resists, employs an all-reflecting microscope objective based on the Schwarzschild design. Schwarzschild objectives, whose general form is illustrated schematically in Figure 4-6, have a partial obscuration of the pupil caused by the small convex secondary mirror lying between the image plane and the concave primary. This obscuration, which results in an annular pupil, makes the illumination requirements for the object plane (reticle) different and more critical than for an unobscured optical system. Here, we describe a technique for fabricating arrays of lenslets, or arbitrary scatterers, lithographically. These lenslet arrays allow the efficient transformation of a relatively spatially coherent beam from a 193-nm ArF excimer laser into a beam whose spatial extent and divergence (etendue) closely match the entrance pupil requirements of our Schwarzschild objectives.

The simplest possible illumination scheme that can be used for projection exposure of a reticle pattern onto a wafer is to illuminate the reticle with the raw beam from the excimer laser. Though some very high-resolution exposures have been obtained this way, several defects are apparent in the imagery when a Schwarzschild objective is used. First, only an annular portion of the reticle pattern prints. Second, only grating patterns whose lines are oriented approximately radially with respect to the center of the field are resolved clearly over a wide range of spatial frequencies. Patches of grating with lines oriented tangentially print only at much lower spatial frequencies. The first defect, or annular field,

occurs because the illumination is not focused into the entrance pupil and is relatively collimated. Rays near the field center hit the central obscuration and are blocked, while the outer limit of the annulus is due to rays falling outside the entrance pupil, i.e., vignetting. Focusing the laser beam to illuminate a small region in the entrance pupil eliminates the dead spot in the center of the field and the vignetting, but if the reticle is mostly transparent the concentration of the beam into a small area results in destruction of the optics, since the peak power of the excimer laser is quite large (~ 10 MW). Furthermore, the second problem, a difference in the attainable resolution between orthogonally oriented lines, persists.

A substantially better scheme is to focus the laser output into the center of the entrance pupil and increase the divergence of the laser beam to fill the annular pupil as well as the dead spot in the center of the annulus. In this case, each reticle region is illuminated by rays that pass through every possible point in the annular pupil. This spreads the laser energy over the pupil, reducing the potential for damage to the optics, and results in imagery that is identical for all feature orientations. For a 36× reduction, 0.5-numerical-aperture (NA) reflecting microscope objective, the object (reticle) side NA is 0.014. Thus, to fill the pupil the illuminating light should have a divergence of about 2 NA = 28 mrad. The field size at the reticle is ~ 18 mm in diameter. Unfortunately, the excimer beam is rectangular (~ 24 mm horizontally and ~ 6 mm vertically) and has a low divergence (~ 3 mrad horizontally and ~ 1 mrad vertically). In our system, we typically scan the excimer beam vertically to illuminate a field ~ 25 mm square, thereby increasing the divergence of the beam to 3 mrad in that direction also, but the beam divergence must still be increased significantly in both directions to ~ 28 mrad. The obvious way to achieve this, aside from mechanically rocking the beam which is feasible only if large numbers of pulses are being used for each exposure, is to use a diffuser. However, conventional diffusers made by grinding glass often scatter light through large angles (> 200 mrad) and would overfill the pupil of our projection lens, wasting most of the laser light. Our solution has been to use microlithographic techniques to fabricate diffusers with well-controlled scattering angles and small divergences.

A fly's-eye lens array is one way to implement the diffuser. If an array of small lenses, each with 0.014 NA, is placed in the path of a plane wave, then rays from a large number of lenslets will cross at a point many focal lengths downstream from the array. If the rays contributed from the different lenslets have no fixed phase relationship, then the effect will be to produce spatially incoherent illumination with little intensity modulation and with a divergence controlled by the NA of the lenslets. If, on the other hand, the rays from the lenslets interfere coherently, a strong speckle pattern (100 percent intensity modulation) will appear downstream from the lens array. If the array is periodic as ours is, then a clear periodicity will appear in the speckle pattern, though even an aperiodic pattern will produce speckle with large intensity modulation. In order to ensure the overlap of rays from many lenslets (to uniformly fill the pupil) and to reduce speckle, it is desirable to place the fly's-eye array at a distance L as far behind the reticle as possible. The maximum distance L_{max} is constrained by the finite diameter D of the illuminated area of the reticle and the divergence of the array (NA) as

$$L << L_{max} = \frac{D}{2\,\mathrm{NA}} \,. \tag{4.1}$$

The minimum acceptable distance L_{min} depends on the degree of tolerable speckle, the spatial and temporal coherence of the laser, and the periodicity of the lenslets. If the light source has extremely short temporal coherence, e.g., white light, then the small optical pathlength difference between rays from each lenslet will lead to incoherent summing even with perfectly collimated incident light. In our case, the laser is temporally coherent enough that we must rely on the spatial incoherence of the illuminating light to smear out the speckle pattern. If the laser light consists of uncorrelated plane waves filling a divergence angle θ_ℓ, then each illuminating ray will produce a periodic speckle pattern with period P (the period of the lenslet centers in the array) downstream from the array. The speckle patterns will sum incoherently, i.e., in intensity. If many identical but spatially displaced speckle patterns are spread over the period P and are summed (in intensity), then the intensity at any point, which represents an average over P, will be constant spatially. Thus, if the illuminating rays are distributed uniformly in intensity over the divergence angle θ_ℓ, the speckle is smoothed out at a distance

$$L_{min} = \frac{P}{\theta_\ell} . \tag{4.2}$$

Even if the rays do not uniformly fill the beam divergence angle, the speckle pattern is quite well averaged out so long as L is many times L_{min}, and therefore

$$L >> L_{min} = \frac{P}{\theta_\ell} . \tag{4.3}$$

Given a laser with modest temporal coherence and with a divergence such that a diameter D is illustrated on the reticle, the only variable left to ensure that a value of L exists for which $L_{min} << L << L_{max}$ is the period P of the lens array. If we choose L to be $\sim L_{max}/4$ and $4L_{min}$, which marginally satisfies our criteria, then

$$P \leq \frac{D\theta_\ell}{32\,\mathrm{NA}} . \tag{4.4}$$

For an illuminated area of D = 18 mm, an NA of 0.014 (set by the objective), and a laser divergence of ~ 3 mrad (determined by the laser horizontally and by scanning vertically), we get $P \leq 121\ \mu$m. Thus, our fly's-eye array must consist of lenses covering an area somewhat larger than 18 mm in diameter and on centers less than ~ 120 μm.

We have chosen to fabricate the lenses by patterning zone plates using an electron beam lithography system. Although the features required are not particularly small, with a minimum linewidth $\lambda/(2\,\mathrm{NA})$ that is about 7 μm for our chosen wavelength of 193 nm, the large numbers of circular features to be written and the critical importance of linewidth control favor the electron beam approach. A chromium-on-fused-silica mask plate coated with polymethylmethacrylate (PMMA) is used as the starting material. After electron beam writing and development of the PMMA, the underlying chromium is etched in a wet etchant. Figure 4-7 shows a photograph of part of a zone plate array at this stage of processing. In this case, the overall pattern is a 100 × 100 array of lenslets on 180-μm centers. Arrays with > 100,000 lenslets have been fabricated. The resulting zone plate, which is 50 percent opaque (chromium) and 50 percent transparent, is an array of lenslets, but passes most of its energy undiffracted. To increase the transmis-

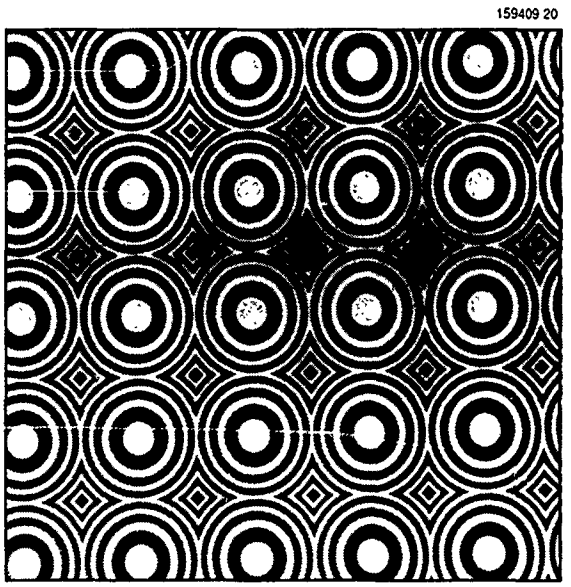

Figure 4-7. Section of a 100 × 100 array of zone plates on 180-μm centers. This photograph shows a chromium (bright) on fused silica (dark) pattern before etching of the fused silica and stripping of the chromium.

sion to 100 percent and eliminate the zero-order beam, we convert the zone plates into phase plates. By using the chromium as a masking material, we etch into the fused silica to a depth of 0.172 μm, calculated using 1.561 as the refractive index at 193 nm, and strip the chromium. This results in a 180° phase shift between the light passing through the etched and unetched regions, with cancellation of the zero order. In general, the etch depth t for cancellation is

$$t = \frac{\lambda}{2(n-1)} , \tag{4.5}$$

where λ is the wavelength in air and n is the refractive index. These phase plate arrays show the expected diffusing properties and substantially improve the imagery obtained from the Schwarzschild objective.

It should be mentioned that the lenslet array described above is not fully optimized for use with an objective with an annular pupil. Some illuminating rays hit the central obscuration. This causes a small decrease in efficiency (the Schwarzschild objectives have ~ 13 percent area obscuration), but more importantly these rays degrade the quality of the imagery since, for the case of a grating, spatial frequency-doubling can occur owing to blockage of the zero-order beam. As has been described in [3], filling an annular portion of the pupil is a superior solution, which the authors achieved by mechanical rotation of the illumination optics. By modifying the design of the "scatterer" in our diffuser array, we can arbitrarily control the intensity distribution across the pupil. Figure 4-8(a) shows a zone plate lenslet, while Figure 4-8(b) shows a modified "lenslet" that scatters less energy on axis since it is missing the lower spatial frequency zones. We have also fabricated linear phase plates (cylindrical lenslets) and crossed linear phase plates.

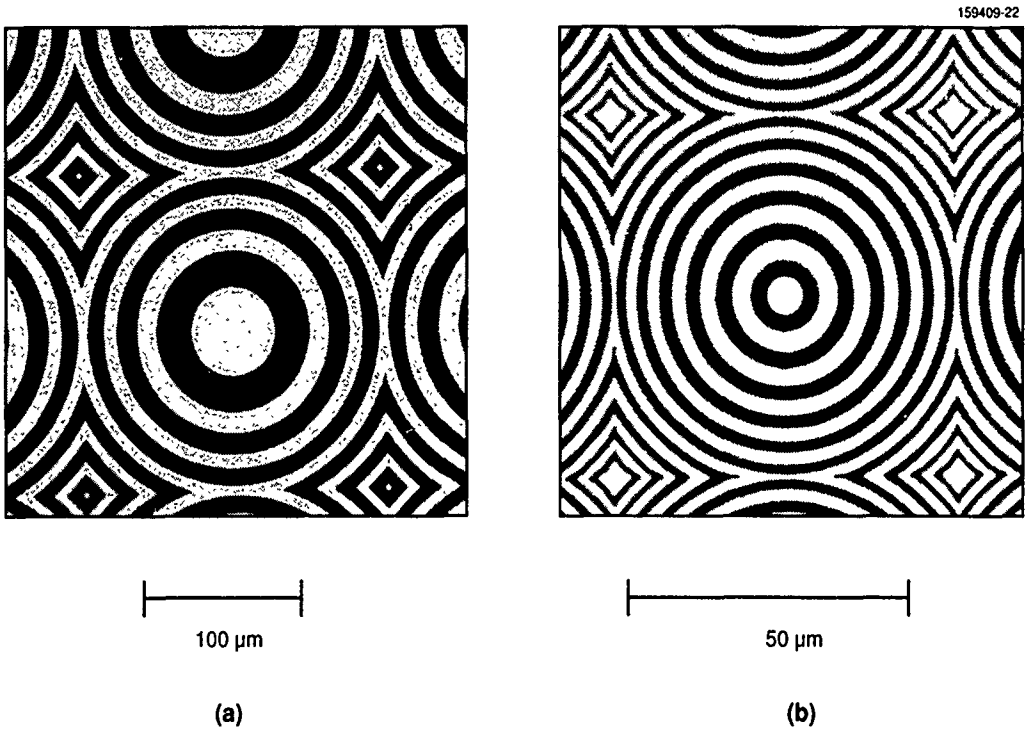

Figure 4-8. (a) Conventional zone plate lenslet and (b) a modified design that creates a hollow cone of illuminating rays.

This work demonstrates a novel use of microlithographic technology for the fabrication of illumination components for projection optical systems. The ability to fabricate beam-transforming components as thin plates using lithographic techniques results in low cost, rapid turnaround for new designs, and good optical transmission characteristics at wavelengths where refractive materials may be absorbing. As such, we expect this to be a useful substitute for systems employing fiber bundles, ground fly's-eye lenses, and light pipes. The undesirable properties of diffractive optics, such as the formation of both real and virtual images as well as higher-order foci, are not significant handicaps in an illumination system.

D.C. Shaver
C.L. Dennis
T.M. Lyszczarz

REFERENCES

1. A similar effect was noted in PECVD films deposited from vinyltrimethylsilane. See M.J. Vasile and G. Smolinsky, *J. Electrochem. Soc.* **119**, 451 (1972).

2. S.W. Pang and M.W. Horn, *IEEE Electron Device Lett.* **11**, 391 (1990); Solid State Research Report, Lincoln Laboratory, MIT, 1990:1, p. 35. DTIC AD-A 227941.

3. S.T. Yang, R.L. Hsieh, Y.H. Lee, R.F. Pease, and G. Owen, *Proc. SPIE* **1264**, 477 (1990).

5. MICROELECTRONICS

5.1 INTEGRATED ELECTRONIC SHUTTER FOR BACK-ILLUMINATED CHARGE-COUPLED DEVICES

A visible-wavelength electronic shutter has been designed and fabricated to reduce smear that occurs during the transfer of an image from a charge-coupled device (CCD) detection area. Smear is an important problem in high-frame-rate applications, such as high-speed photography, target tracking, and real-time adaptive optics, where the image transfer time is comparable to or greater than the stare or integration time. Extinction ratios (ratio of photons detected with shutter open to photons detected with shutter closed) of 50 to 100 have been measured on these shuttered devices. The switching time for the shutter is of the order of a microsecond and is currently limited by the measurement technique.

The electronic shutter has been integrated into a back-illuminated buried-channel CCD [1] by inclusion in an existing process of two extra masking and implantation steps. Figure 5-1(a) shows a top-plan view of the frame-transfer CCD including the electronic shutter, and Figure 5-1(b) illustrates the top-plan and cross-sectional views of a single back-illuminated pixel. Two structures are added to a standard frame-transfer CCD to form the electronic shutter: an n^+ dopant (shutter drain) is placed between the vertical transfer channels in the imaging array, and a p buried layer is located across the width of the pixel at a depth that alternates between 1.4 and 2.0 μm from the Si-SiO_2 interface. As will be described, the 1.4-μm-deep portion of the layer centered beneath the buried channel forms the collection area of the pixel during image capture while the 2.0-μm-deep portions create a storage region.

The numerical device simulators PISCES and CANDE were used to determine physical parameters associated with the electronic shutter, such as doping concentration and location of the p buried layer, and also to predict shutter performance. The process simulator SUPREM was used to generate doping profiles used in the device simulations. Figure 5-2 shows the depletion region in a back-illuminated pixel for the two electronic-shutter operating conditions, shutter open and shutter closed. When the shutter is open and an image is being captured, a voltage V_{IA} is applied to the imaging-array clock electrode such that the depletion region extends from the gate dielectric through the n buried channel and 1.4-μm p buried layer into the lightly doped p^- substrate. The high-resistivity substrate (~ 1000 Ω-cm) is easily depleted at moderate electrode voltages. The voltage V_{SD} that is applied to the n^+ shutter drains keeps the junctions reverse biased but is not sufficient to cause depletion through the p buried layer. Photoelectrons created by the optical signal entering the p^- substrate are attracted by the electric field to the n buried channel detection area where the charges are stored. Typical voltage levels for the shutter open are $0\ \text{V} \le V_{SD} \le 5\ \text{V}$ and $12\ \text{V} \le V_{IA} \le 20\ \text{V}$. The undepleted p buried layer creates an electric field that repels the photoelectrons away from the n^+ shutter drains. If a Maxwellian distribution for the holes is assumed, the shutter-drain barrier potential is

$$V = kT \ln\left(N_b / N_{\text{sub}}\right) , \tag{5.1}$$

where k is Boltzmann's constant, T is the temperature, N_b is the peak acceptor concentration of the p buried

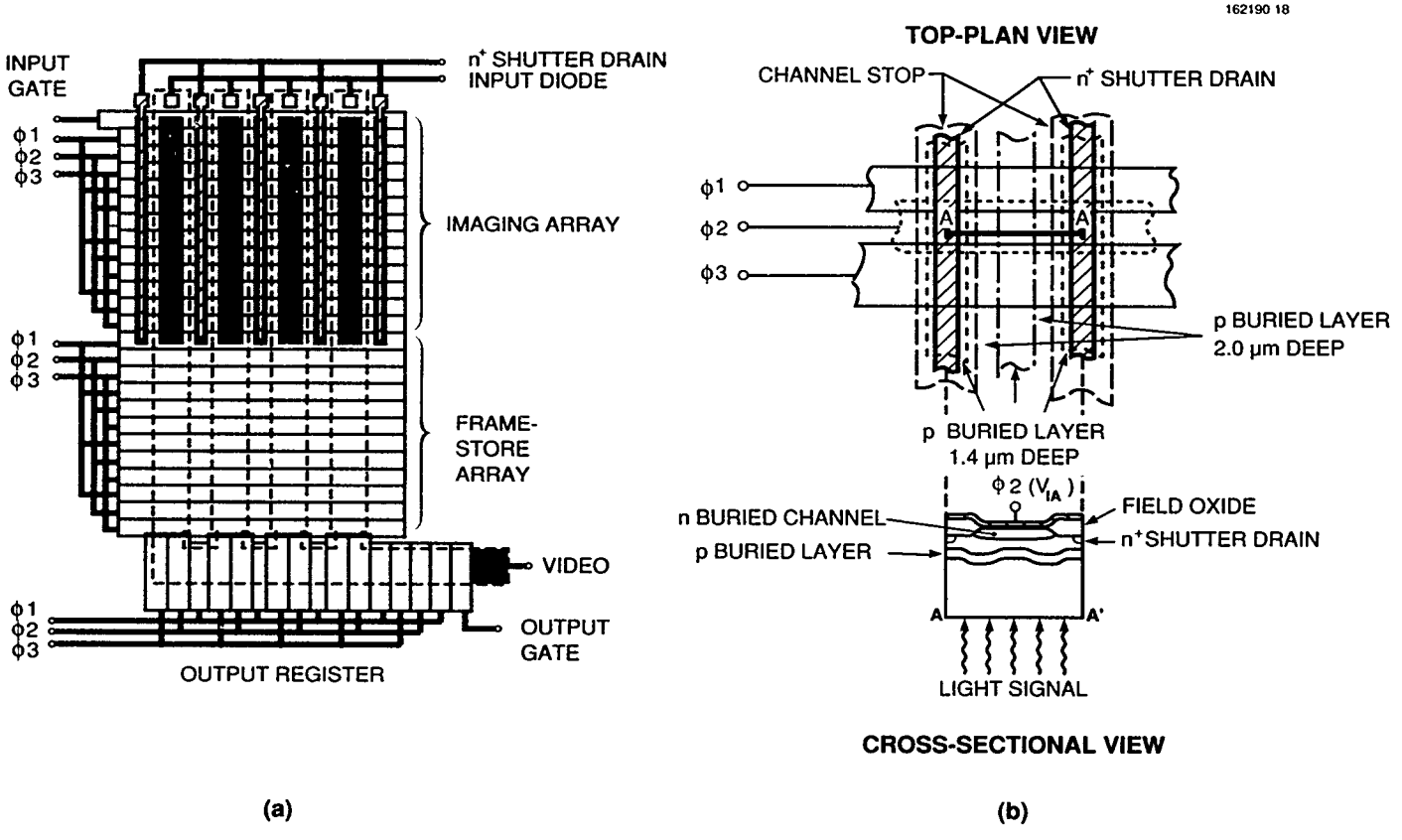

Figure 5-1. (a) Top-plan view of a frame-transfer CCD with electronic shutter, in which the imaging array is on top and the frame-store array is on the bottom. In each pixel the n^+ shutter drains are placed in the vertical imaging-array channel stop regions between the transfer channels. (b) Top-plan and cross-sectional views of a single back-illuminated pixel in the imaging array showing the location of n^+ shutter drains and 1.4- and 2.0-μm portions of the p buried layer. In the frame-store array the depth of the p buried layer is uniformly 2.0 μm.

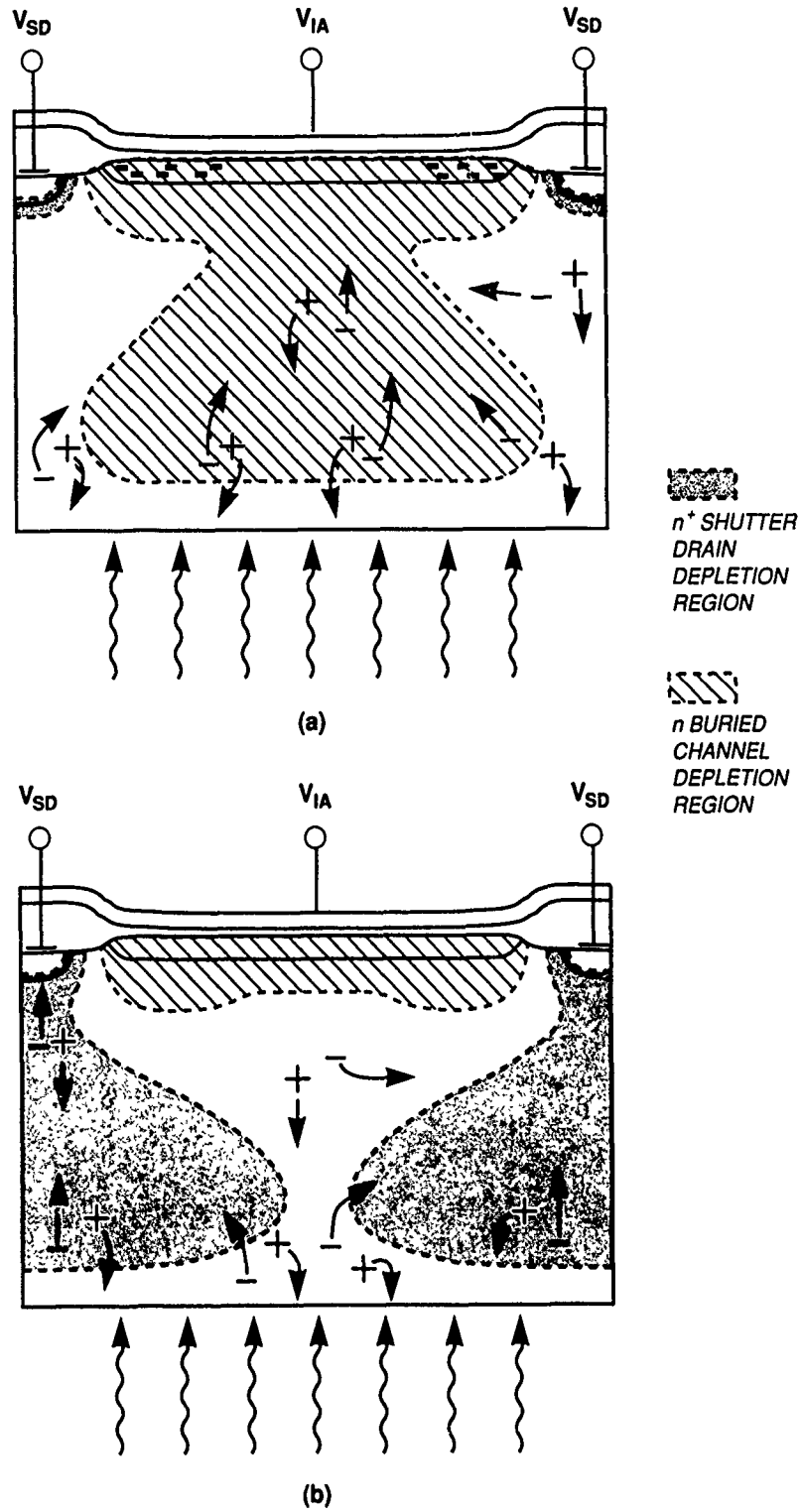

Figure 5-2. Single back-illuminated pixel in a CCD with electronic shutter showing the depletion regions associated with the n^+ shutter drains and n buried channel for (a) shutter-open and (b) shutter-closed operating conditions.

layer, and N_{sub} is the substrate acceptor concentration. Inserting the values used in the device simulator, CANDE, the barrier calculated from Equation (5.1) is ~ 0.2 eV, or about 7.5 times greater than the room-temperature thermal energy of an electron in the lattice.

Photoelectrons enter the *n* buried channel from the p^- substrate through the region of the 1.4-μm *p* buried layer near the center of the pixel [see Figure 5-2(a)]. A potential barrier, similar to that for the n^+ shutter drains, stops photoelectrons from directly entering the *n* buried channel region above the 2.0-μm *p* buried layer. The potential well in the buried channel adjacent to the 2.0-μm *p* buried layer is more positive than that adjacent to the 1.4-μm layer. As a result, the electrons that enter through the 1.4-μm *p* buried layer are transferred to the buried channel region above the 2.0-μm *p* buried layer, and therefore the depletion region under the central, collection part of the pixel is insensitive to the number of photo-electrons captured, up to some maximum amount. Additional photoelectrons beyond this maximum are shared between the collection and storage regions of the pixel, causing a gradual collapse of the depletion region.

To close the electronic shutter, a smaller voltage V_{IA} is appli d to the imaging-array clock electrode that is not sufficient to deplete through the *p* buried layer but is adequate for transfer of charge from pixel to pixel. A potential barrier between the *n* buried channel and the p^- substrate is created by the *p* buried layer. This barrier has an associated electric field that repels the photoelectrons away from the *n* buried channel. At the same time a larger voltage V_{SD} is applied to the n^+ shutter drains, causing the depletion region to spread beyond the *p* buried layer deep into the p^- substrate, as shown in Figure 5-2(b). Now, photoelectrons are attracted by the electric field to the shutter drains and as a result are not detected. Again, Equation (5.1) can be used to calculate the barrier potential between the *p* buried layer and the p^- substrate beneath the *n* buried channel. The potential resulting from this calculation is ~ 0.2 eV.

The process for fabrication of this device is varied to optimize the shutter for a particular operating spectrum. Operation of the shutter at longer wavelengths requires a thicker substrate layer with the thickness being approximately three absorption lengths for the longest wavelength to shutter. As the silicon thickness is increased, the substrate resistivity must be increased to ensure that the depletion regions extend to the back surface of the device.

Typical voltage levels and timing for the electronically shuttered CCD are shown in Figure 5-3. During image integration the electronic shutter is open. After the image has been captured, the shutter is closed. The image is then transferred to the frame-store array where it is protected by an aluminum light shield. Once the image is in the frame-store array, the shutter is opened and image integration can begin once again in the imaging array. Meanwhile, the stored image in the frame-store region is clocked out of the chip. A restriction on all applied voltages is that the magnitude be less than that necessary for avalanche breakdown. Trilevel clocking is required on the imaging-array electrode that is used for the collection of the photoelectrons during image capture.

Measurements demonstrating the capability of the integrated electronic shutter were done on front-illuminated CCDs. Although the shutter was designed for back-illuminated operation, it will function in a similar manner for front-illuminated devices if the absorption length of the light signal is much greater than the depth of the *p* buried layer. A high-pass filter was used in the experiments to stop light with

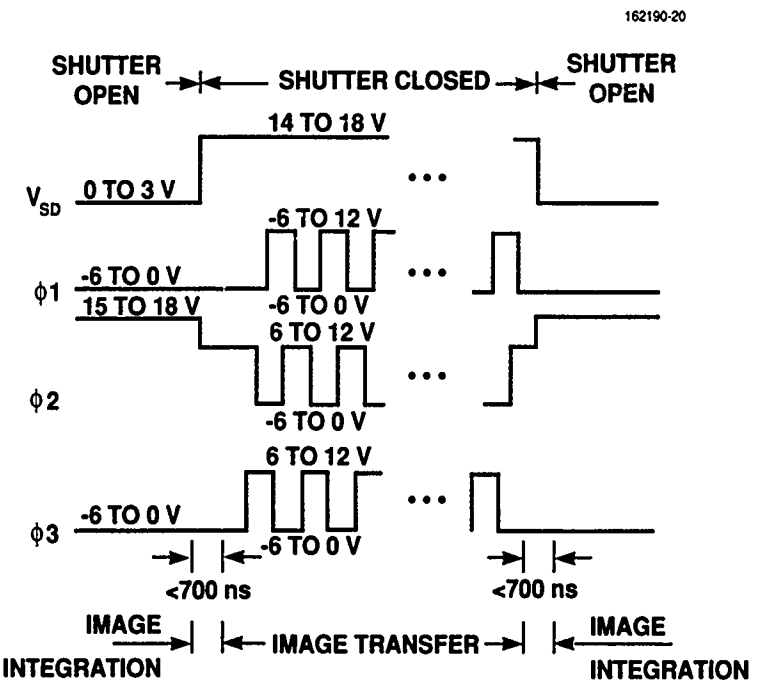

Figure 5-3. Timing diagram and typical voltage levels required for operation of the electronic shutter. The shutter is open during image integration and closed during transfer of the image from the imaging to frame-store array. Proper operation of the shutter requires about a 700-ns delay between switching applied voltages associated with the shutter and the beginning of an image integration or image transfer.

wavelengths less than 700 nm where the absorption length is ~ 4.5 μm. A bar pattern was projected onto the CCD imaging array that constantly illuminated the device under test. The intensity of the bars was enough to cause approximately full-well conditions in the CCD during the shutter-open time of 3.2 ms. Figure 5-4 shows a photograph of a shuttered and unshuttered image as well as the corresponding plots of signal voltage versus vertical position. For the dark pixels in between the bars, the signal voltage in the plots drops almost to zero in the shuttered device while the unshuttered device has significant "smear" signal. The extinction ratio calculated from the measurements is between 50 and 100. The shutter clock switching time in the tests was ~ 1 μs.

R.K. Reich
R.W. Mountain
W.H. McGonagle
B.B. Kosicki
E.D. Savoye

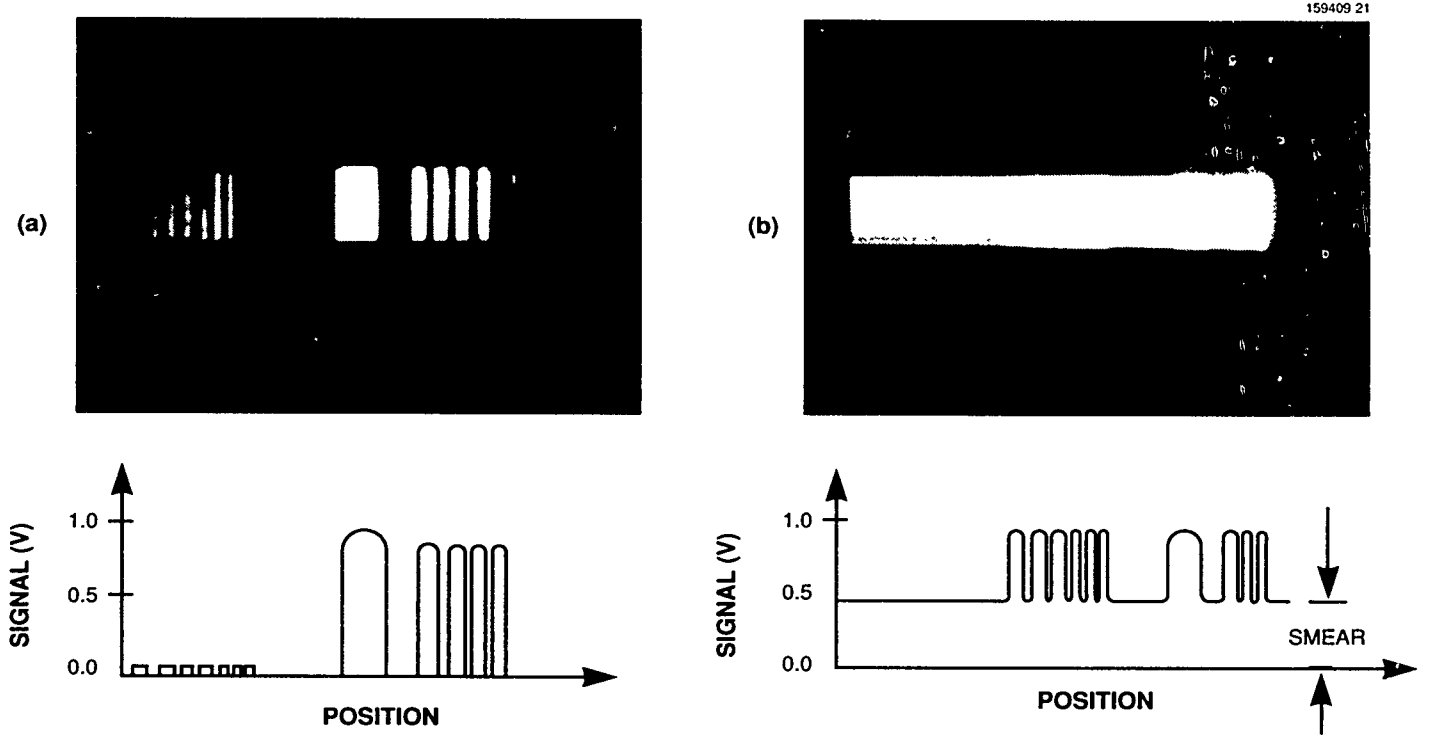

Figure 5-4. Photograph of bar pattern and corresponding signal voltage versus position for (a) shuttered and (b) unshuttered CCDs.

5.2 GaAs QUANTUM-WELL DYNAMIC RANDOM-ACCESS MEMORY CELL

A GaAs-based dynamic random-access memory (DRAM) cell using modulation-doped field-effect transistors (MODFETs) for accessing and sensing is expected to have a speed advantage relative to a Si DRAM. However, the lack of high-quality metal-oxide-semiconductor structures in GaAs has prevented the realization of a practical DRAM up to now. A new memory structure is described here that utilizes GaAs/AlGaAs quantum wells for charge storage sites. The material structure is compatible with that for MODFETs, which have demonstrated great promise for very high speed integrated circuits and which are used as access transistors in the cells.

The layers, grown by molecular beam epitaxy, are shown in Figure 5-5. This structure is similar to that of a MODFET with a superlattice buffer layer. Alloyed Ni/Ge/Au and Ti/Au metallizations are used for ohmic contacts and Schottky-barrier gates, respectively.

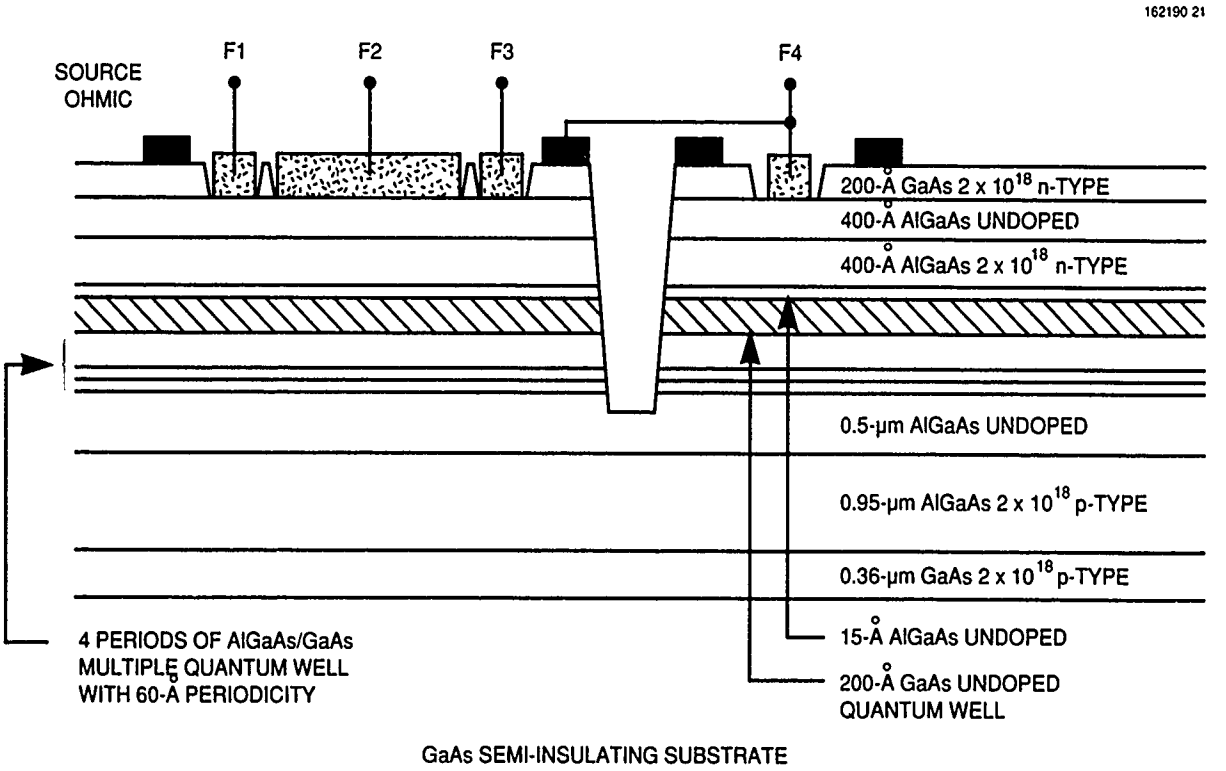

Figure 5-5. Structural diagram of the memory demonstration circuit. The quantum well under the gate F2 is the storage cell.

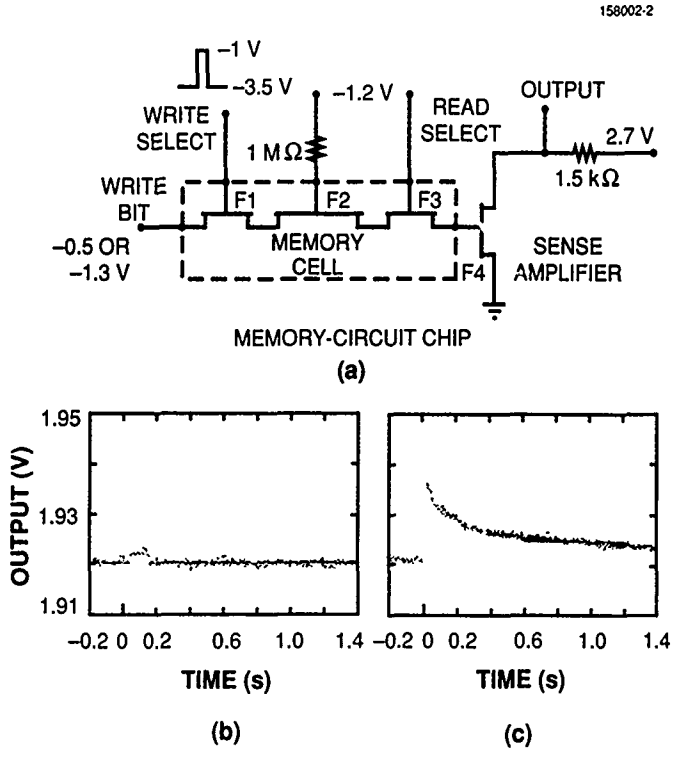

Figure 5-6. (a) Demonstration circuit diagram. (b) Waveform for –0.5-V source bias; the cell before t = 0 is in the 0 state. (c) Waveform for –1.3-V source bias.

A diagram of the memory cell demonstration cir uit is shown in Figure 5-6(a). The quantum well under the Schottky-barrier gate F2 is used as the storage cell. Access transistors F1 and F3 are used as control switches and F4 is the output buffer MODFET. This memory cell is designed for ease of testing purposes, and in an actual DRAM cell only one of the two transistors F1 and F3 would be required. Also, with proper MODFET and circuit designs, the 1-MΩ resistor through which a dc reference is provided to F2 can be eliminated. To write into the memory cell, F1 is turned on by applying a gate voltage above threshold. If the potential of the source ohmic contact is low, electrons will be transferred to the quantum well under the gate of F2 and the memory cell is considered in the 1 state; on the other hand, if the potential of the ohmic contact is high, no electrons will be transferred and a 0 state is written. The source contact corresponds to the data bit line and the gate of F1 to the word line in a DRAM circuit. Unselected bit lines would be allowed to float with no potential applied and therefore the state of unselected cells would not be altered during a write operation. To read the information, F3 is turned on, allowing charge stored under F2 to be transferred to the gate of the simple sense amplifier F4.

To simplify the circuit operation, F3 was kept on at all times in this experiment and a 50-μs pulse was applied to turn on F1. With a source voltage of –0.5 V, the nearly flat output response, shown in Figure 5-6(b), indicates that there is little charge being transferred when the pulse is applied; therefore, a 0

state is maintained in the memory cell. As shown in Figure 5-6(c), with a source bias of −1.3 V, the output voltage instantly rises at $t = 0$, representing a 1 state. The storage time, defined as the time required for the output voltage to fall below $1/e$ of the maximum transient value, is ~ 250 ms for this experiment. This storage time is a gross underestimate of the true capability of this cell because F3 is always on and provides no isolation for the storage cell. Nevertheless, this circuit has demonstrated the functionality and the MODFET compatibility of the memory cell. A 5.4-s storage time was measured in another test circuit with well-isolated storage cells. This charge retention time is sufficient for a DRAM cell. The DRAM circuit demonstrated is practical, easy to fabricate, and can be simplified to a conventional Si DRAM configuration for many potential applications.

C.L. Chen
W.D. Goodhue
L.J. Mahoney

REFERENCE

1. Solid State Research Report, Lincoln Laboratory, MIT, 1988:2, p. 51. DTIC AD-A204718.

6. ANALOG DEVICE TECHNOLOGY

6.1 ALL-REFRACTORY PROCESS FOR THE FABRICATION OF LOW-NOISE DC SQUIDS

An all-refractory process for the fabrication of superconductive circuits has now been established at Lincoln Laboratory. This process, based on $Nb/AlO_x/Nb$ trilayers [1] replaces the Nb/Pb technology used previously. The trilayers are deposited on oxidized Si substrates and the junction areas are defined by either a selective Nb anodization process (SNAP) or a selective Nb etching process (SNEP) [1],[2]. Both processes have yielded high-quality Josephson junctions for junction areas > 25 μm^2 and critical current densities up to 1000 A/cm^2. A measure of the junction quality is V_m, which is the product of the critical current and the subgap resistance measured at 2 mV. For refractory junctions, V_m exceeds 50 mV, an improvement over the $Nb/NbO_x/Pb$ planar junctions with V_m of 35 mV and the $Nb/NbO_x/Pb$-In-Au edge junctions developed at IBM with V_m of 20 to 30 mV.

Josephson junctions defined by SNEP with areas less than about 25 μm^2 have lower V_m because shunting paths at the edges reduce the subgap resistance. In the case of junctions defined by SNAP, the subgap resistance of small-area junctions is greatly improved by increasing the rate of formation of the anodic oxide. At an oxidation rate greater than 15 nm/s, V_m is independent of junction area for areas as small as 0.3 μm^2. Figure 6-1 shows the current-voltage plot of a Josephson junction defined by SNAP at 4.2 K. The junction area is 0.5 μm^2, and the calculated value of V_m and the critical current density J_c (for a critical current × normal-state resistance = 2.28 mV) are 60 mV and 1140 A/cm^2, respectively.

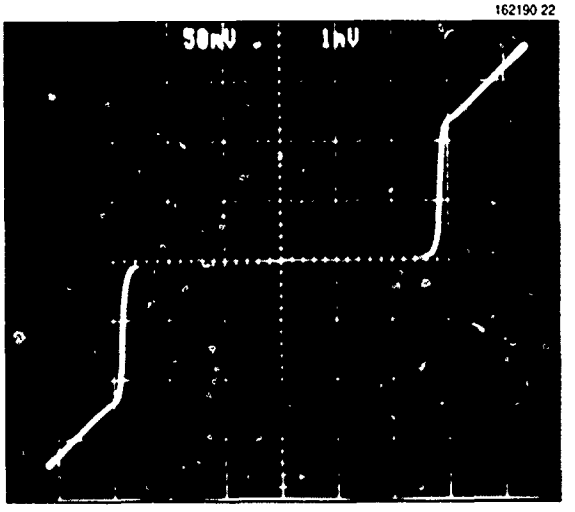

Figure 6-1. I-V characteristics of a Josephson junction fabricated using the all-refractory SNAP trilayer process.

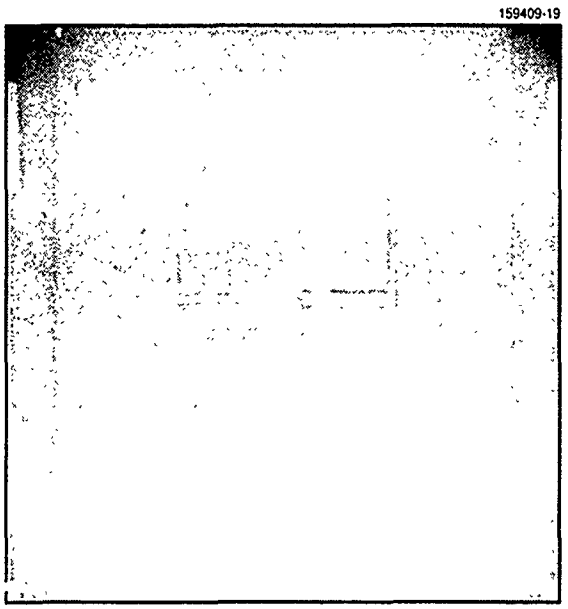

Figure 6-2. Photograph of a dc SQUID.

Previous measurements of dc superconducting quantum interference devices (SQUIDs) fabricated using an all-refractory trilayer process show a higher white-noise level than those fabricated with Nb/Pb technology [3]. As this is a matter of concern for SQUID-based instrumentation, experiments were conducted to study the noise properties of SQUIDs made using this new process. A photograph of the basic SQUID design, which did not include an input coil, is shown in Figure 6-2. The SQUID inductance, junction areas, and the resistive-shunt geometry were varied in a matrix fashion to give SQUIDs with near-optimum parameter values for a factor-of-5 range in J_c and with the sheet resistance of the shunt resistor. The devices were fabricated using both SNAP and SNEP processes with a minimum feature size of 2 μm and J_c ranging from 400 to 1000 A/cm^2. The noise was measured with an RF SQUID using a direct small-signal readout scheme.

Our best results were obtained from SQUIDs fabricated using the SNAP process. Figure 6-3 shows a noise-power spectrum of a representative 50-pH SQUID with square junctions 2×2 μm that had critical currents of 20 μA and shunt resistors of 6 Ω. The white noise is below 3×10^{-13} Φ_0^2/Hz and the white-to-1/f crossover frequency is below 20 Hz. This noise performance matches or exceeds that of the best dc SQUIDs fabricated with Nb/NbO_x/Pb-In-Au edge junction technology at IBM [4] and verifies the suitability of the all-refractory Nb/AlO_x/Nb trilayer process for high-performance SQUID applications.

M. Bhushan
*M.B. Ketchen
*S.B. Kaplan
*W.J. Gallagher

*Author not at Lincoln Laboratory.

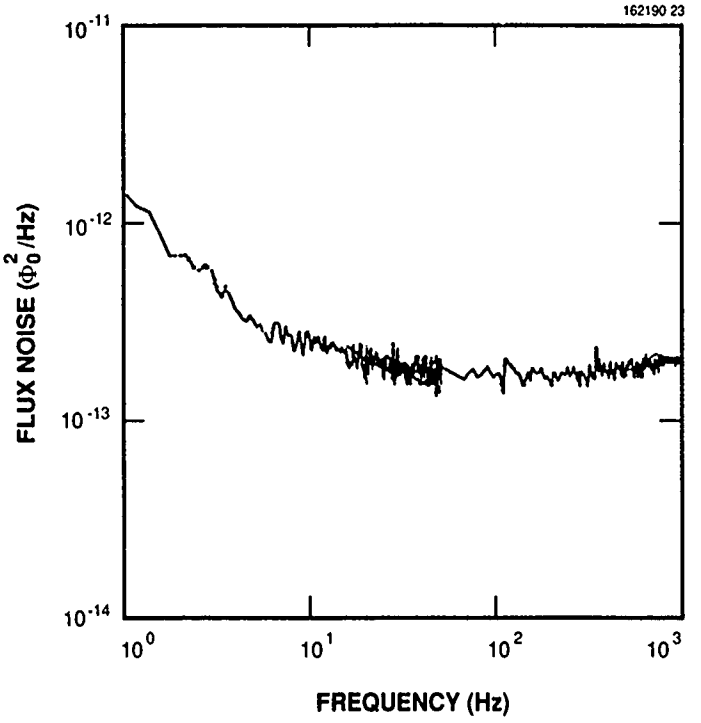

Figure 6-3. Noise-power spectrum of a dc SQUID fabricated using the all-refractory SNAP process.

6.2 5-V UNIPHASE CMOS/CCD PROCESS FOR MIXED-SIGNAL CIRCUITS

We have developed a 2-μm CMOS process to allow integration of high-performance analog, digital, and discrete-time analog (charge-coupled device and switched-capacitor filter) circuitry. Such capability will allow us to design very sophisticated mixed-signal chips in which every function is optimally implemented. The basic process is a double-polysilicon (both levels active), double-metal, *n*-well CMOS process that allows high density and a high level of integration. The MOSFET gate oxide is sufficiently thick (50 nm) to guarantee reliable operation with ± 5-V power supplies, which are the new standard for analog signal processing. The process also supports high-performance, dual-dielectric, buried-channel charge-coupled devices (CCDs) operating between the ground and +5-V rail with uniphase clocks. With this arrangement the charge packets under the unclocked "dc" phase can be sensed nondestructively with floating-gate taps.

Because of several competing requirements, the design of the CCDs presented the greatest challenge in this process development. The channel doping of the single-phase CCDs is all phosphorus. After an initial uniform phosphorus implant to define the buried channel, a second phosphorus implant is added after the first polysilicon is defined to create the storage wells [5]. The storage and barrier implants had to be engineered with a low dose (thresholds less negative than –3 V) to enable 5-V levels for the clocks, drain, and source while maintaining large charge capacity. The gate dual-dielectric had to be thick

enough for reliable operation but thin enough for the buried-channel implant to be narrowly confined slightly below the interface. To obtain high speed and low noise in the buried-channel CCDs, it is important that the charge packet be always confined in the channel, away from the interface.

Our previous two-phase buried-channel CCDs [5] were analyzed using the process and device simulation programs SUPREM and CANDE. The analysis indicated that much of the buried-channel implant, which peaked at the interface, was used inefficiently since it did not contribute to making the charge packet larger but made the channel potential too positive for 5-V uniphase operation. Using SUPREM and CANDE we were able to determine the parameters of the shallow buried channel profile that retained the high charge density required for good dynamic range (2000 electrons/μm^2) while simultaneously achieving channel potentials and well depths compatible with 5-V operation.

The CCD substrate chosen was p-Si, with $N_A = 5 \times 10^{14}$ cm^{-3}, and the nitride and oxide thicknesses in the gate dual-dielectric were 30 and 40 nm, respectively. After an initial uniform phosphorus implant to define the buried channel (4×10^{11}-cm^{-2} dose at 270 keV), a second self-aligned phosphorus implant was added to create the storage wells (2.3×10^{11}-cm^{-2} dose at 270 keV). The phosphorus concentration profiles in the barrier and storage regions calculated with SUPREM are shown in Figure 6-4. The barrier

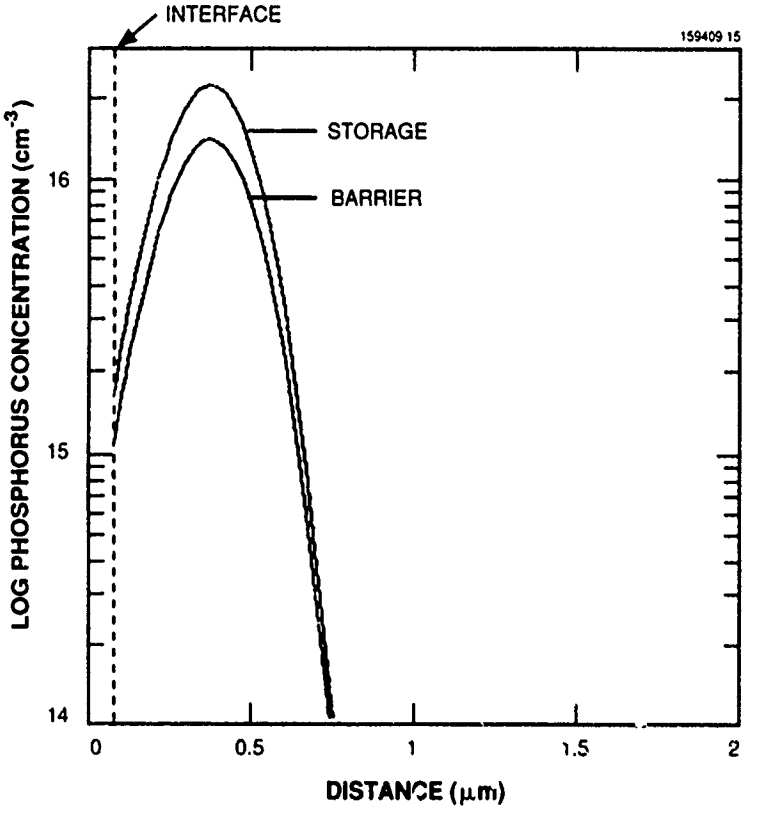

Figure 6-4. Phosphorus concentration profiles in the barrier and storage regions calculated with SUPREM.

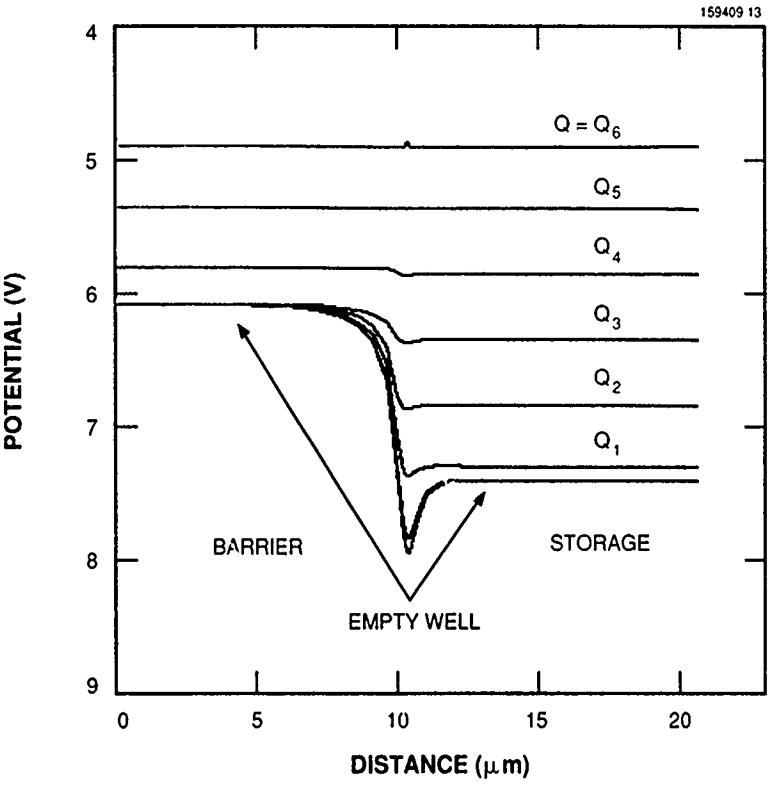

Figure 6-5. Channel potential in the barrier and storage wells for different charge packets when 5 V is applied to the gates.

and storage potentials were calculated with CANDE. The simulations assumed infinitely long electrodes separated by an interelectrode gap much larger than used in practice. The potential trough in the transition region between the two electrodes is an artifact of this gap. Figure 6-5 shows the channel potential for different charge packets when 5 V is applied to the gates. From the figure we see that the charge corresponding to a full well, i.e., before electrons spill over the barrier, is $Q_3 < Q_{max} < Q_4$. For this design, $Q_3 = 1700$ electrons/μm^2 and $Q_4 = 2700$ electrons/μm^2, corresponding to $Q_3 = 4.1 \times 10^5$ electrons and $Q_4 = 6.5 \times 10^5$ electrons for our CCDs, which have a well area $A = 240\ \mu m^2$. Figure 6-6 shows the calculated distribution of the charge packets in Figure 6-5, in a cross section of the storage wells, for $V_g = 5$ V. From Figure 6-6 we see that all allowable charge packets of this design ($Q < Q_{max}$) are safely away from the interface. The CCD structure with barrier and storage gates 4 and 6.5 μm long, respectively, and a 0.3-μm interelectrode gap was modeled with CANDE. The calculated channel potential and electric field in the channel are shown in Figure 6-7. By integrating the electric field in the channel, we calculated the single electron transit time [5] $T_t = 1.4$ ns.

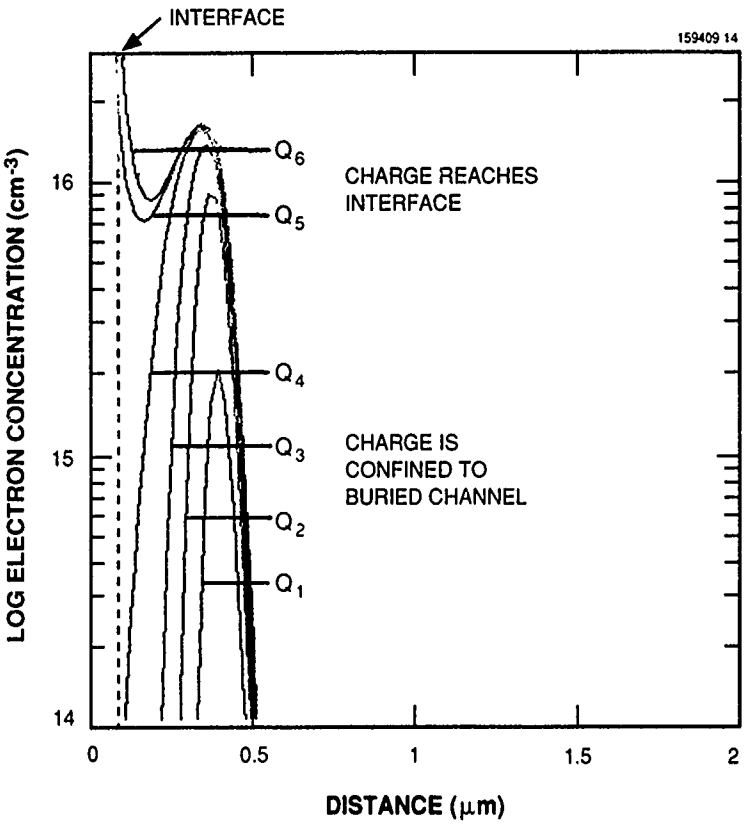

Figure 6-6. Calculated distribution of the charge packets for the conditions shown in Figure 6-5 in a cross section of the storage wells.

We have fabricated a CCD test structure with this process and verified experimentally that it could operate with 5 V and that the maximum charge capacity is $Q_{max} = 4.8 \times 10^5$ electrons. This value is consistent with our calculations and confirms that the charge capacity of the new buried channel is not compromised by the low implant doses of this new process. We expect the fringing fields to be strong enough to allow clock rates greater than 100 MHz. Furthermore, the process was designed to be compatible with our step-doping technology [5], which allows us to build in the drift fields necessary for even higher speed charge transfer.

Characterization of this CMOS/CCD process is nearly complete, and we are well into the design of a CCD-based correlator (a chip with 58×10^3 transistors) that will use our new process to achieve 5×10^{10} operations per second with 100-MHz clocks. The 5-V compatibility of the CCD opens up many possibilities that were previously impractical. For example, many short CCDs could be operated in parallel under control of a master 5-V clock to perform multivalued logic functions or to act as neurons in a neural net.

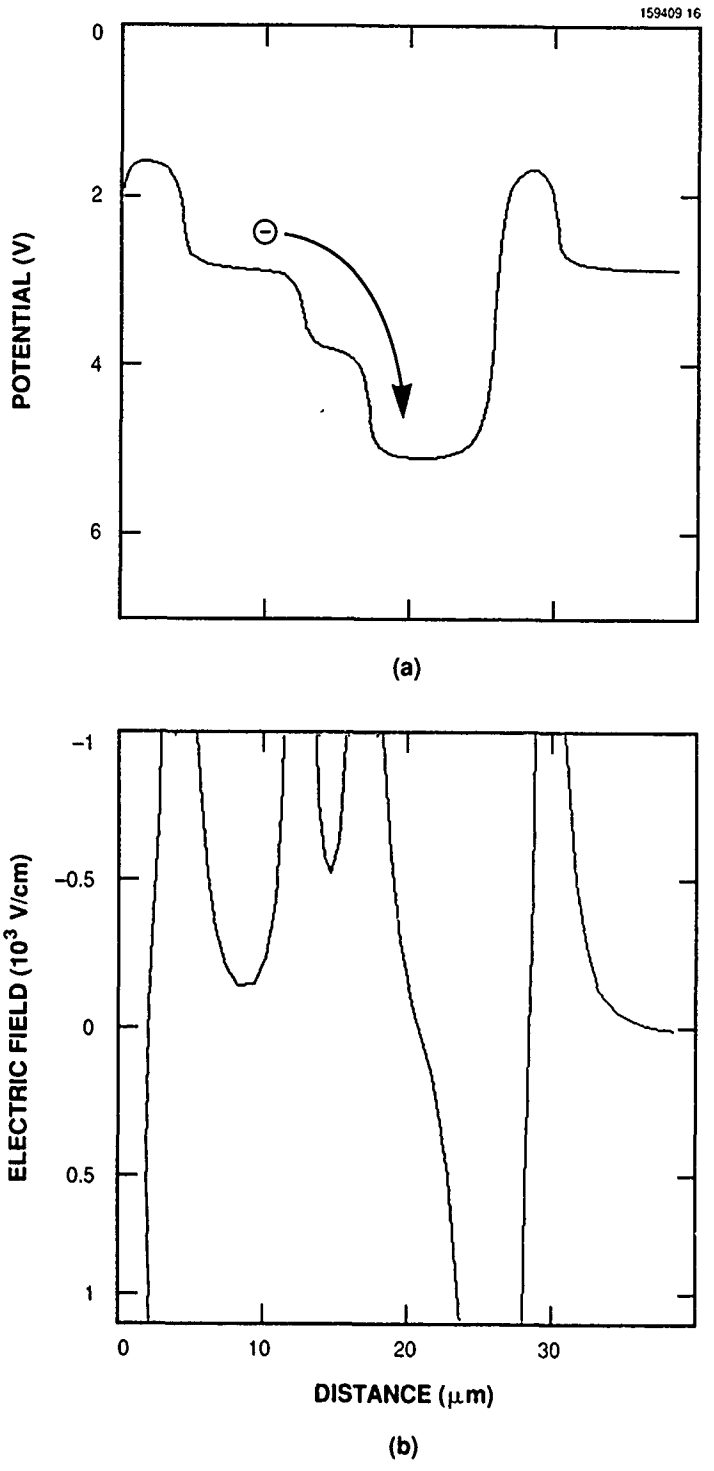

Figure 6-7. (a) Calculated channel potential in the CCD when no charge is present. (b) Calculated electric field corresponding to (a).

The ability to integrate all three signal-processing domains in an optimal fashion will also enable us to integrate on a single chip a large fraction of complex systems, such as spread-spectrum receivers.

S.C. Munroe
A.L. Lattes
D.B. Whitley
D.R. Arsenault

REFERENCES

1. M. Gurvitch, M.A. Washington, and H.A. Huggins, *Appl. Phys. Lett.* **42**, 472 (1983).
2. H. Kroger, L.N. Smith, and D.W. Jillie, *Appl. Phys. Lett.* **39**, 280 (1981).
3. M.W. Cromar, J.A. Beall, D. Go, K.M. Masarie, and R.H. Ono, *IEEE Trans. Magn.* **25**, 1005 (1989).
4. V. Foglietti, W.J. Gallagher, M.B. Ketchen, A.W. Kleinsasser, R.H. Koch, S.I. Raider, and R.L. Sandstrom, *Appl. Phys. Lett.* **49**, 1393 (1986).
5. Solid State Research Report, Lincoln Laboratory, MIT, 1990:2, p. 55.

REPORT DOCUMENTATION PAGE

Form Approved
OMB No. 0704-0188

1. AGENCY USE ONLY *(Leave blank)*	2. REPORT DATE	3. REPORT TYPE AND DATES COVERED
	15 August 1990	Quarterly Technical Report, 1 May — 31 July 1990

4. TITLE AND SUBTITLE

Solid State Research

5. FUNDING NUMBERS

C — F19628-90-C-0002
PE — 63250F
PR — 221

6. AUTHOR(S)

Alan L. McWhorter

7. PERFORMING ORGANIZATION NAME(S) AND ADDRESS(ES)

Lincoln Laboratory, MIT
P.O. Box 73
Lexington, MA 02173-9108

8. PERFORMING ORGANIZATION REPORT NUMBER

1990:3

9. SPONSORING/MONITORING AGENCY NAME(S) AND ADDRESS(ES)

Air Force Systems Command, USAF
Andrews AFB
Washington, DC 20334-5000

10. SPONSORING/MONITORING AGENCY REPORT NUMBER

ESD-TR-90-119

11. SUPPLEMENTARY NOTES

None

12a. DISTRIBUTION/AVAILABILITY STATEMENT

Approved for public release; distribution is unlimited.

12b. DISTRIBUTION CODE

13. ABSTRACT *(Maximum 200 words)*

This report covers in detail the research work of the Solid State Division at Lincoln Laboratory for the period 1 May through 31 July 1990. The topics covered are Electrooptical Devices, Quantum Electronics, Materials Research, Submicrometer Technology, Microelectronics, and Analog Device Technology. Funding is provided primarily by the Air Force, with additional support provided by the Army, DARPA, Navy, SDIO, NASA, and DOE.

14. SUBJECT TERMS

electrooptical devices	microelectronics	optical modulation	ultraviolet lithography
quantum electronics	analog device technology	epitaxial growth	charge-coupled devices
materials research	lasers	quantum wells	random-access memories
submicrometer technology	nonlinear optics	infrared detectors	superconductive devices

15. NUMBER OF PAGES
98

16. PRICE CODE

17. SECURITY CLASSIFICATION OF REPORT	18. SECURITY CLASSIFICATION OF THIS PAGE	19. SECURITY CLASSIFICATION OF ABSTRACT	20. LIMITATION OF ABSTRACT
Unclassified	Unclassified	SAR	